

Detecting the Invisible Universe with Neutrinos and Dark Matter

by

Asher C. Kaboth

A.B., University of Chicago (2006)

Submitted to the Department of Physics
in partial fulfillment of the requirements for the degree of

Doctor of Philosophy in Physics

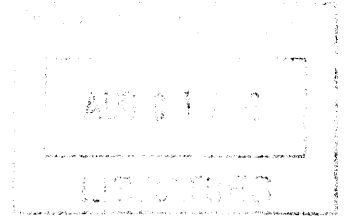
at the


MASSACHUSETTS INSTITUTE OF TECHNOLOGY

June 2012

© Massachusetts Institute of Technology 2012. All rights reserved.


ARCHIVES



Author 

Department of Physics

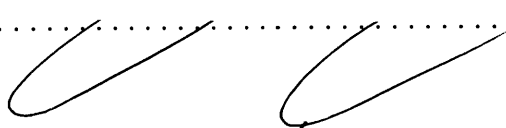
Feb 29, 2012

Certified by 

Peter Fisher

Professor

Thesis Supervisor

Certified by 

Joseph Formaggio

Associate Professor

Thesis Supervisor

Accepted by 

Krishna Rajagopal

Associate Department Head for Education

Detecting the Invisible Universe with Neutrinos and Dark Matter

by

Asher C. Kaboth

Submitted to the Department of Physics
on Feb 29, 2012, in partial fulfillment of the
requirements for the degree of
Doctor of Philosophy in Physics

Abstract

Recent work in astrophysics has show that most of the matter in the universe is non-luminous. This work investigates two searches for non-luminous matter: hot dark matter formed from cosmic relic neutrinos from the Big Bang, and directional detection of cold dark matter. The cosmic neutrino background is investigated through the KATRIN experiment, using neutrino capture on tritium to search for a signal. A sensitivity at KATRIN of about 10^4 events per year, or a local overdensity of relic neutrinos of about 3×10^9 is found.

Directional detection of cold dark matter provides a unique way to distinguish a dark matter signal from terrestrial backgrounds, using the expected direction of a dark matter wind based on astrophysical parameters. This work presents a new technique for directional dark matter detection—a drift chamber readout using a CCD camera. The backgrounds of this detector are investigated and enumerated, and a dark matter search sets a limit at $m_\chi = 100$ GeV of $3.7 \times 10^{23} \text{ cm}^2$.

Thesis Supervisor: Peter Fisher
Title: Professor

Thesis Supervisor: Joseph Formaggio
Title: Associate Professor

Acknowledgments

This work would not have been possible without the support and help of many people. First, I want to thank Peter and Joe, who have been excellent advisors and mentors. Your insights and advice have made me grow as a scientist and a person. I also want to thank the collaborators on KATRIN and DMPTC with whom I have worked closely: Shawn, Cosmin, Jeremy, Dan, Ben, Denis, James, Jocelyn, and Gabriella. None of this would have been possible without your labors.

I also want to thank the employees of WIPP who ensured that our work underground could happen, especially Norbert Rempe, Kevin McIllwee, Delores Hutchinson, and Rob Hayes. The people of EXO also provided invaluable advice, assistance, and the loan of tools and time as we learned to do science in a salt mine, especially Jon, Adam, Jesse, and Michelle.

The roots of this work stretch further back than my time in graduate school, and I must thank Ed Blucher, who set me on the path to neutrinos and research, and all the teachers who have made an impact on the way I think, especially Mr. Wallace and Dr. Léger.

I have been lucky to have many wonderful groups of friends while in graduate school: my fellow graduate students (especially the Penthouse residents), who were always willing to help with the myriad small daily problems of research; the bell ringers and knitters, who have been a source of much laughter and stress relief; the people of First Church (especially the Havrutites), who have nourished my heart and soul; and all the others who are part of my chosen family, who have kept me happy and fed.

Finally, I want to thank my parents. I couldn't have done it without your love and encouragement.

Contents

1	Introduction	21
1.1	Composition of the Universe	21
1.2	Hot Dark Matter and the Cosmic Neutrino Background	22
1.3	Cold Dark Matter	25
1.3.1	Historical Context	26
1.3.2	Dark Matter in the Milky Way	27
1.3.3	Dark Matter Candidates	29
1.3.4	Interaction Rates and Models	32
1.3.5	Current Results from Dark Matter Experiments	39
2	The KATRIN Experiment	47
2.1	Tritium Source	47
2.2	Transport Section	49
2.3	Rear Section	49
2.4	Spectrometers	49
2.5	Detector	51
2.6	Uncertainties and Reach	52
3	The Cosmic Neutrino Background at KATRIN	55
3.1	Expected Event Rates and Spectra	55
3.2	Expected Sensitivity	56
3.3	Implications	59

4	The DMTPC Experiment	63
4.1	Detector Configuration	63
4.1.1	Outer Vessel and Gas System	63
4.1.2	Field Cage	65
4.1.3	Amplification Region	65
4.1.4	CCD Readout	68
4.1.5	Charge Readout	68
4.2	Gas Properties of CF_4	69
4.2.1	Drift Electron Diffusion and Attachment	69
4.2.2	Scintillation Spectrum	70
4.3	Calibration	70
4.3.1	Energy Calibration	72
4.3.2	Energy Stability	72
4.3.3	Relative Gain Calibration	74
5	Underground Operation of DMTPC	79
5.1	The WIPP Facility	79
5.2	Data Taking	81
5.3	Data Processing	81
5.3.1	Image Cleaning	81
5.3.2	Track Finding	82
5.3.3	Parameter Calculation	83
5.3.4	Monte Carlo Simulation and Parameter Reconstruction Quality	85
5.4	Backgrounds	89
5.4.1	Sparks	93
5.4.2	Residual Bulk Images	94
5.4.3	Worms	95
5.4.4	Edge Crossing Tracks	97
5.4.5	Cutoff Tracks	97
5.4.6	Misjoined Tracks	100

5.4.7	Extreme Partial Sparks	100
5.4.8	Spacers	100
5.4.9	Cut Efficiencies	100
5.4.10	Final Data Sample	101
5.5	Dark Matter Limits	103
5.6	Discussion	106
6	Conclusions	111

List of Figures

1-1	A sample rotation curve from the galaxy NGC 9138. [1] The square points show the experimental data. The dashed line shows the velocity component coming from the galactic disc. The dotted line shows the velocity component from the interstellar gas. The dot-dashed line shows the velocity component from dark matter. The solid line shows the sum of the three components.	27
1-2	The Milky Way rotation curve as calculated in Reference [2]. The two plots show the rotation curve fit for two different measured parameters of R_0 , the distance to the galactic center and Θ_0 , the rotational velocity of the sun around the galactic center. Dashed line shows dark matter contribution, dotted line shows stellar bulge contribution, filled circles show stellar disc contribution, and crosses and open circles show the gas components of HI and H_2 respectively.	28
1-3	The difference in recoil energy spectra for the maximum (red dotted line) and minimum (blue dashed line) earth velocity through the year. The example target is a ^{19}F nucleus and the WIMP is 100 GeV. Note that recoils get pushed to lower energies when the relative earth velocity is at a minimum.	35
1-4	The WIMP interaction rate as a function of recoil energy and angle between recoil and the direction of the motion of the Earth. The example target is a ^{19}F nucleus and the WIMP is 100 GeV.	36

1-5	Current WIMP spin independent cross section limits. Dotted black line shows the XENON100 results [3]. Solid black line shows the CDMSII results [4]; solid grey line shows the CDMSII low threshold analysis results. [5]. Dark red and light red regions show the allowed regions for DAMA/LIBRA under the assumptions of ion channeling and no ion channeling, respectively. [6]. Solid light blue area shows the allowed region for the CoGeNT experiment. [7]. Plot made using DMTools. [8]	41
1-6	Current WIMP spin dependent cross section limits, normalized to the proton. Dotted black line shows the COUPP limit. [9]. Solid black line shows the KIMS limit. [10] Dark red and light red regions show the allowed regions for DAMA/LIBRA under the assumptions of ion channeling and no ion channeling, respectively. [6]. Plot made using DMTools. [8]	42
1-7	Residual rates from the yearly average for the DAMA/LIBRA experiment in different energy bins. [6] The x-axis is time in days since the beginning of the experiment. The solid line shows the predicted oscillation, with the amplitude fit in each energy bin. Dashed and dotted lines show maxima and minima, respectively.	44
1-8	Recent results from the CoGeNT experiment.	45
2-1	The KATRIN detector, showing the major components of the system: rear system (yellow), source (blue), transport section (red), spectrometers (green) and detector (grey).	48
2-2	Schematic of a MAC-E-Filter, showing the longitudinal locations of important fields. The arrows along the bottom show the change in transverse energy to longitudinal energy in the filter.	50

2-3	The sensitivity and discovery potential of the KATRIN experiment as a function of neutrino mass, described in number of sigma away from zero. Horizontal red line shows the 90% confidence limit bound. KATRIN thus has 5- σ discovery potential at 0.35 eV and a 90% bound setting sensitivity at 0.2 eV.	54
3-1	The anticipated beta decay spectrum as a function of retarding voltage with (black) and without (red) neutrino capture events. Neutrino mass is assumed to be 1 eV.	58
3-2	Confidence regions for cosmic neutrino captures in events per year versus neutrino mass in eV for four example neutrino masses. Statistical errors only are shown. Red ellipse shows 90% C.L in the $C\nu B$ events per year and neutrino mass parameter space.	60
3-3	The 90% confidence level sensitivity limit for relic neutrino over-density as a function of neutrino mass as expected from the 3 year data run at the KATRIN neutrino mass experiment. Solid curves show expectation from cosmological prediction assuming Fermi-Dirac (light blue), Navarro-Frenk-White (violet), and Milky Way (yellow) mass distribution. Arrow shows neutrino mass limits already obtained from cosmological observations($\sum m_\nu \leq 1.2$ eV) [11].	61
4-1	A schematic and a photograph of the DMTPC 10L detector	64
4-2	A finite element method analysis of the electric potential contours of the 10L drift cage for 1000 V applied. Numbers are in units of volts. The horizontality and uniform spacing of the contours indicates that the electric field points vertically downwards and is uniform along the drift cage.	66
4-3	A finite element method analysis of the transverse field in the 10L drift cage. The colors indicate the value of E_T/E . The active area has no more than 1% transverse field.	67
4-4	The transverse diffusion of CF_4 as a function of reduced field.	70

4-5	The measured scintillation spectrum of CF_4 as a function of wavelength. The integral of the spectrum is set to unity. Error bars are not shown for clarity. $58\pm 6\%$ of the spectrum lies between 450 and 800 nm.	71
4-6	The wavelength-dependent quantum efficiency for the Kodak1001E chip of the Apogee Alta U6 cameras. The peak of this spectrum is well-matched to the 630 nm peak in the scintillation spectrum of CF_4 .	71
4-7	The energy calibration for (a) the top chamber and (b) the bottom chamber. Black points show data from alpha tracks in the chamber and red shows Monte Carlo generated tracks using the calibration constants 18.6 keV/adu (top) and 17.5 keV/adu (bottom) which provide the best match to the data.	73
4-8	The variation of the energy calibration within a gas fill for three different fills. The gain rises about 3% over the course of a fill, and the interfill variation is 7%.	74
4-9	The variation of the energy calibration across many gas fills (one point per fill) for 850 hours. There is a downward trend with a variation of about 7%.	75
4-10	Relative gain maps for the DMTPC 10L detector, produced using a Cs-137 and a Co-57 source. Spacers are marked with dotted lines. The maps are normalized such that the average value of a pixel in the image is 1.	77
5-1	A photograph of the lab where the DMTPC 10L is located in the WIPP facility. The detector is in the far right corner of the lab as shown in this picture.	80
5-2	A photograph of the 10L detector installed in DMTPC lab at the WIPP facility.	80

5-3	Energy and range reconstruction for top detector. Shown in (a) is the energy resolution as a function of recoil energy, which is 14.6% at 100 keV. Shown in (b) is the range reconstruction as a function of recoil energy. The colored histogram shows the distribution of Monte Carlo events, and black points are a profile histogram of the points, with the error bars representing the RMS of each energy bin.	86
5-4	Energy and range reconstruction for bottom detector. Shown in (a) is the energy resolution as a function of recoil energy, which is 17.0% at 100 keV. Shown in (b) is the range reconstruction as a function of recoil energy. The colored histogram shows the distribution of Monte Carlo events, and black points are a profile histogram of the points, with the error bars representing the RMS of each energy bin.	87
5-5	Projected range (2D) as a function of recoil energy for a ²⁵² Cf run, top camera. Black points show nuclear recoil candidates; grey shading shows Monte Carlo generated nuclear recoil candidates; blue line shows predicted (3D) range-energy function for the running conditions. . . .	88
5-6	Projected range (2D) as a function of recoil energy for a ²⁵² Cf run, bottom camera. Black points show nuclear recoil candidates; grey shading shows Monte Carlo generated nuclear recoil candidates; blue line shows predicted (3D) range-energy function for the running conditions. . . .	89
5-7	Angular reconstruction (ϕ) for (a) top camera and (b) bottom camera.	90
5-8	Axial angular reconstruction (ϕ) for (a) top camera and (b) bottom camera. The colored histogram shows the distribution of Monte Carlo events, and black points are a profile histogram of the points, with the error bars representing the RMS of each energy bin.	91
5-9	Correct percentage of vector direction determination for (a) top camera and (b) bottom camera	92
5-10	A sample partial spark. Note the hard edge of the excess light near the middle of the image. This is the defining quality of a partial spark.	94

5-11 Worm subtypes in the DMTPC detector. Type (a) shows a high deposition worm—note the difference in vertical scales between (a) and (b)/(c). Type (b) shows a medium deposition worm. Type (c) shows a ‘blank’ worm. All images have been zoomed in to show the structure of the worm. The pixels found to be in the track are shown outlined with a thin white line. 96

5-12 Fisher discriminant cuts for (a) top camera and (b) bottom camera. The black line shows Monte Carlo simulated recoils and the red line shows tracks from detector off datasets. The small bleed of worms above the cut shown comes from the third type of worm (blank worms) and is addressed by the lower bound cut on cluster RMS. 98

5-13 A sample cutoff track. Note the hard edge on the left side of the track; this is the hallmark of a cutoff track. 99

5-14 The distributions for the two x-derivatives of clusters. Red points show Monte Carlo generated cutoff alpha tracks which pass all other reconstruction cuts. Color-scaled boxes show Monte Carlo nuclear recoil tracks which pass all other reconstruction tracks. The black line shows the cut described in the text. 99

5-15 A sample extreme partial spark. The image has been zoomed to show both the small amount of light near the left-hand edge and the nuclear recoil candidate resulting from RBI next to it. 101

5-16 Cut efficiencies as a function of energy for (a) top camera and (b) bottom camera. Not shown are the RBI, track rejoining, or edge cut sparks, as they do not contribute in simulation. 102

5-17 Range vs. energy for tracks that pass all cuts. Data points are shown with black circles; the predicted range vs. energy curve for fluorine recoils is shown with the blue line. 104

5-18 The energy spectrum for tracks that pass all cuts. 104

5-19 The reduced phi distribution for tracks that pass all cuts. Evidence for dark matter would appear as a peak around zero. 105

5-20	The reduced phi distribution as a function of energy for tracks that pass all cuts.	105
5-21	WIMP cross section normalized to single proton limits as a function of mass for this work using an assumption of 1 s exposures (solid black line), an assumption of 1.3 s exposures (small dotted blue line), and a brief run with 5 s exposures (long dashed magenta line). Also shown are limits from the 10L above ground (dotted grey line) [12], NEWAGE (dot-dash red line) [13], KIMS (dotted green line) [14], PICASSO (dotted cyan line) [15], and projected for the next generation DMTPC detector (small dotted blue line).	107

List of Tables

1.1	Lifetimes and cross sections for neutrino capture on nuclei of interest in beta decay experiments	24
1.2	Cosmic neutrino background overdensities in the region of earth for two potential clustering distributions.	25
1.3	Spin-dependent cross section enhancement factors for some commonly used dark matter search target elements. Data from Reference [16].	39
2.1	Summary of the source of uncertainties in the KATRIN experiment, showing their relative contribution to the measurement of m_ν^2	53
3.1	The event rates at KATRIN for three different neutrino masses and three different mass profiles for the $C\nu B$. Rates are calculated by scaling the results of Ref [17] by the tritium mass of the KATRIN experiment. All rates are given in events/yr.	56
3.2	Error contributions to the $C\nu B$ for four major KATRIN systematics at $m_\nu = 0$ eV. Errors are extended to other masses as a percentage of statistical errors. Note that the error on the final states is limited by Monte Carlo statistics.	59
5.1	Rates of events passing each cut for source-free data with the 10L detector, for 1907000 1 s exposures on each side of the chamber.	103

5.2	Rates of potential physics background events on the surface and underground. Neutron rates from the surface are calculated in [18] and [12] and then scaled by exposure, efficiency, and total neutron flux from [19] for underground. Alpha contamination rates are for the top camera of the 10L detector, measured in data.	108
5.3	Rates of events passing each cut for 87000 5 s exposures on each side of the camera, using the same cuts as for the 1 s data in Table 5.1. Two alpha sources were deployed in the top chamber.	109

Chapter 1

Introduction

1.1 Composition of the Universe

One of the most important achievements of physics in the twentieth century has been the development of theories of the structure and composition of the universe and the collection of experimental evidence to inform and organize those theories. The most precise information about the distribution of the energy budget of the universe has come from the discovery of the cosmic microwave background (CMB) [20] and analysis of its properties. [21] [22]

The CMB provides insight into the composition of the universe through analysis of the multipoles of the acoustic peaks of the anisotropy of the photons. Fitting this for the ‘standard’ six-parameter Λ CDM model, which posits a universe containing hot ‘regular’ matter, cold ‘dark’ matter, and dark energy. In 2011, the WMAP collaboration released their seven-year dataset, which gives the most precise determination of the content: the universe is comprised of $73.4 \pm 2.9\%$ dark energy, $4.48^{+0.113}_{-0.111}\%$ baryonic matter, and $22.0 \pm 1.1\%$ cold dark matter. [23]

1.2 Hot Dark Matter and the Cosmic Neutrino Background

Though the cold dark matter and the dark energy that comprise over 95% of the universe's energy budget present significant mysteries to understanding the universe, even the relatively well-understood baryonic matter holds mysteries of its own. Among these is the cosmic neutrino background (C ν B).

Neutrinos were not first proposed as an astrophysical particle, but rather as a solution to the continuous spectrum of electrons in beta-decaying nuclei. Since neutrinos are electrically neutral and weakly interacting, the advent of experimental neutrino physics was long delayed from the initial proposal of the neutrino. First detection of the neutrino occurred in 1956 by Cowan and Reines at a nuclear reactor. [24] More recently, experimental neutrino physics has focused on the fact that neutrinos are not massless, as initially proposed, but instead, have very tiny masses relative to the other fundamental particles and also have interesting mass-flavor mixing properties. [25]

With greater understanding of the basic properties of neutrinos—though, by no means complete understanding—attention has also now expanded to the role of neutrinos in the cosmos, since, like all other particles, neutrinos were produced during the Big Bang, and have played a role in the evolving universe ever since.

Following the discussions in [26] and [27], while the universe is hot, but after the heavier bosons and fermions have frozen out—temperatures from about 20MeV down to a few MeV—the final remaining species in equilibrium are

$$\gamma \leftrightarrow e^+ + e^- \leftrightarrow \nu_x + \bar{\nu}_x \tag{1.1}$$

with $x = e, \mu, \tau$.

The point at which the neutrinos can no longer maintain their equilibrium can be calculated from noting that freeze-out occurs when the interaction rate of the particles drops below the expansion rate of the universe: $\Gamma_{e^+ + e^- \leftrightarrow \nu_x + \bar{\nu}_x} < H(t)$. At energies small compared with the masses of the W and Z bosons, the neutrino cross section

goes as $G_F^2 E^2$, with $G_F \sim 10^{-5}$, the Fermi coupling constant. The number density of the neutrinos, which are still a relativistic gas, goes as E^3 . Since the average energy can also be described as the temperature of the particles, the interaction rate is thus:

$$\Gamma \simeq \sigma_w n_\nu v \simeq G_F^2 T^5 \quad (1.2)$$

From the standard model of the expansion of the universe for relativistic particles, the expansion rate is given as:

$$H(t) \simeq 1.66 g_\star^{\frac{1}{2}} \frac{T^2}{M_{\text{planck}}} \quad (1.3)$$

where M_{planck} is the Planck mass, 1.2×10^{19} and $g_\star^{\frac{1}{2}}$ is the effective number of statistical degrees of freedom equal to $2 + 2 \cdot (7/4) + 6 \cdot (7/4) = 16$ in this case, for the photons, electron/positrons, and three species of neutrinos/antineutrinos, respectively.

Putting this all together, neutrinos freeze out at approximately

$$T < \left(\frac{1.66 g_\star^{\frac{1}{2}}}{M_{\text{planck}} G_F^2} \right) \sim 2\text{MeV} \quad (1.4)$$

However, the electrons and photons remain in thermal equilibrium until about 0.5-1 MeV, after which the electrons and positrons decouple and the photons are 'reheated' by the process $e^+ + e^- \rightarrow \gamma + \gamma$. This information can predict the current temperature of the CνB.

This is possible because the expansion of the universe is adiabatic, and by setting the entropy before and after the reheating equal, the temperature of the photons before and after can be calculated, and the neutrino temperature is that of the before case. The result is that the neutrino temperature is $T_\nu = \left(\frac{4}{11}\right)^{(1/3)} T_\gamma = 1.95\text{K} = 168\mu\text{eV}$. The neutrino density can likewise be calculated, and the number density of CνB neutrinos is $N_\nu = \left(\frac{3}{11}\right) N_\gamma = 113\text{cm}^{-3}$

Such low energy and density creates a significant problem for the detection of these Big Bang remnant neutrinos (also called cosmic relic neutrinos), as most con-

ventional methods of neutrino detection, such as water Čerenkov or liquid scintillator detectors, have thresholds for detection of neutrino energies many orders of magnitude larger than the $C\nu B$ energy. Therefore, any potential detection method must be thresholdless. One potential method, first proposed by Weinberg in 1962 [28], is to use neutrino capture on beta-decaying nuclei and the effect of the capture on the beta-decay spectrum of that nuclei. This proposal is also advantageous because the theoretical cross-sections for such captures are easily calculable from the beta-decay rate, which is well-known for many nuclei.

The total $C\nu B$ rate depends on the cross-section of ν -capture on the nucleus and the local $C\nu B$ density.

$$R_\nu = n_\nu \frac{N_A M_{\text{eff}}}{A} \int \sigma_\nu v_\nu f(p_\nu) \frac{d^3 p_\nu}{2\pi^3} \quad (1.5)$$

where N_A is Avogadro's number, A is the target atomic number, n_ν is the relic neutrino density, M_{eff} is the effective target mass, σ is the $C\nu B$ cross-section, v_ν and p_ν are the neutrino velocity and momenta, respectively, and $f(p_\nu)$ is the momentum distribution of the relic neutrinos, which is treated as a simple Fermi-Dirac distribution of characteristic temperature T_ν , as calculated above. Table 1.1 shows the result of this calculation for nuclei used in precision beta decay studies, as performed by [17].

Isotope	Half-life (s)	$\sigma(v_\nu/c)(10^{-41}\text{cm}^2)$
^3H	3.8878×10^8	7.84×10^{-4}
^{187}Re	1.3727×10^{18}	4.32×10^{-11}

Table 1.1: Lifetimes and cross sections for neutrino capture on nuclei of interest in beta decay experiments

The second factor in the total $C\nu B$ rate is the local density. Since the neutrinos do have mass, and do interact with matter, albeit rarely, there will be some clustering of neutrinos in galaxies. Ringwald and Wong [29] calculated the predicted overdensity for three neutrino masses and two potential clustering distributions: a Navarro-Frenk-White distributions, which is characteristic of dark matter, and the mass distribution of the Milky Way, which is characteristic of the visible matter in our galaxy. The Milky Way distribution represents the most extreme clustering possible, as it is derived from

the matter that interacts at the greatest rate. The results of their calculation are shown in Table 1.2, with the relevant parameter of overdensity $\frac{n}{\langle n \rangle}$, the local density of neutrinos, divided by the density for a Fermi-Dirac distribution.

Neutrino Mass (eV)	Neutrino Overdensity $\frac{n}{\langle n \rangle}$	
	Navarro-Frenk-White	Milky Way
0.15	1.4	1.6
0.3	3.1	4.4
0.6	12	20

Table 1.2: Cosmic neutrino background overdensities in the region of earth for two potential clustering distributions.

From these predicted $C\nu B$ temperatures, densities, and interaction rates, the expected rates for terrestrial based experiments can be calculated, as will be done for the KATRIN experiment in chapter 3.

1.3 Cold Dark Matter

Cold dark matter is so termed because it is dark matter whose constituent particles have non-relativistic velocities at much earlier times in the development of the universe, unlike the $C\nu B$ discussed above. This “cold” quality is critical for the formation of large scale structure in the universe. Evidence from large scale structure indicates that the clumpiness of matter in the universe is built up from smaller object to larger objects [30], which requires the dominant component of dark matter to be cold, as hot dark matter suppresses small scale structure—a fact which is actually used to search for the neutrino mass [31]. The cold quality of this dark matter also affects the acoustical peaks of the cosmic microwave background, which are informative as to how much dark matter is in the universe. There is some recent evidence from the velocities of satellite dwarf galaxies in the Milky Way [32] and the lack of a dark matter ‘cusp’ at the center of dwarf galaxies [33] that is difficult to reconcile with cold dark matter. Nevertheless, the cold dark matter model has had great success in explaining disparate experimental data, while the nature of the dark matter remains a mystery.

1.3.1 Historical Context

Initial evidence for dark matter came from astronomy and the study of the rotation curves of galaxy clusters and individual galaxies. The predicted velocity of matter in rotating galaxies can be determined from the virial theorem, which for the gravitational potential describes the relationship between kinetic energy (T) and potential energy (U) as

$$\langle T \rangle = -\frac{1}{2} \langle U \rangle \quad (1.6)$$

$$\frac{1}{2}mv^2(r) = \frac{1}{2} \frac{GM(r)m}{r} \quad (1.7)$$

$$v^2(r) = \frac{GM(r)}{r} \quad (1.8)$$

where $v(r)$ is the velocity of matter at a radius r and $M(r)$ is the total mass inside radius r . Since galaxies tend to have most of their mass concentrated in the center of the galaxy, outside of this central region, the velocity of matter should fall off as approximately $r^{-\frac{1}{2}}$.

Fritz Zwicky first studied this effect in 1937 [34], and found that the velocities of the galaxies in the Coma cluster did not follow this distribution, but rather had much higher than predicted velocities at large radii. As instrumentation progressed, this relationship was studied in individual galaxies, notably by Vera Rubin, W. Kent Ford, and their collaborators in the 1970s and 1980s. [35] [36] In these studies, the measured velocity of matter does not decrease with increasing radius, but remains almost constant out to the edge of the measurable region. This implies that $M(r) \propto r$ for all radii with visible matter. Since the density of luminous matter—the stars and interstellar gas—is obviously not proportional to r , this implies that there is some non-luminous matter that extends beyond the visible matter, and is actually the vast majority of the matter. A sample rotation curve from Reference [1] displaying this effect is shown in Fig. 1-1.

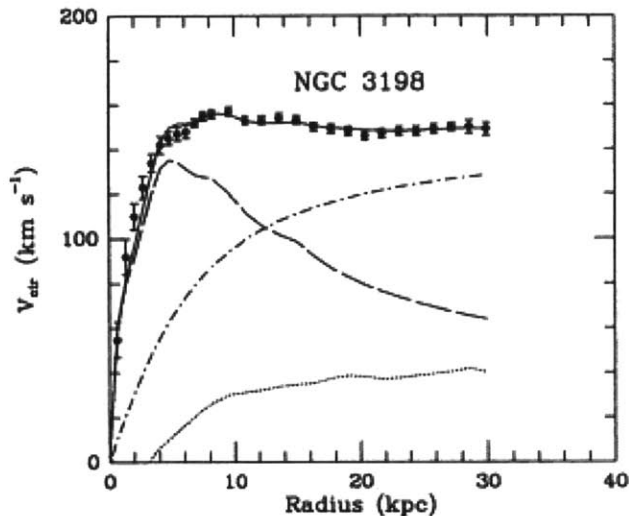


Figure 1-1: A sample rotation curve from the galaxy NGC 9138. [1] The square points show the experimental data. The dashed line shows the velocity component coming from the galactic disc. The dotted line shows the velocity component from the interstellar gas. The dot-dashed line shows the velocity component from dark matter. The solid line shows the sum of the three components.

1.3.2 Dark Matter in the Milky Way

The rotation curve of the Milky Way galaxy can be used in the same way to determine the local dark matter density and the velocity of the sun within the dark matter halo. However, this is significantly more difficult than for non-Milky Way galaxies, due to the geometrical effects of making observations from inside the galaxy being observed. Fig. 1-2 shows the measured rotation curve for the Milky Way, including the the velocity contribution from different mass components of the galaxy.

For ease of calculation, most direct detection dark matter experiments assume an isothermal halo with a Maxwell-Boltzmann distribution of dark matter particle velocities. This halo assumes a density distribution of

$$\rho(r) = \frac{\rho_0}{1 + \frac{r^2}{r_0^2}} \quad (1.9)$$

with ρ_0 and r_0 parameters describing the characteristic density and radius of the halo. In this model, the value of the local density of dark matter is $\rho = 0.3 \frac{\text{GeV}}{c^2} \text{cm}^{-3}$. This number, however, has a significant error associated with it. As described in

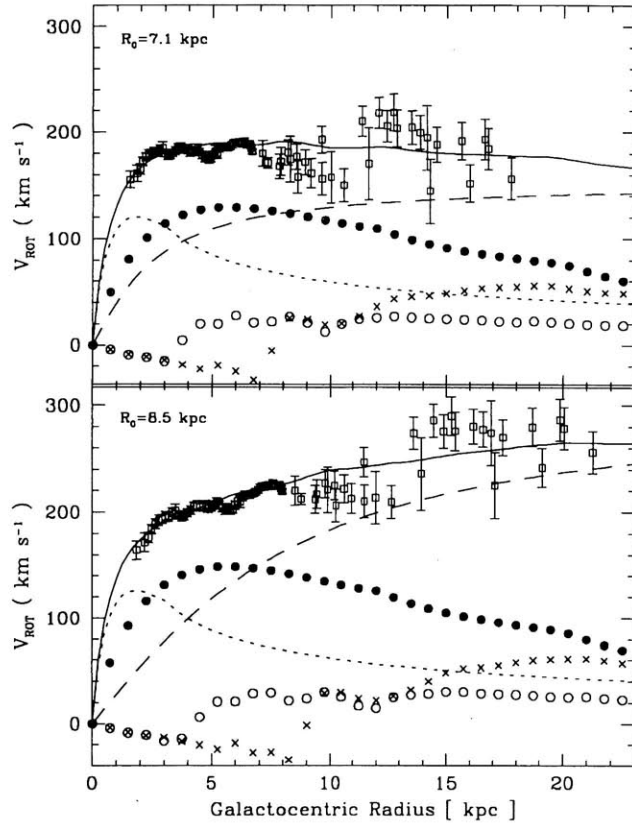


Figure 1-2: The Milky Way rotation curve as calculated in Reference [2]. The two plots show the rotation curve fit for two different measured parameters of R_0 , the distance to the galactic center and Θ_0 , the rotational velocity of the sun around the galactic center. Dashed line shows dark matter contribution, dotted line shows stellar bulge contribution, filled circles show stellar disc contribution, and crosses and open circles show the gas components of HI and H_2 respectively.

References [37] and [2], flattening of the halo or alternative radial profiles have the power to change the local density by a factor of 2. Furthermore, structure in the halo, including rings [38] or disks of dark matter in the galactic plane [39], could also change the local density by a factor of up to 4. Others [40, 41] have also suggested that given new data and simulations and better fitting techniques, the central value should be considered to be closer to $0.4 \frac{\text{GeV}}{c^2} \text{cm}^{-3}$. This work will use the “standard” value, of $0.3 \frac{\text{GeV}}{c^2} \text{cm}^{-3}$, for ease of comparison with other experiments, as the value of ρ amounts to a final scaling factor for cross section determination.

The other quantity calculable from the production of the rotation curve is the velocity of the sun with respect to the halo. A review of galactic constants [42] finds this value for the sun to be $v_c = 220 \pm 20 \text{ km/s}$. In the assumed Maxwell-Boltzmann distribution, that means that the velocity distribution is

$$f(\mathbf{v}) = \frac{1}{(2\pi\sigma^2)^{3/2}} e^{-\frac{|\mathbf{v}|^2}{2\sigma^2}} \quad (1.10)$$

where $\sigma = \sqrt{3/2}v_c = 270 \text{ km/s}$. As with the uncertainty about the local density, there is also uncertainty about the velocity distribution. The effect of this uncertainty is more complicated than the simple scaling of the density uncertainty, but generally has the effect of shifting the effective threshold for a given detector.

1.3.3 Dark Matter Candidates

All of the astrophysical information reviewed so far is informative as to where and how the dark matter affects the structure of the universe, however, the nature of the dark matter remains a mystery. While this work focuses on WIMPs as the dark matter candidate, many dark matter candidate particles and mechanisms have been proposed, as only a few requirements must be met: electrically neutral, weak interactions, and compatible with the known relic abundance and structure formation constraints. A thorough review of dark matter candidates can be found in Reference [43]. Most of these candidates do not have current searches focused on them; in fact, there is only one candidate particle other than the WIMP that has an ongoing

ing direct search—the axion. A brief review of the axion follows, and then a more comprehensive review of the motivation and properties of the WIMP.

Axions

The axion is a theoretical pseudo-scalar neutral boson first proposed to solve the mystery of the CP invariance of the strong force. [44] There is no evidence for CP violation in strong interactions, despite no requirement for this from the standard QCD theory. The axion has a linear relationship to its coupling with a real and virtual photon (Primakoff coupling), $m_a \propto g_{a\gamma\gamma}$. Bounds coming from cosmological, supernovae, red giants, and accelerators have limited the mass (and thus coupling) range of the axion to be dark matter to $0.5 \mu\text{eV} < m_a < 10 \text{ meV}$. [43]

The ADMX experiment has conducted a search using a Sikivie radio frequency cavity over the range $2.0 < m_a < 3.4 \mu\text{eV}$, including some portions of that space with very high resolution, and has seen no evidence for axion dark matter. [45, 46]

Weakly Interacting Massive Particles

The WIMP is the most studied and most favored dark matter particle candidate at the moment. “Weakly Interacting” indicates that the candidate interacts only through gravity and forces weaker than electromagnetism. “Massive” indicates that the particle is massive enough to be non-relativistic at the right time to match structure formation studies in the universe. Usually for weak-scale cross sections, this means that the particle has a mass of greater than 1 keV.

A natural candidate for the WIMP might be a heavy ‘sterile’ (i.e., does not have a charged lepton partner) neutrino that mixes at some small fraction with the Standard Model (SM) neutrinos. While this neutrino would not be stable, its level of mixing can be small enough to make it stable enough over the lifetime of the universe. Constraints on this scenario come primarily from looking for subdominant $N \rightarrow \nu\gamma$ decays in X-ray spectra from astrophysical object, as well as the usual structure formation constraints. A review of the current constraints can be found in Reference [47].

Notwithstanding, the most commonly used WIMP scenario is one in which the

dark matter candidate is a supersymmetric (SUSY) particle. SUSY is a Standard Model (SM) extension that posits a supersymmetric partner for each of the SM particle, where the supersymmetric particle has a spin of $|j - 1/2|$ from its SM partner—e.g. the $+2/3$ -charged, spin- $1/2$ quarks would have $+2/3$ -charged, spin-0 squark superpartners. SUSY is an attractive theory because it not only provides a natural candidate for dark matter, as will be explained, but also addresses several other Standard Model gaps, including possible unification with gravity, the reason for the low mass of the Higgs boson, and the mass scale of electroweak symmetry breaking.

SUSY has three potential dark matter candidates: the neutralino, the sneutrino, and the gravitino. The last two have significant problems in agreement with collider experiment and relic abundance. Thus, the primary SUSY candidate for dark matter is the neutralino χ^0 , which is a linear combination from the fields of the b , W^0 , and Higgs doublets superpartners: the bino, wino, and neutral higgsinos, respectively. Since the SM b , W^0 , and Higgs doublet all have spin 0 or 1, the neutralino superpartner has spin $1/2$. As for the stability of such a particle, it is assured through the introduction of a discrete symmetry R -parity, which also has the benefit of preventing other unwanted features, such as proton decay in excess of current bounds. The R -parity for a given particle is

$$R = (-1)^{3B+L+2S} \tag{1.11}$$

with the baryon number B , the lepton number L , and the spin S . Since superpartners have the same baryon and lepton numbers as the SM particles they are based on, but differ by a $1/2$ unit of spin, it is clear that the SM particles have $R = 1$ and the SUSY particles have $R = -1$. With conservation of R in interactions, it is necessary that in any decay of a SUSY particle, there is a SUSY particle in the final state. This means that the lightest SUSY particle (LSP) is stable. Since, if the LSP is charged, it would bind to nuclei and be detected as anomalously heavy nuclei, and experimental evidence excludes that to a level higher than the predicted abundance of the LSP [48], if SUSY is valid, then the LSP must be neutral—the lightest neutralino—and a good

dark matter candidate.

1.3.4 Interaction Rates and Models

Several authors [49, 50, 51] have produced a thorough and clear derivation of the rates of interaction of non-relativistic particles. The method of Reference [51] is particularly enlightening from the particle physics perspective, as it begins with the recoil between the two particles.

Begin by considering a non-relativistic recoil between a WIMP of mass m_χ and initial velocity v , and a target nucleus initially at rest of mass m_N , final momentum \mathbf{q} . The WIMP recoils with angle θ' relative to its initial direction and the nucleus recoils with angle θ relative to the WIMP initial direction. Momentum and energy conservation demand:

$$\frac{1}{2}m_\chi v^2 = \frac{1}{2}m_\chi v'^2 + \frac{q^2}{2m_N} \quad (1.12)$$

$$m_\chi v' \cos \theta' = m_\chi v - q \cos \theta \quad (1.13)$$

$$m_\chi v' \sin \theta' = q \sin \theta \quad (1.14)$$

Solving these equations for q results in

$$q = 2\mu v \cos \theta \quad (1.15)$$

with μ the reduced mass

$$\mu = \frac{m_\chi m_N}{m_\chi + m_N} \quad (1.16)$$

If we assume that due to large mass and small velocity, the interaction between a WIMP and a nucleus is elastic, the differential cross section for the WIMP-nucleus interaction is

$$\frac{d\sigma}{dq^2} = \frac{\sigma_0}{q_{\max}^2} S(q) \quad (1.17)$$

where $q_{\text{max}}^2 = 4\mu^2 v^2$, σ_0 is the total scattering cross section with a point-like nucleus, and $S(q) = |F(q)|^2$ is the nuclear form factor. The form factor and the dependences of σ_0 will be discussed later.

This cross section can be extended to be doubly differential in the angle of recoil by noting that $d\Omega = 2\pi d\cos\theta$, since the scattering is azimuthally isotropic around the initial direction of the WIMP. Since the relationship between q and $\cos\theta$ is exact (Eq. 1.15), the condition can be imposed with a Dirac δ function:

$$\frac{d^2\sigma}{dq^2 d\Omega} = \frac{d\sigma}{dq^2} \frac{1}{2\pi} \delta\left(v\cos\theta - \frac{q}{2\mu v}\right) = \frac{\sigma_0 S(q)}{8\pi\mu^2 v} \delta\left(v\cos\theta - \frac{q}{2\mu v}\right) \quad (1.18)$$

The next task is to turn this individual event differential cross section into a differential rate given in events per kg per second seen in a detector. To do this, the differential must be transformed using $dq^2 = 2m_N dE_R$, with E_R the recoil energy of the nucleus; multiplication by the number of nuclei N in the target; division by the detector mass $m_N N$; multiplication by the number of WIMPs in the local neighborhood, assumed constant as $\frac{\rho_0}{m_\chi}$; and finally, integration over the velocity distribution of the local WIMPS.

Therefore,

$$\frac{d^2 R}{dE d\Omega} = \frac{2m_N N}{m_N N} \frac{\rho_0}{m_\chi} \int \frac{d^2\sigma}{dq^2 d\Omega} v f(\mathbf{v}) d^3v = \frac{\rho_0}{m_\chi} \frac{\sigma_0 S(q)}{4\pi\mu^2} \int \delta\left(v\cos\theta - \frac{q}{2\mu v}\right) f(\mathbf{v}) d^3v \quad (1.19)$$

This result for the rate is particularly nice, as it exhibits an interesting feature of the recoil spectrum, namely that it is dependent on the Radon transform of the velocity distribution, which is a well-studied transform in the context of differential equations. This makes it easy to calculate the changes to the recoil spectrum by calculating the Radon transform of a test velocity distribution, and potentially, if enough recoils probably of order hundreds, depending on detector resolution can be gathered, to use the inverse transform to determine the velocity distribution. An extensive

description of the Radon transform and its uses in science, including algorithms for the inverse transform, can be found in Reference [52].

For example, taking the isotropic distribution (Eq. 1.10) and putting it into Eq. 1.19 gives the result that the rate is proportional to $e^{\frac{E_R m_N}{2\mu^2 \sigma_v^2}}$.

However, the Earth (and hence any laboratory experiment) is moving through through the halo with some velocity \mathbf{v}_E . This means that from the point of view of an observer at rest on Earth, the velocity distribution is actually

$$f(\mathbf{v}) = \frac{1}{(2\pi\sigma)^{3/2}} e^{-\frac{|\mathbf{v}+\mathbf{v}_E|^2}{2\sigma^2}} \quad (1.20)$$

with the result that

$$\frac{d^2R}{dEd\Omega} = \frac{\rho_0}{m_\chi} \frac{\sigma_0 S(q)}{4\pi\mu^2} \frac{1}{(2\pi\sigma_v^2)^{1/2}} \exp - \frac{\left(\mathbf{v}_E \cdot \hat{\mathbf{q}} + \frac{q}{2\mu}\right)^2}{2\sigma_v^2} \quad (1.21)$$

where $\frac{q}{2\mu}$ can also be called v_{min} , the minimum velocity a particle must have to produce a recoil of energy E_R .

The velocity of the Earth has three components

$$\mathbf{v}_E = \mathbf{v}_r + \mathbf{v}_\odot + \mathbf{v}_O \quad (1.22)$$

where $\mathbf{v}_r = (0, 220, 0)$ km/s is the sun's rotational velocity in the galaxy given in galactic coordinates, $\mathbf{v}_\odot = (9, 12, 7)$ is the sun's proper motion with respect to the nearby stars, and \mathbf{v}_O is the orbital velocity of the earth around the sun. Since the dominant component of the velocity is the second rotational component and the Earth's orbital velocity is small compared to this, typically only the component of the sun's motion parallel to this component is calculated.

$$\mathbf{v}_O = |v_O| \cos \xi \cos 2\pi t \quad (1.23)$$

where $|v_O| \approx 30$ km/w, $\cos \xi \approx 60^\circ$ is the angle of inclination of the earth's orbit with respect to the galactic plane, and t the time in years from June 2.

Both Eq. 1.21 and Eq. 1.23 produce interesting results that can be used to dis-

tinguish dark matter signals in the lab. Eq. 1.23 means that the magnitude of the Earth's velocity changes sinusoidally over the course of a year, and as a result, the energy spectrum of recoils will change over the course of a year. This is shown in Fig. 1-3. This effect is relatively small, of order 1-10%, depending on the energy threshold and material of a detector.

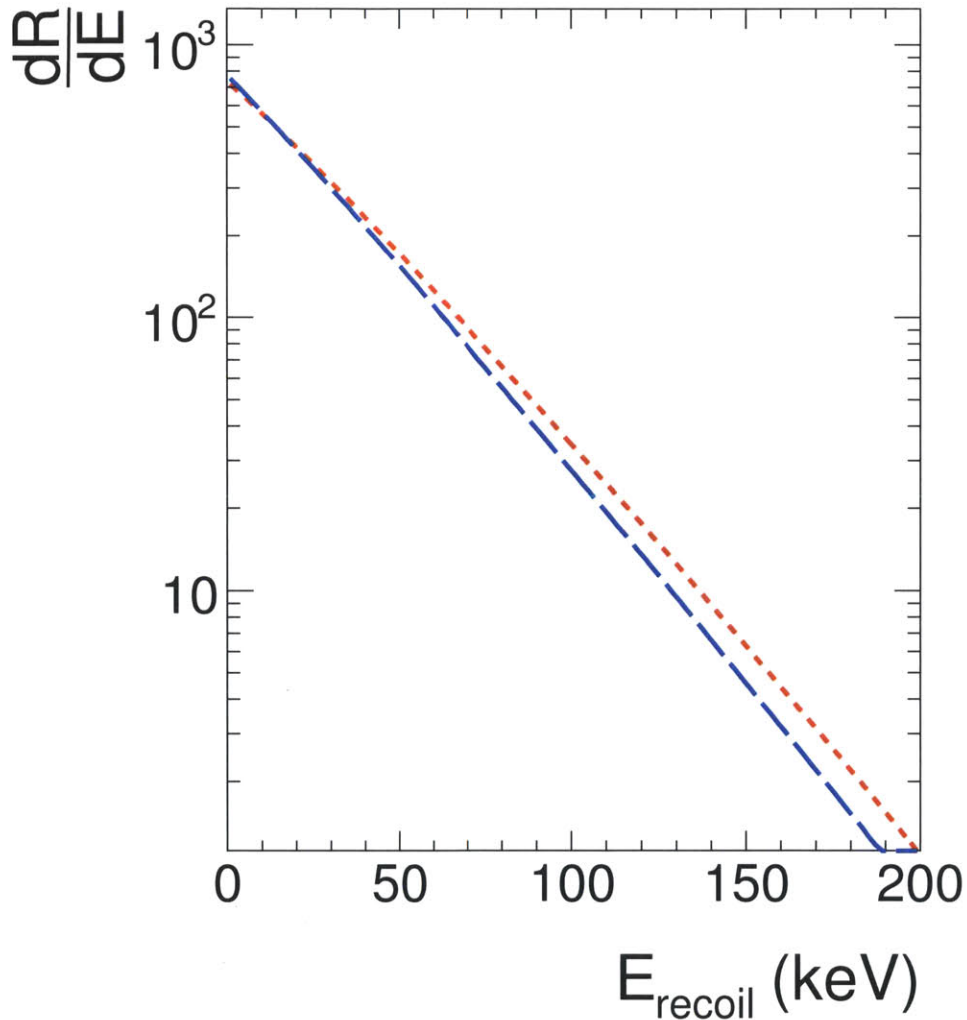


Figure 1-3: The difference in recoil energy spectra for the maximum (red dotted line) and minimum (blue dashed line) earth velocity through the year. The example target is a ^{19}F nucleus and the WIMP is 100 GeV. Note that recoils get pushed to lower energies when the relative earth velocity is at a minimum.

Eq. 1.21 also has intriguing implications if the recoil direction of the target nucleus

is measurable. In this case, there is a significant directional asymmetry observable in the recoil direction. This is shown visually in Fig. 1-4, where $\cos \gamma = \frac{v_E \cdot \hat{q}}{v_E}$ from Eq. 1.21 this shows that the recoiling nuclei are aligned with the incident dark matter particles in a preferred and theoretically predicted direction. This asymmetry is large, of order 1 and the experimental realization of this measurement will be the focus of this work. Green and Morgan have done several theoretical studies [53, 54, 55, 56] probing the magnitude and variations in this effect, and have shown that a positive dark matter detection can be made with very few events, if the reconstruction of the detector is sufficient. One of the interesting points to note is that this effect is only weakly dependent on the velocity distribution $f(v)$; they show the effect to be robust across a few different velocity models.

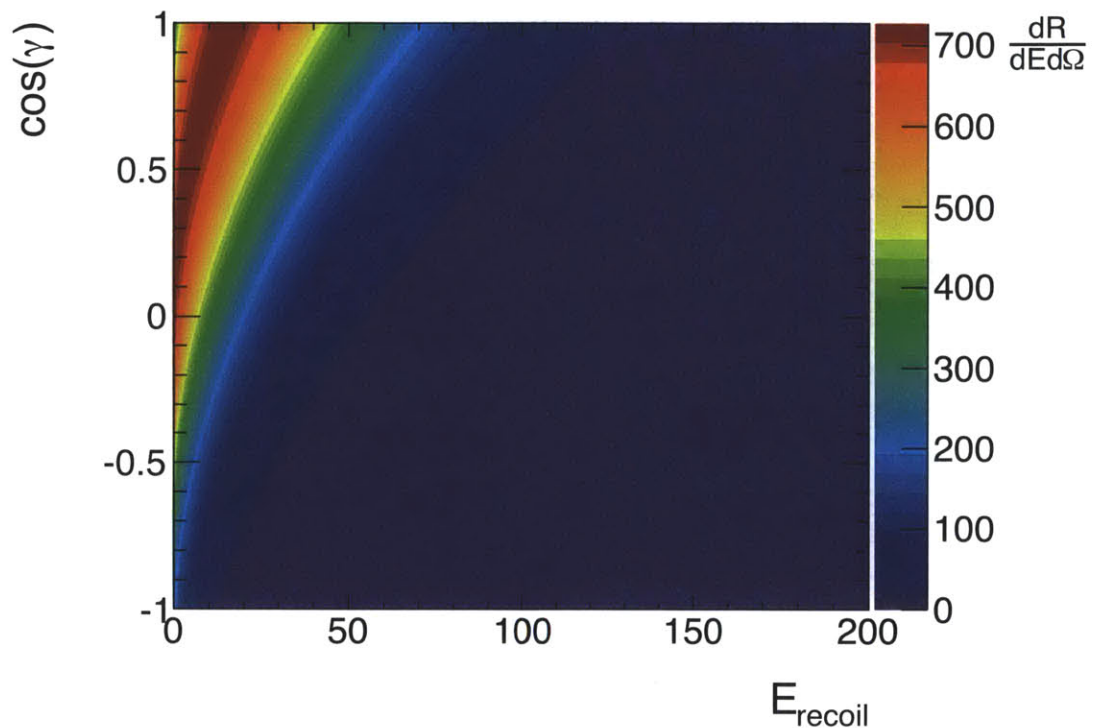


Figure 1-4: The WIMP interaction rate as a function of recoil energy and angle between recoil and the direction of the motion of the Earth. The example target is a ^{19}F nucleus and the WIMP is 100 GeV.

Hitherto, nothing has been said about the connection between the SUSY model of dark matter and the recoil rates. The following will deal with that connection,

and the effect of the form factor on the interaction rates. In general, if the LSP is a fermion, as in the case of the neutralino, the Lagrangian will contain the following terms:

$$\mathcal{L} \supset \alpha_q^A (\bar{\chi} \gamma^\mu \gamma_5 \chi) (\bar{q} \gamma_\mu \gamma_5 q) + \alpha_q^S \bar{\chi} \chi \bar{q} q + \alpha_q^V \bar{\chi} \gamma_\mu \chi \bar{q} \gamma^\mu q \quad (1.24)$$

where $\alpha_q^{A,S,V}$ are the quark-neutralino axial, scalar, and vector couplings, respectively. The first contributes to the spin-dependent coupling and the latter two to the spin-independent coupling. As a result, the factor $\sigma_0 S(q)$ can be decomposed as

$$\sigma_0 S(q) = \sigma_0^{SI} S^{SI}(q) + \sigma_0^{SD} S^{SD}(q) \quad (1.25)$$

Spin-Independent Cross Sections and Form Factors

The scalar term of the Lagrangian contributes as

$$\sigma_0^{SI,S} = \frac{4\mu^2}{\pi} (Z f^p + (A - Z) f^n)^2 \quad (1.26)$$

with Z the atomic number of the target and A the atomic mass, and f^p and f^n given by

$$\frac{f^p}{m^p} = \sum_{q=u,d,s} \frac{\alpha_q^S}{m_q} f_{Tq}^p + \frac{2}{27} f_{TG}^p \sum_{q=c,b,t} \frac{\alpha_q^S}{m_q} \quad (1.27)$$

$$\frac{f^n}{m^n} = \sum_{q=u,d,s} \frac{\alpha_q^S}{m_q} f_{Tq}^n + \frac{2}{27} f_{TG}^n \sum_{q=c,b,t} \frac{\alpha_q^S}{m_q} \quad (1.28)$$

and $f_{Tq}^{p,n}$ are the contributions of the light quarks to the mass of the proton of neutron and $f_{TG}^{p,n}$ are the contributions of the gluons and other sea quarks to the mass: $f_{TG}^{p,n} = 1 - \sum_{q=u,d,s} f_{Tq}^{p,n}$. The f_{Tq} s are experimentally determined and given in Reference [57]. Since, however, $f^p \approx f^n$ and so

$$\sigma_0^{SI,S} = \frac{4\mu^2}{\pi} (A f^p)^2 \quad (1.29)$$

This indicates that heavier elements are a better choice to probe this aspect of

the cross section, as they are highly enhanced.

The vector term of the Lagrangian contributes only for Dirac fermions, and is

$$\sigma_0^{SI,V} = \frac{\mu^2 B^2}{64\pi} \quad (1.30)$$

with $B = \alpha_u^V(A + Z) + \alpha_d^V(2A - Z)$, as this term only depends on the valence quarks. The neutralino, however, is typically considered to be a Majorana particle, and this term is ignored.

The form factor in the spin independent case is usually parametrized as

$$S(q) = \left(\frac{3j_1(qR)}{qR} \right)^2 e^{-q^2/s^2} \quad (1.31)$$

where $j_1(x) = \frac{\sin x - x \cos x}{x^2}$ is the first spherical Bessel function, and R is a parameter characterizing the size of the nucleus, typically $R \simeq 0.89A^{1/3} + 0.3$ fm and s is a skin depth parameter, taken $s \simeq 1$ fm.

Spin-Dependent Cross Sections and Form Factors

The spin dependent component of the cross section for a fermionic WIMP takes the form¹

$$\sigma_0^{SD} = \frac{32\mu^2}{\pi} \left(\frac{1}{J} (a_p \langle S_p \rangle + a_n \langle S_n \rangle) \right)^2 J(J+1) \quad (1.32)$$

where

$$a_p = \sum_{q=u,d,s} \frac{\alpha_q^A \Delta_q^p}{\sqrt{2}}, a_n = \sum_{q=u,d,s} \frac{\alpha_q^A \Delta_q^n}{\sqrt{2}} \quad (1.33)$$

and $\langle S_{p,n} \rangle$ is the expectation value of the spin component for the proton or neutron group of the nucleus and the $\Delta_q^{p,n}$ s are related to the matrix elements of the axial-vector current in the nucleon, and are calculable from nuclear models, and also given in Reference [57].

¹The usually referenced versions of equations 1.32 and 1.33 have a factor proportional to G_F^2 in σ_0 and inverse factors of G_F in a_p and a_n . These cancel and so are omitted for clarity.

The factor $\frac{1}{J}(a_p \langle S_p \rangle + a_n \langle S_n \rangle) \equiv \lambda$ is termed the Landé factor, and a listing of $\lambda^2 J(J+1)$ of elements commonly used in dark matter experiments is in Table 1.3, using the values from Reference [16], which are calculated using the odd-group model.

Unpaired Proton		
Isotope	J	$\lambda^2 J(J+1)$
^{19}F	1/2	0.647
^{23}Na	3/2	0.041
^{127}I	5/2	0.023
Unpaired Proton		
Isotope	J	$\lambda^2 J(J+1)$
^{29}Si	1/2	0.063
^{73}Ge	9/2	0.065
^{129}Xe	1/2	0.124
^{131}Xe	3/2	0.055

Table 1.3: Spin-dependent cross section enhancement factors for some commonly used dark matter search target elements. Data from Reference [16].

The form factor for the spin-dependent component is taken as

$$S(qr_n) = \begin{cases} j_0^2(qr_n) & \text{if } qr_n < 2.55 \text{ or } qr_n > 4.5.; \\ 0.047 & \text{if } 2.55 \leq qr_n \leq 4.5. \end{cases} \quad (1.34)$$

with $j_0(x) = \frac{\sin x}{x}$ and $r_n \simeq A^{1/3}$.

Alternatively,

$$S(q) = a_0^2 S_{00}(q) + a_0 a_1 S_{01}(q) + a_1^2 S_{11}(q) \quad (1.35)$$

where $a_0 = a_p + a_n$ and $a_1 = a_p - a_n$, but the parameters S_{ij} must be determined experimentally for any given element.

1.3.5 Current Results from Dark Matter Experiments

There is an extensive suite of direct dark matter experiments currently underway. Experiments are using a variety of techniques and target elements in order to eliminate backgrounds and cross-check systematics.

Non-Modulation Experiments

The non-modulation experiments aim to build detectors with large mass, low energy threshold, and low background in order to be as sensitive as possible. Typically, these experiments are built with a way to separate electronic recoils (not dark matter) with nuclear recoils (dark matter candidate), and placed deep underground in order to be shielded from cosmogenic neutrons and other backgrounds.

One subclass of these experiments is the liquid noble element detectors, where a liquid noble target region is read out with photomultiplier tubes. The addition of a gas ‘phase’, also read out with PMTs can add electronic-nuclear separation. The most popular noble for these experiments is xenon, as it is an element with both very large atomic mass—important for spin-independent detection—and two spin-sensitive isotopes (see Table 1.3). However, research is ongoing for also using liquid argon and liquid neon targets, as they may present better electronic-nuclear separation. The most advanced collaboration in this group of experiments is the XENON100 collaboration [3], whose limit is shown in Fig. 1-5.

Another subclass of experiments is the cryogenic bolometer detectors, where a heat from a nuclear recoil deposited in a dielectric crystal is read out with thermistors. The addition of an ionization collection method can provide electron-nuclear separation. Germanium is the favored element for this kind of detector, for its large mass. The most advanced collaboration in this group of experiments is CDMS [4], whose limit is shown in Fig. 1-5.

A third subclass of experiments uses scintillator crystals read out with phototubes. Sodium iodide crystals are the most commonly used crystals, though cesium iodide has also been used. This technique is challenging on the experimental side due to the difficulty of producing radiopure crystals. The most successful group to do this is the DAMA/LIBRA experiment, which claims a positive detection of dark matter as will be discussed below. The KIMS experiment [10], using CsI crystals, has set the best spin-dependent limit at high dark matter masses, as shown in Fig. 1-6.

The last class of experiments in this group are the superheated liquid bubble

chambers, where fluid is kept in a metastable superheated state and nuclear recoils nucleate bubbles within the fluid. The bubbles are photographed. This technique excludes electronic recoils as background by tuning the state of the fluid. The most advanced collaboration using this technique is the COUPP experiment [9], using CF_3I as the detection medium, and whose spin-dependent limit is shown in Fig. 1-6.

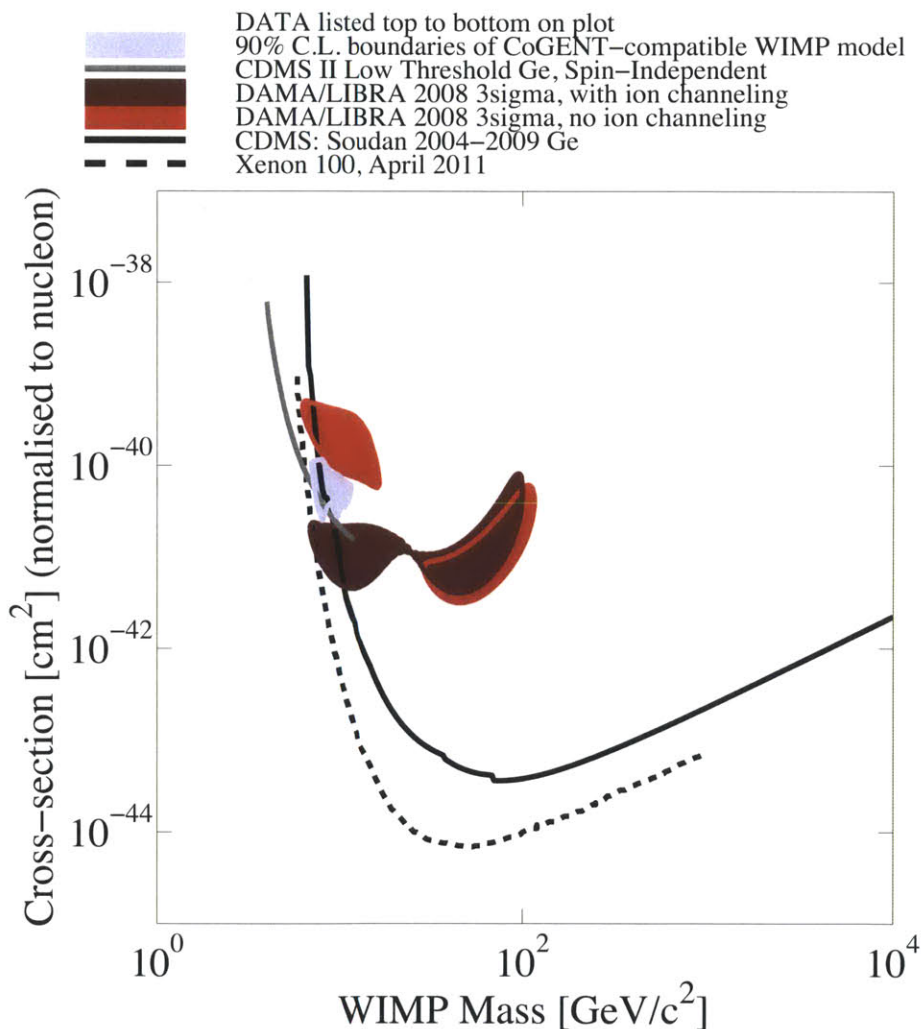


Figure 1-5: Current WIMP spin independent cross section limits. Dotted black line shows the XENON100 results [3]. Solid black line shows the CDMSII results [4]; solid grey line shows the CDMSII low threshold analysis results. [5]. Dark red and light red regions show the allowed regions for DAMA/LIBRA under the assumptions of ion channeling and no ion channeling, respectively. [6]. Solid light blue area shows the allowed region for the CoGENT experiment. [7]. Plot made using DMTools. [8]

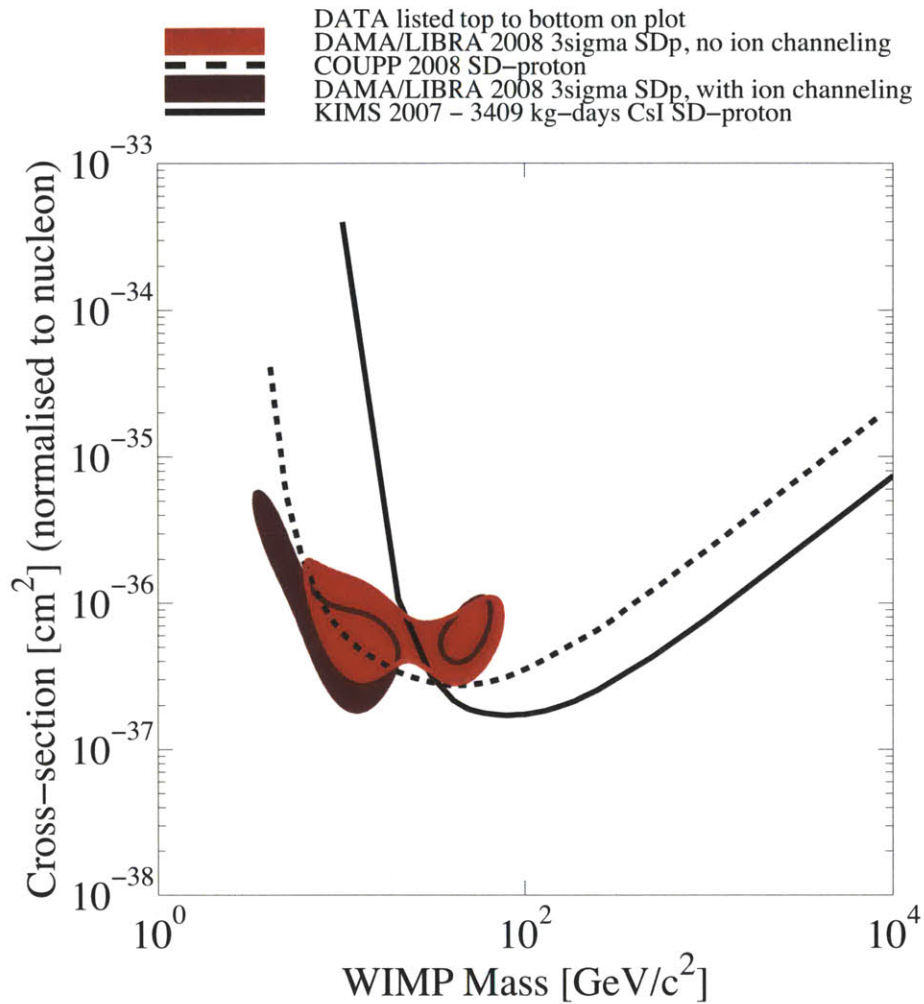


Figure 1-6: Current WIMP spin dependent cross section limits, normalized to the proton. Dotted black line shows the COUPP limit. [9]. Solid black line shows the KIMS limit. [10] Dark red and light red regions show the allowed regions for DAMA/LIBRA under the assumptions of ion channeling and no ion channeling, respectively. [6]. Plot made using DMTools. [8]

Annual Modulation Experiments

As discussed in section 1.3.4 and shown in Fig. 1-3, the rate of the dark matter recoils varies over the year as the Earth orbits the Sun. Two experiments have searched for dark matter using this annual modulation and have seen positive results. The DAMA/LIBRA collaboration uses 250kg of NaI(Th) crystals and operates in the Gran Sasso Laboratory in Italy. They have operated for over a decade, and have seen a consistent oscillation of their recoil rates over that period, as shown in Fig. 1-7, with the promising property that they achieve the correct phase for their modulation, peaking in early June. [6] However, their results are in some tension with other results, as shown in Figs. 1-5 and 1-6.

The other experiment to do this search is the CoGeNT experiment, which is a Ge bolometer-type experiment running in the Soudan mine in Minnesota, USA that focuses on pushing their energy threshold as low as possible. They report a modulated signal over approximately one year of running [7], shown in Fig. 1-8(a). Their phase, however, is approximately one month out of phase with the DAMA/LIBRA result, and their allowed region of phase space is in tension with the DAMA/LIBRA allowed region, as shown in 1-8(b).

Directional Experiments

Finally, in the past few years, a community of dark matter searches exploiting the directionality of Eq. 1.21 has arisen. There are many proposals of how to search for directional recoils, primarily using low pressure gas detectors. These gas detectors have coalesced around CF_4 gas, for its high fluorine content, and thus sensitivity to spin; and CS_2 because of experimental benefits of low diffusion and a medium-heavy (32 amu) S atom. Xenon gas and ^3He mixtures have also been proposed, for better sensitivity for spin-independent and low dark matter mass interactions, respectively.

The DRIFT experiment [58] is a 1 m^3 multi-wire proportional chamber with 2 mm wire pitch using 40 torr CS_2 gas. Because in CS_2 the ion is drifted instead of the electrons, the diffusion of the gas is quite low, and spatial resolution is approximately

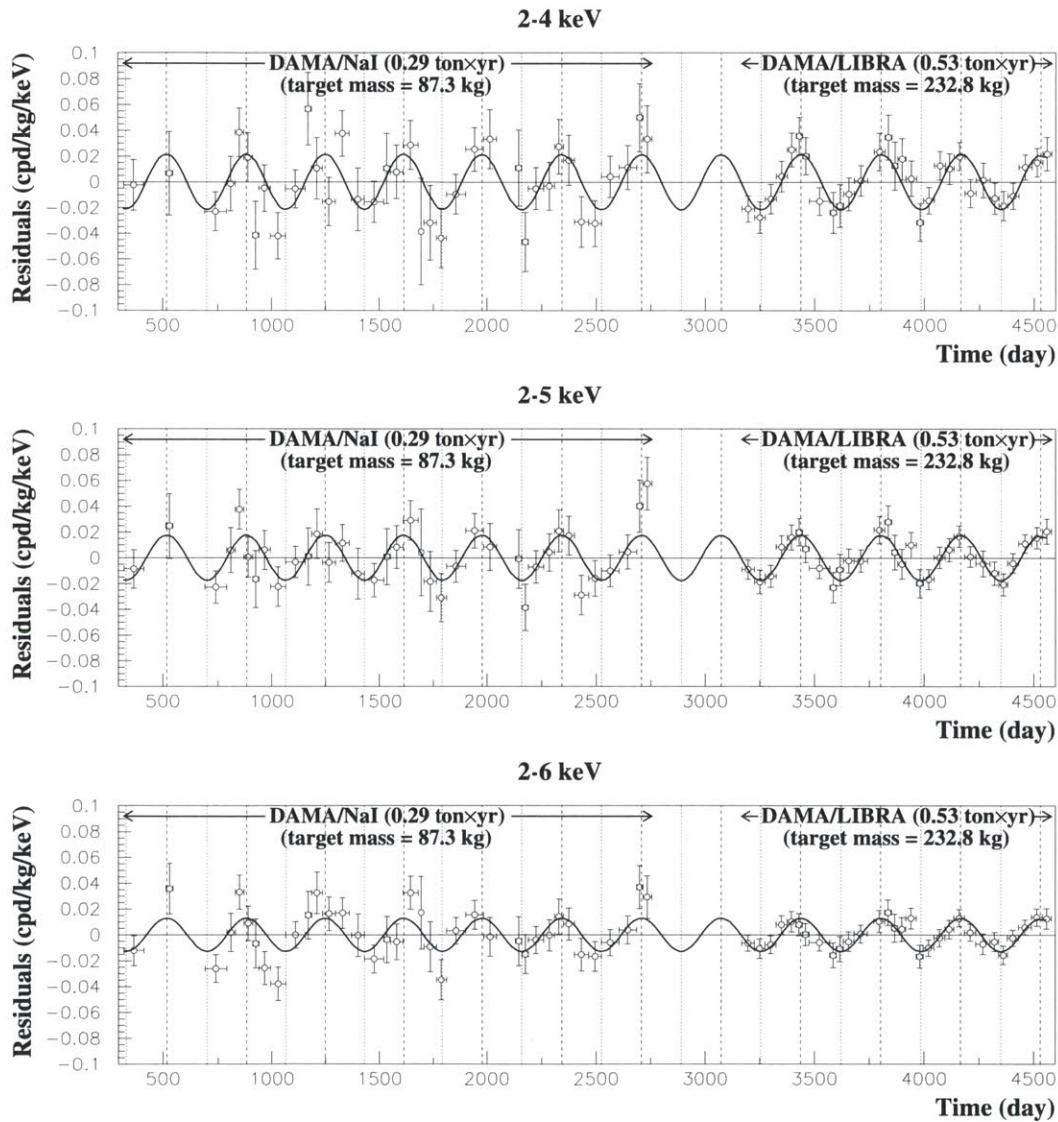
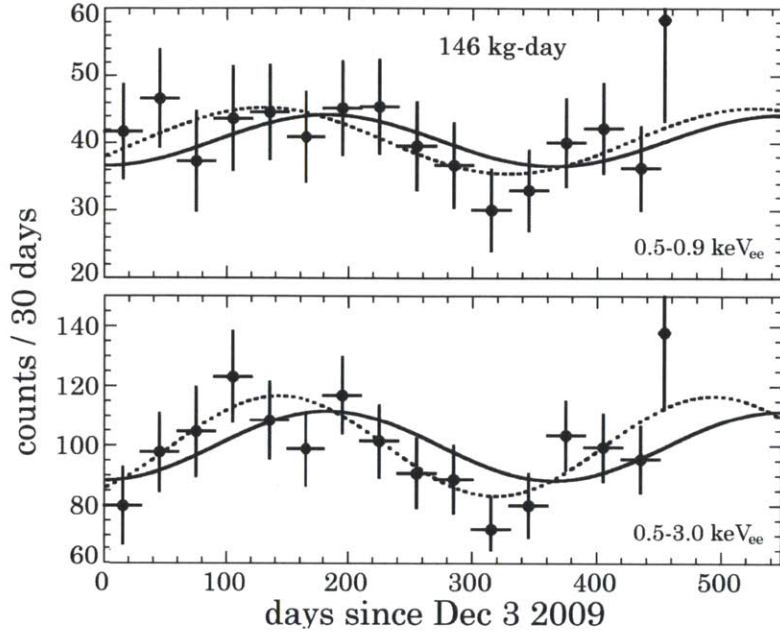
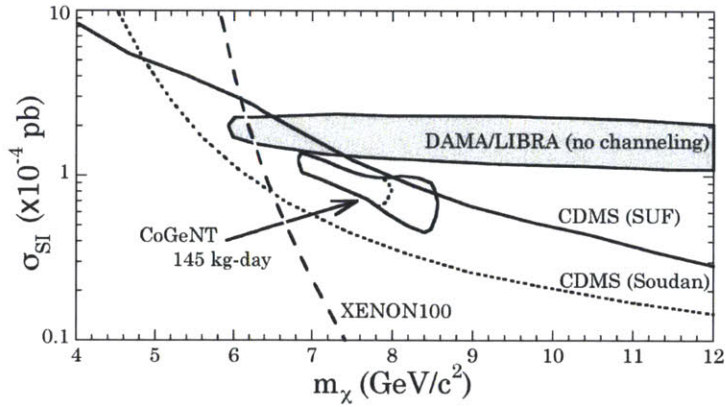


Figure 1-7: Residual rates from the yearly average for the DAMA/LIBRA experiment in different energy bins. [6] The x-axis is time in days since the beginning of the experiment. The solid line shows the predicted oscillation, with the amplitude fit in each energy bin. Dashed and dotted lines show maxima and minima, respectively.



(a) Event rates from the CoGeNT experiment. [7] Dotted line shows the best fit oscillation; solid line shows the model prediction.



(b) Allowed region for the CoGeNT experiment. [7] Results from the CDMS and XENON100 experiments are also shown.

Figure 1-8: Recent results from the CoGeNT experiment.

2 mm. The detector has also been operated with a mix of 30 torr CS_2 and 10 torr CF_4 to increase the spin-dependent sensitivity. With this gas mixture, the DRIFT detector was operated for 47.4 live days underground in 2009 the Boulby mine in England and reported their results in Reference [59].

The NEWAGE experiment [13] is a $(0.3\text{m})^3$ CF_4 -based experiment using μ -PICs for charge readout, which pixelate readout at a $400\ \mu\text{m}$, which in conjunction with timing information, allows for three-dimensional reconstruction of a potential tracks. This detector was operated underground at the Kamioka Observatory in Japan for just under three months, and their limit is reported in the same reference.

The MIMAC experiment [60] has also built a prototype detector using micromegas segmented into $300\ \mu\text{m}$ pixels, which, like the NEWAGE μ -PICs, allow for full 3D reconstruction. They aim to use CF_4 , ^3He , CH_4 , or some combination thereof to search for dark matter. The addition of the lighter gases allows for lower energy thresholds, which is a benefit in dark matter searches. The collaboration is currently preparing a larger prototype detector.

Chapter 2

The KATRIN Experiment

The Karlsruhe TRItium Neutrino experiment is an experiment located at the Karlsruhe Institute of Technology in Karlsruhe, Germany, dedicated to studying the tritium beta decay spectrum in order to study the mass properties of the neutrino. Because the neutrinos resulting from the decay of the tritium are difficult to detect, the experiment instead relies on studying the electrons resulting from the decay, which give an indirect measure of the properties of the neutrino.

KATRIN is arranged in a linear fashion, as shown in Fig. 2-1, beginning with a tritium source on one end and ending at an electron detector at the other end. The following sections describe these and the other components of the experiment.

2.1 Tritium Source

KATRIN's tritium source is composed of T_2 gas, which is injected into the center a 10 m long, 90 mm diameter tube and pumped out at both ends of the tube. The gas is cooled to 27 K to eliminate the contribution of kinetic energy of the gas molecules to the decay system. The source additionally sits in a magnetic field that guides decay electrons along the field lines towards the rest of the detector. The magnetic field is 3.6 T over the source, increasing to 5.96 T after the end of the differential pumping section. The relationship between these fields governs the maximum angle of acceptance of decay electrons from the source: $\sin^2(\theta_{max}) = B_{source}/B_{max} = \frac{3.6}{5.96}$,

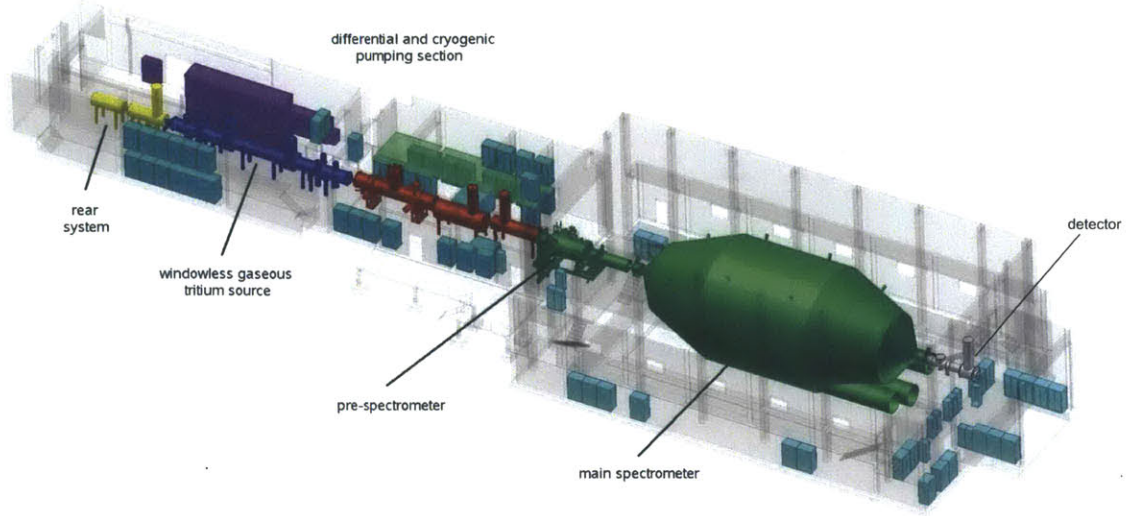


Figure 2-1: The KATRIN detector, showing the major components of the system: rear system (yellow), source (blue), transport section (red), spectrometers (green) and detector (grey).

with the result that $\theta_{max} = 51^\circ$, where θ is measure off of the field lines, which run longitudinally down the apparatus.

One critical number for KATRIN is the amount of tritium instantaneously measurable by the detector. This can be calculated as follows. The number of T_2 molecules is

$$N = A_s \cdot \epsilon_T \cdot \frac{\Delta\Omega}{2\pi} \cdot \rho d \cdot P_0 \quad (2.1)$$

where A_s is the cross sectional area of the source, 56.52 cm^2 at KATRIN, $\epsilon_T = 0.95$ is the tritium purity, $\frac{\Delta\Omega}{2\pi}$ is the solid angle acceptance of the source, with a value of $1 - \cos(51^\circ)$, $\rho d = 5 \times 10^{17}$ is the column density, and P_0 is the probability of an electron making it through the source without scattering, which has the value of 0.413 for the experimental column density and angular acceptance. This means that the total number of instantaneously available tritium molecules is 4.1×10^{18} , or 40.7 micrograms. For an explanation of the factors required in determining these experimental parameters, see reference [61].

2.2 Transport Section

After decay, the electrons from the tritium decay must be transported out of the tritium source, maintaining their precise energy, while also preventing any tritium from following, as downstream tritium decays adversely affect the experiment. This separation between electrons and tritium is accomplished with two methods. The first is a differential pumping station that draws most of the tritium out of the source, as well as having sections that bend at 20° , through which the charged electrons can be guided, but the neutral tritium cannot. Downstream from this, there are two cryogenic pumping stations where tritium is cryo-sorbed onto the cold surface of the transport tube. Again the transport tube is directed so as to facilitate adsorption of the tritium. These two methods combined should reduce the tritium flow into the spectrometers to 10^{-14} mbar l/s, which keeps the background rate at the detector below 10 mHz.

2.3 Rear Section

On the opposite side of the tritium source from the transport section is the rear section. This section has two purposes: removing tritium from the source in a way to keep the longitudinal source profile symmetric around the insertion point and to monitor and calibrate the tritium source. The section contains a differential pumping station similar to the downstream station and an electron detector to monitor the rate of electrons coming off the back of the tritium source. There is also a pulsed electron source installed in this section that will allow monoenergetic electrons to be shot down the entire apparatus for the purpose of calibration and mapping any inhomogeneities.

2.4 Spectrometers

The spectrometers are the workhorse of the KATRIN experiment. They are the component of the facility that allows for the precise, 1 eV energy resolution of the

experiment. There are two spectrometers, the pre-spectrometer and the main spectrometer. The pre-spectrometer is designed as both an initial filter reducing the rate of electrons entering the main spectrometer and also as a test facility for methods and components for the entire experiment.

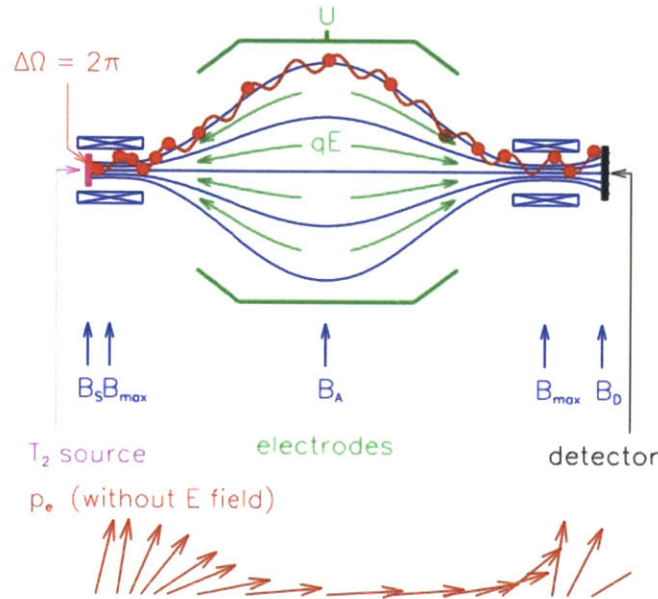


Figure 2-2: Schematic of a MAC-E-Filter, showing the longitudinal locations of important fields. The arrows along the bottom show the change in transverse energy to longitudinal energy in the filter.

The spectrometers are designed as MAC-E-Filters—Magnetic Adiabatic Collimation with Electrostatic Filters. A diagram of this process is shown in Fig. 2-2. These filters utilize a slow (adiabatic) change in magnetic field to convert transverse (perpendicular to the long axis of KATRIN) kinetic energy of electrons into longitudinal (parallel to the long axis) kinetic energy. The magnetic moment μ , is defined for non-relativistic particles as

$$\mu = \frac{E_{\perp}}{B} = \text{constant} \quad (2.2)$$

So it is clear that if B , the magnetic field is decreased, the transverse kinetic energy must also be reduced. If this happens in an environment where the particle's total kinetic energy is unchanged, this excess transverse energy has nowhere to go but into

longitudinal kinetic energy. If, then, a retarding electric potential is applied at the point of minimum magnetic field, the particle will pass through this electrostatic filter if the longitudinal energy of the particle is greater than qU , where U is the retarding potential. This means that the energy resolution of this method is dependent only on the ratio of the maximum and minimum magnetic fields:

$$\frac{\Delta E}{E} = \frac{B_{min}}{B_{max}} \quad (2.3)$$

However, if no flux of particles is to be lost, it also means that the total area that the magnetic field lines pass through is inversely proportional to the magnetic field, or:

$$\frac{B_{min}}{B_{max}} = \frac{A_{max}}{A_{min}} \quad (2.4)$$

This means that to achieve the intended energy resolution of KATRIN, $\frac{\Delta E}{E} = \frac{1}{20000}$, the main spectrometer must be extremely large, 23.3 m long and 9.8 m in diameter. This scale has presented many challenges for the experiment, including the vacuum system and the electrostatic system design. Nevertheless, those challenges have been met, and the main spectrometer will achieve 10^{-12} mbar vacuum, which is necessary to maintain a background below 0.01 Hz, and electrostatic stability of sub-volt precision, which is necessary to preserve the resolution guaranteed by the magnetic fields.

2.5 Detector

The final section of KATRIN is a detector to count the electrons that pass through both spectrometers. This detector is a silicon semi-conductor detector with an energy resolution of about 600 eV. This circular detector is segmented into 148 equal-area pixels in order to study any the spatial inhomogeneities that may be present in the system. There is also an electrode just before the detector, which accelerates the electrons from their initial energy by about 30 keV. This allows discrimination from backgrounds which may be present close to the detector, and also lowers the effec-

tive threshold of the detector, which may assist in studying low-energy backgrounds present in the source or spectrometer.

2.6 Uncertainties and Reach

Various aspects of the experimental design give rise to systematic uncertainties on the measurement of the electron neutrino mass. This section will briefly describe those uncertainties and give their predicted values, as well as an overall estimation of the reach of the KATRIN experiment.

Most of the systematic uncertainties come from the tritium source. These can be divided into two categories: physics uncertainties, which are comprised of uncertainties coming from physics properties and interactions of particles and molecules; and experimental uncertainties, which are comprised of uncertainties that are based in the experimental set up and the ability of the experiment to track variations in the source.

In the physics category, there are uncertainties that come from the description of the rotational and vibrational final states of the T-He molecule, which imparts some smearing to the decay spectrum this has been calculated but not measured, and since it directly impacts the energy of the decay electron, it has a relatively large contribution to the error. Additional errors include the concentration of T⁻ ions in the gas, which, when they decay may contaminate the spectrum and elastic electron-tritium scattering, which may non-uniformly change the direction of the electron.

In the experimental category, there are uncertainties that come from the monitoring of the column density (that is, the number of tritium ions in the source), which is based on the ability to monitor the source purity, temperature, pressure, and knowledge of the decay rate; the monitoring of electric potential variations in the source; and the monitoring of magnetic field variations in the source. Some of these uncertainties have gotten better since the initial design report, particularly the resolution on the high voltage stability [62], which affects the electric potential variation error, and the ability to measure the temperature of the tritium [63], which affects

the column density monitoring error. A final accounting of these errors, of course, can only be made when the experiment is operational.

There are also uncertainties that come from the spectrometer and detector sections, which include the errors on the determination of the transmission function through the spectrometer, which itself includes the uncertainty from inelastic ; the slope of the background rate—whether it is constant over all potentials in the spectrometer; and variations in the electric potential in the spectrometer.

These uncertainties and an estimation of the statistical uncertainty are show in Table 2.1.

Source of Error	Contribution to $\sigma(m_\nu^2)$ [10^{-3} eV ²]
Final state description	< 6
T ⁻ ion concentration in T ₂	<0.1
Elastic e ⁻ -T ₂ scattering	< 5
Column density monitoring	< $\frac{\sqrt{5} \cdot 6.5}{10} = 1.45$
Source electric potential variations	< 0.2
Source magnetic field variations	< 2
Transmission function determination	<6
Background slope	< 1.2
Spectrometer potential variations	< 5
Total systematic uncertainty from these sources	11
Total systematic error with contingency	17
Total statistical error	18
Total error	25

Table 2.1: Summary of the source of uncertainties in the KATRIN experiment, showing their relative contribution to the measurement of m_ν^2 .

In predicting a final systematic uncertainty, KATRIN has allowed for sources of systematic error equal to the known sources as a contingency for as-yet undiscovered sources of error. This makes KATRIN an experiment nearly equivalent in systematic and statistical error. Using these numbers, KATRIN has predicted its reach for a 3 year, 10 month run, as shown in Fig 2-3. KATRIN has 5- σ discovery potential at 0.35 eV and a 90% bound setting sensitivity at 0.2 eV.

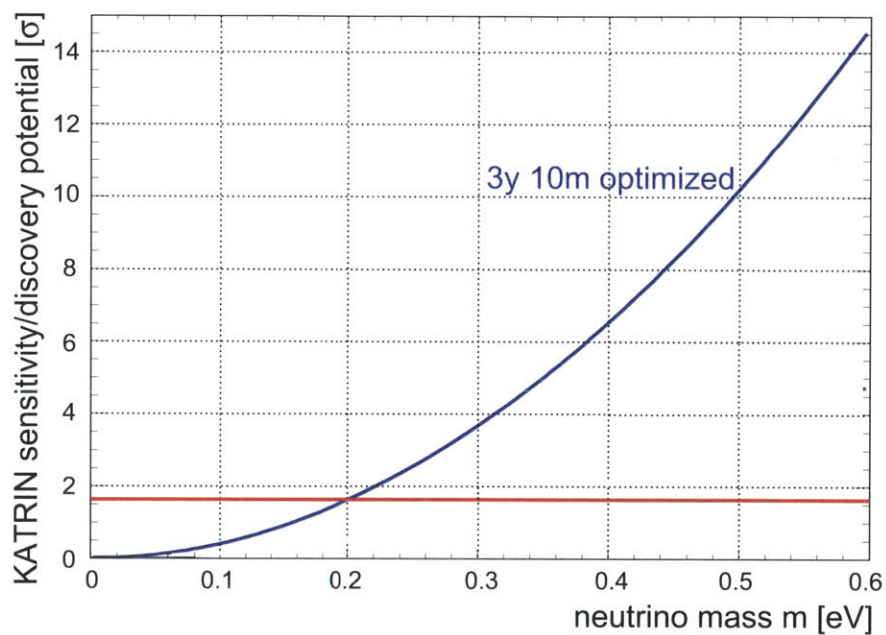


Figure 2-3: The sensitivity and discovery potential of the KATRIN experiment as a function of neutrino mass, described in number of sigma away from zero. Horizontal red line shows the 90% confidence limit bound. KATRIN thus has 5- σ discovery potential at 0.35 eV and a 90% bound setting sensitivity at 0.2 eV.

Chapter 3

The Cosmic Neutrino Background at KATRIN

The KATRIN experiment provides a laboratory for investigating the $C\nu B$ on Earth. Tritium appears as a very promising isotope for $C\nu B$ detection, for many of the same reasons that it is an ideal isotope for neutrino mass measurements: it has a low endpoint energy, it has a moderate lifetime, and it has a simple nuclear structure. Added to this, it has a relatively high cross-section among the isotopes in Table 1.1, in combination with a lifetime long enough to ensure enough material to potentially observe this low-density population.

3.1 Expected Event Rates and Spectra

Using the cross-section and neutrino clustering described in Section 1.2 and the instantaneous amount of tritium ($40.7 \mu\text{g}$) in KATRIN's source, the Table 3.1 gives the expected event rates in KATRIN for various mass and neutrino distributions. A Fermi-Dirac distribution assumes no gravitational clustering—the relic neutrinos are spread uniformly through the universe. The Navarro, Frenk, & White distribution is characteristic of the gravitational clustering of dark matter. The Milky Way density profile is based on the mass profile of the baryonic matter of the Milky Way.

	Event Rates (events/yr)		
m_ν	Fermi-Dirac	Navarro, Frenk, & White	Milky Way
0.6	3×10^{-6}	3.6×10^{-5}	6.1×10^{-5}
0.3	3×10^{-6}	9.4×10^{-6}	1.3×10^{-5}
0.15	3×10^{-6}	4.1×10^{-6}	4.9×10^{-6}

Table 3.1: The event rates at KATRIN for three different neutrino masses and three different mass profiles for the $C\nu B$. Rates are calculated by scaling the results of Ref [17] by the tritium mass of the KATRIN experiment. All rates are given in events/yr.

3.2 Expected Sensitivity

It is clear from table 3.1 that KATRIN is unlikely to observe the $C\nu B$: it simply has far too little tritium. Nevertheless, calculating the projected limit for KATRIN provides a critical first step in understanding how to develop future $C\nu B$ experiments.

The signal for electrons from this nuclear capture is distinctive: a mono-energetic peak of electrons at one m_ν above the $m_\nu = 0$ beta-decay endpoint. This is a simple consequence of conservation of energy in the neutrino capture interaction and the fact that the neutrinos have a kinetic energy that is so far below any other characteristic energy scale in the system that their energy can be considered zero.

Because the KATRIN experiment measures the integral beta decay spectrum above some threshold qU set by the spectrometer, the electron spectrum is really the convolution of the β and $C\nu B$ electron spectrum, dN/dE , and the transmission function of the detector, $T(E, qU)$. KATRIN also expects a small but finite background rate, N_b , to contribute to the overall signal. Currently, this background rate is expected to be of order 10 mHz in the signal region of interest, independent of retarding voltage. These backgrounds come from tritium leaking into and decaying in the spectrometers, cosmic muon-produced electrons in the apparatus, and intrinsic background of the detector.

$$G(qU) = \int_{qU}^{\infty} \frac{dN}{dE} T(E, qU) dE + N_b \quad (3.1)$$

The tritium beta decay energy spectrum has an analytic form [64] given by Eq. 3.2

$$\frac{dN}{dE} = \sum_{fs} \left(N_{T_2} F(Z, E) p_e(E + m_e) (E_0 - E) \sqrt{(E_0 - E)^2 - m_\nu^2} \Theta(E_0 - E(fs) - m_\nu) + N_{C\nu B} e^{-\frac{(E_0 - E(fs) + m_\nu)^2}{2\sigma^2}} \right) P(fs)$$

where $F(Z, E)$ is the Fermi function for beta decay, E_0 is the endpoint energy of the ${}^3\text{H}_2 \rightarrow ({}^3\text{He}{}^3\text{H})^+ + e^- + \bar{\nu}_e$ decay, E is the kinetic energy of the emitted electron, and N_{T_2} and $N_{C\nu B}$ are the rates of tritium beta decay and neutrino capture, respectively. The gaussian term represents the capture signal from the $C\nu B$ centered at one neutrino mass above the endpoint, with a width σ which is smaller than any characteristic energy of the system. When simulating this, the width is chosen to be smaller than any characteristic resolution present in the experiment, but sufficiently large to be reliably integrable by numerical methods. Since the target involves the presence of molecular T_2 gas, one must include any corrections to the endpoint energy due to the molecular daughter molecule following the tritium decay. An accounting of these states is given in [65]. Of most relevance are the effects of the rotational-vibrational contributions from decays to the ground state, which introduce a mean excitation energy of 1.7 eV with an inherent broadening of 0.36 eV. In this analysis, the final states are taken into account via a summation over the states fs of the He^+T molecule, each final state weighted by the probability $P(fs)$ for that state occurring.

The transmission function, $T(E, qU)$, depends on the value of the retarding potential, qU , as well as the intrinsic resolution of the main spectrometer. For an isotropic source, $T(E, qU)$ can be written analytically as:

$$T(E, qU) = \begin{cases} 0 & \text{if } E - qU < 0 \\ \frac{1 - \sqrt{1 - \frac{(E - qU)B_S}{EB_A}}}{1 - \sqrt{1 - \frac{\Delta EB_S}{EB_{\max}}}} & \text{if } 0 \leq E - qU \leq \Delta E \\ 1 & \text{if } E - qU > \Delta E. \end{cases} \quad (3.2)$$

where E is the electron energy, B_S is the magnetic field at the source, B_A is the magnetic field at qU , B_{\max} is the maximum (pinch) field, and $\frac{\Delta E}{E} = \frac{1}{20000}$ at KATRIN.

A sample decay spectrum, with and without neutrino capture, is shown in Figure 3-1.

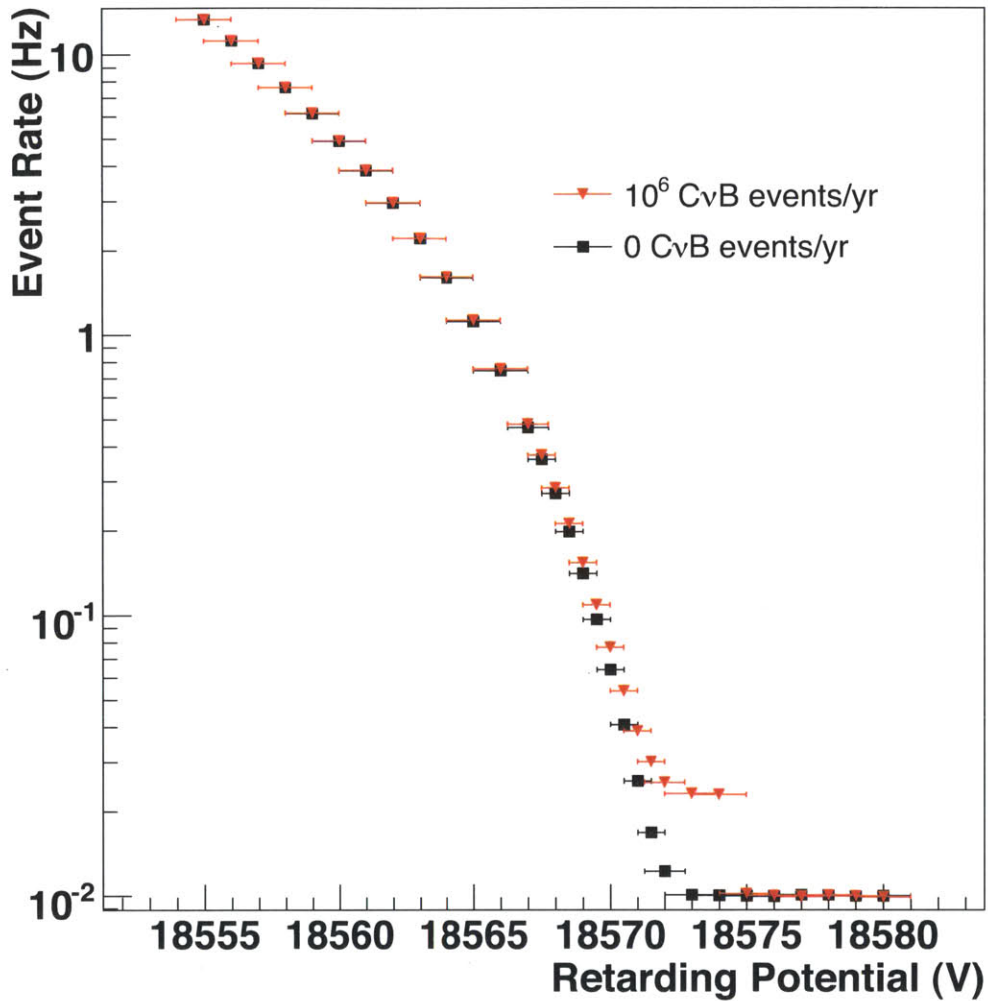


Figure 3-1: The anticipated beta decay spectrum as a function of retarding voltage with (black) and without (red) neutrino capture events. Neutrino mass is assumed to be 1 eV.

To calculate the sensitivity, many fake Monte Carlo data sets were created and fit over six parameters: the neutrino mass (m_ν), the CνB rate ($N_{C\nu B}$), the endpoint of the beta decay spectrum (E_0), the beta decay rate (N_{T_2}), the width of the CνB peak (σ), and the background rate (N_b). We assume the same projected KATRIN run measurement plan as reported in [61]. The results of the fit in the mass and capture rate are plotted for 2000 simulated experiments to create the confidence regions shown in Fig 3-2. The figure shows only statistical errors; the systematic errors are estimated

for four of the major errors for KATRIN: high voltage precisions, magnetic field precision, the effect of final states, and the error on the number of available tritium atoms. The errors are estimated by shifting the Monte Carlo data sets by one standard deviation on the error and fitting at the central value of that parameter. The relative contributions to the errors for the mass and $C\nu B$ rate are shown in Table 3.2. The 90% limit is shown for a variety of masses in Fig 3-3. Shown on the right hand side of the plot is the limit on the local density of neutrinos at Earth. There is a slight decrease in sensitivity near 2 eV due in part because the run plan for KATRIN is discretized and optimized for a neutrino mass search. The discretization in the retarding potential in 0.5 V steps in the region of interest means that the $C\nu B$ search is restricted to a few points which do not change significantly with increasing mass up to about 1eV. However, above 1 eV, the finite endpoint of the default run plan means there are not sufficient bins to firmly establish the background level. Widening the energy scan from the original plan improves the limit significantly.

Contributor	Error (events/year)	Percentage of Statistical
High Voltage	± 5850	70.1%
Magnetic Field	± 2020	24.2%
Final States	± 1420	17.0%
Normalization	± 2080	24.9%
Statistical	± 8340	–
Total	± 10680	128%

Table 3.2: Error contributions to the $C\nu B$ for four major KATRIN systematics at $m_\nu = 0$ eV. Errors are extended to other masses as a percentage of statistical errors. Note that the error on the final states is limited by Monte Carlo statistics.

3.3 Implications

From a limit on the local density at earth, certain theoretical possibilities can be investigated. It has been proposed that the knee of the cosmic ray spectrum could be caused by a relic neutrino GZK effect [66], which requires a neutrino overdensity of greater than 10^{13} . Since the required overdensity to result in the limit KATRIN can set is 2.0×10^9 , then, assuming KATRIN sees no signal at the expected sensitivity,

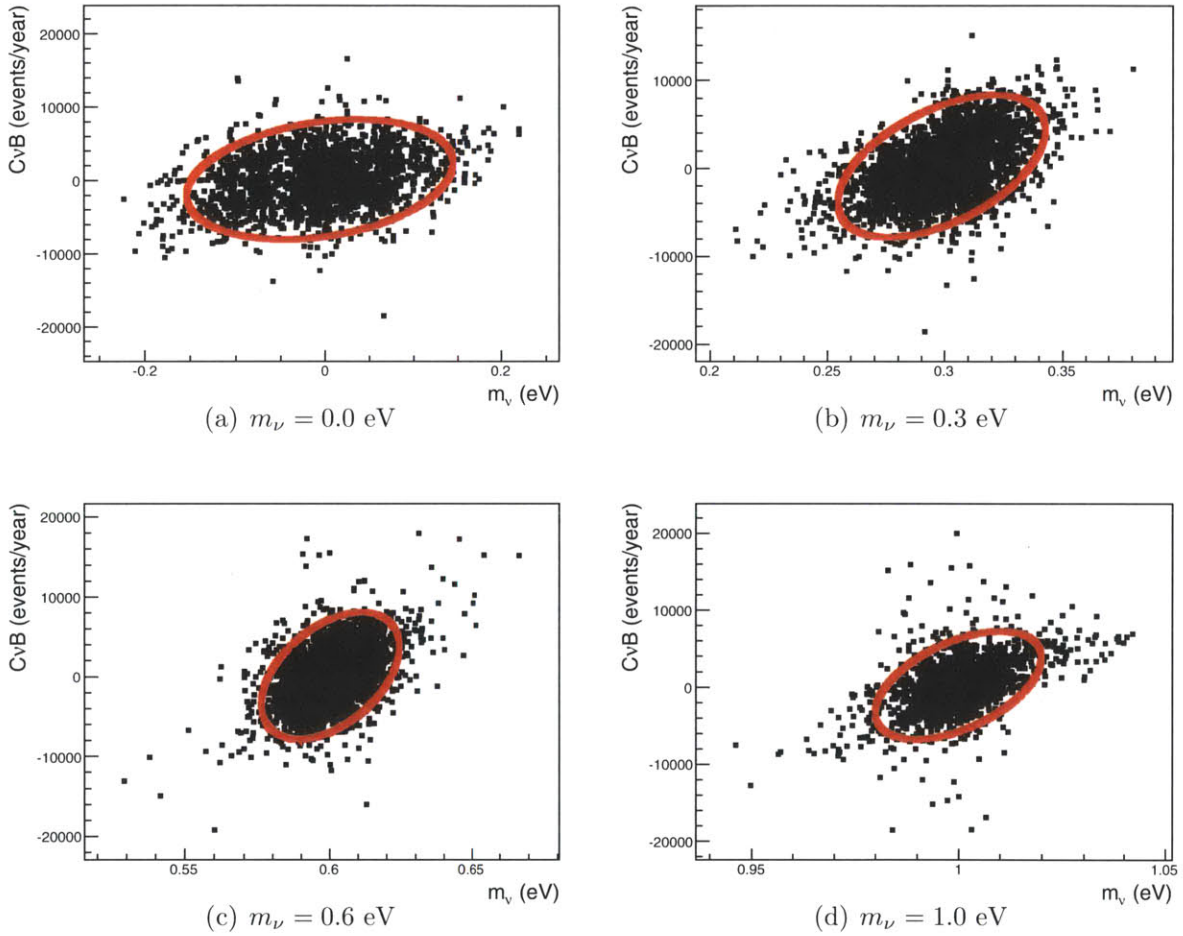


Figure 3-2: Confidence regions for cosmic neutrino captures in events per year versus neutrino mass in eV for four example neutrino masses. Statistical errors only are shown. Red ellipse shows 90% C.L in the $C\nu B$ events per year and neutrino mass parameter space.

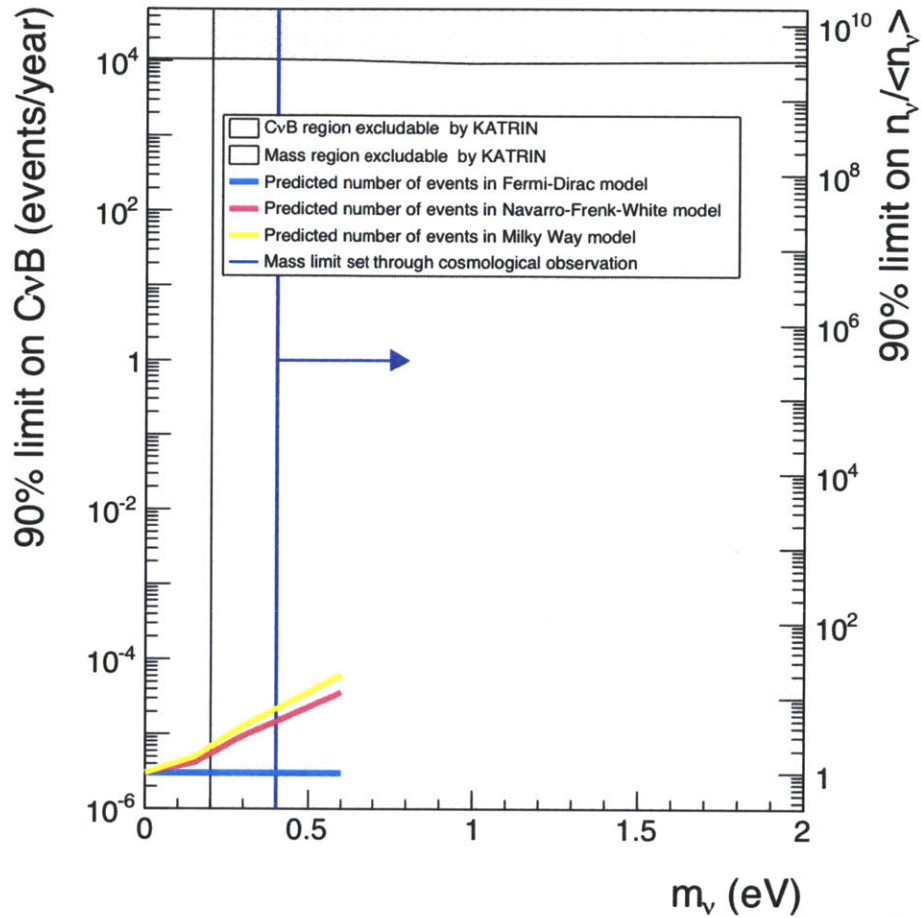


Figure 3-3: The 90% confidence level sensitivity limit for relic neutrino over-density as a function of neutrino mass as expected from the 3 year data run at the KATRIN neutrino mass experiment. Solid curves show expectation from cosmological prediction assuming Fermi-Dirac (light blue), Navarro-Frenk-White (violet), and Milky Way (yellow) mass distribution. Arrow shows neutrino mass limits already obtained from cosmological observations ($\sum m_\nu \leq 1.2$ eV) [11].

KATRIN will exclude this model for neutrinos near earth. It has also been proposed that neutrinos could couple to one another via a light scalar boson and form bound clouds with significant effect on small scale structure formation in the universe [67]. While this work shows that KATRIN is able to set a better limit on overdensity than the experiments considered therein by a factor of 10^6 (resulting in an improvement on the limit on the fermi momentum by a factor of 100), the ultimate limit on the coupling strength is also determined by the neutrino mass. In the range of masses accessible at KATRIN, the limit on the coupling strength could either entirely rule out this model or broaden the parameter space significantly. While no firm conclusions can be drawn with this work, it is definitely a topic for future analysis.

Chapter 4

The DMTPC Experiment

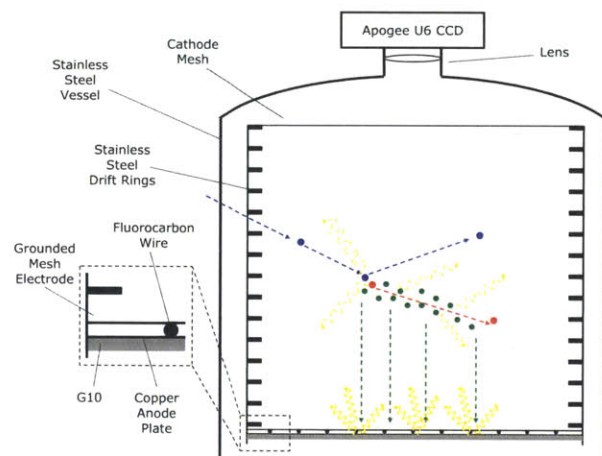
The DMTPC “10L” detector is a first-generation prototype of the DMTPC experiment[68]. It is a dual-sided drift chamber with two forms of readout: charge-coupled device (CCD) cameras and an electronic readout of the amplification region. The configuration and calibration of this detector will be described in this chapter.

4.1 Detector Configuration

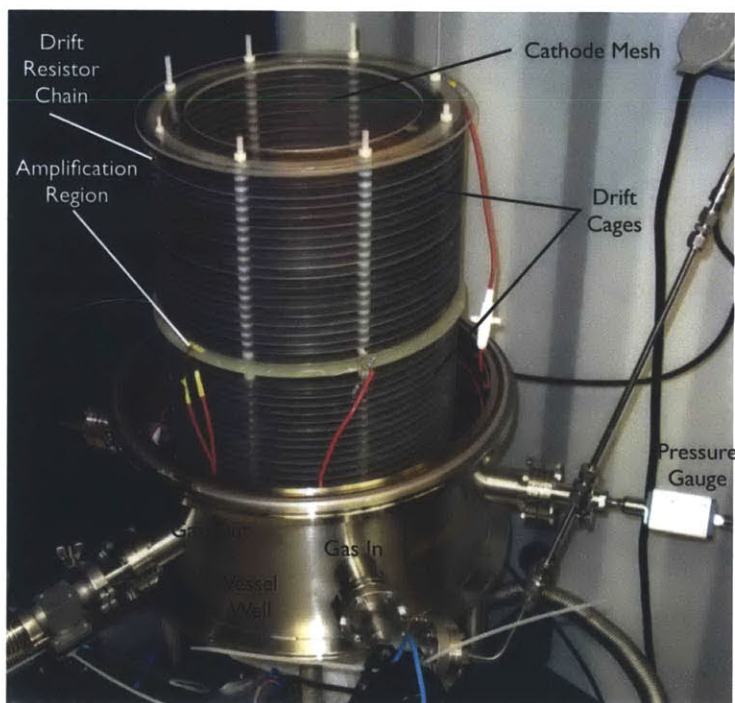
A schematic and photograph of the DMTPC 10L detector is shown in Fig. 4.1.

4.1.1 Outer Vessel and Gas System

The active volume of the detector is located inside a 16” outer diameter and 25” tall cylindrical vacuum vessel with 0.188” thick walls. The vessel consists of a “well” approximately one third the total height and a “bell” which sits on top of the well, with an o-ring in between. There are six ports on the well for services to the inside. There are three ports for the gas system: gas in, gas out, and a pressure monitor; and three ports for electrical connections: two high voltage ports and one for charge signal out. Both the well and the bell have a circular port on the ends of the cylinder with a quartz window for CCD readout. All ports use ConFlat copper o-rings at the nearest connection to the vessel, though many connections also have quick flange



(a) Schematic showing the main components of the DMTPC 10L detector. The diagram shows only one of the two drift chambers. A WIMP (blue) is shown interacting with a F atom (red) resulting in ionization (green) and scintillation (yellow).



(b) Photograph showing the drift cages, amplification region, and bottom section of the DMTPC 10L detector. The detector is in its underground laboratory at the WIPP facility near Carlsbad, NM.

Figure 4-1: A schematic and a photograph of the DMTPC 10L detector

connections.

The gas system consists of a series of computer controlled valves connected to the input gas bottle, which allow the detector to be filled to a given pressure of gas, and a rough pump and a turbo pump for evacuating the vessel. The turbo pump is not normally used during dark matter search running, but is used after the interior of the detector has been exposed to ambient air. Using the turbo, the vessel can be evacuated to 5×10^{-4} torr. The pressure is read out using an Inficon PCG400 pressure monitor, which provides gas-independent pressure monitoring over the range of 5×10^{-4} mbar to 1.5 bar.

4.1.2 Field Cage

The main active volume of detection is contained within drift cages 19.7cm tall. The drift cages are composed of 19 steel rings 27 cm in inner diameter and spaced 1 cm apart. The rings are supported by six acrylic rods which run vertically through each ring and also align the acrylic spacers which maintain the inter-ring spacing. Each drift ring is connected by a 1 M Ω resistor to its immediate neighbors. At a cathode mesh stretched over the ring furthest from the amplification region, -5 kV is applied, and the bottom ring is connected through an 2.2 M Ω resistor to ground. This provides a 25.4 kV/m electric field over the drift region with transverse field component of less than 1%. Figs. 4-2 and 4-3 show a finite element method analysis of the electric fields in the drift cage, showing its uniformity.

4.1.3 Amplification Region

The amplification region is comprised of a grounded stainless steel mesh, stretched over a stainless steel ring of inner diameter 27 cm and circle of copper—the anode—fixed on a layer of G10. The two are separated by sections of plastic wire of diameter 0.53 mm, spaced approximately 2.5 cm apart. The mesh sits 1.7 cm from the bottom ring of the drift cage. Since the detector contains two back-to-back active regions, the G10 is shared between the two regions, with copper on both sides of the plane.

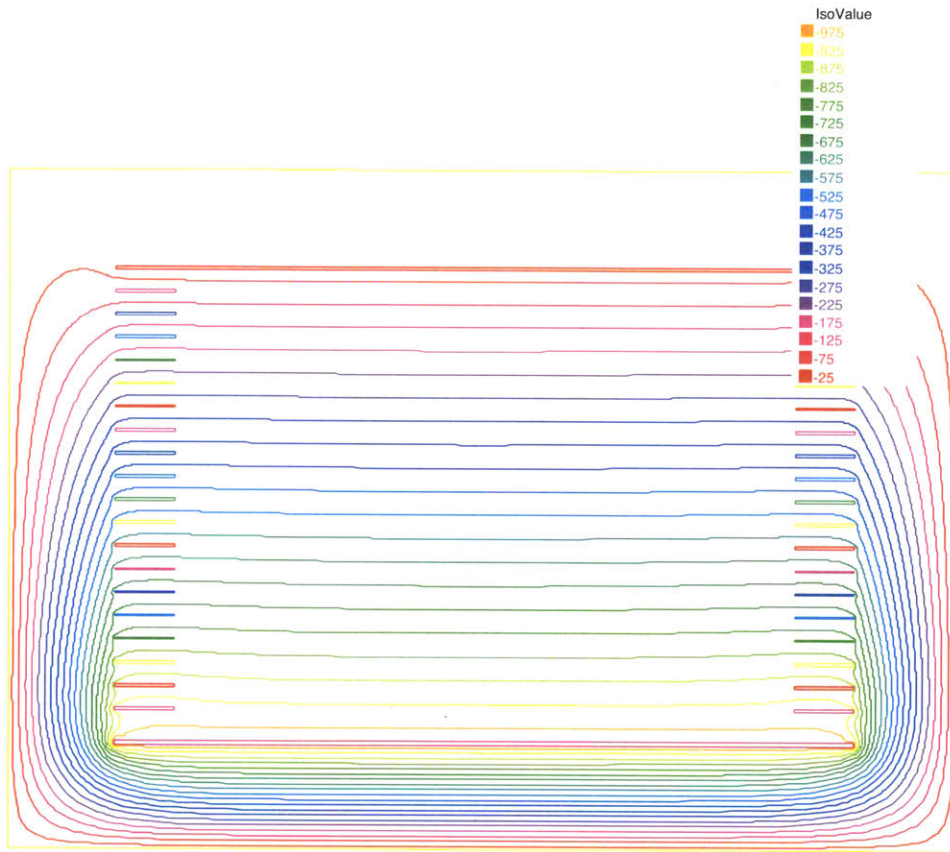


Figure 4-2: A finite element method analysis of the electric potential contours of the 10L drift cage for 1000 V applied. Numbers are in units of volts. The horizontality and uniform spacing of the contours indicates that the electric field points vertically downwards and is uniform along the drift cage.

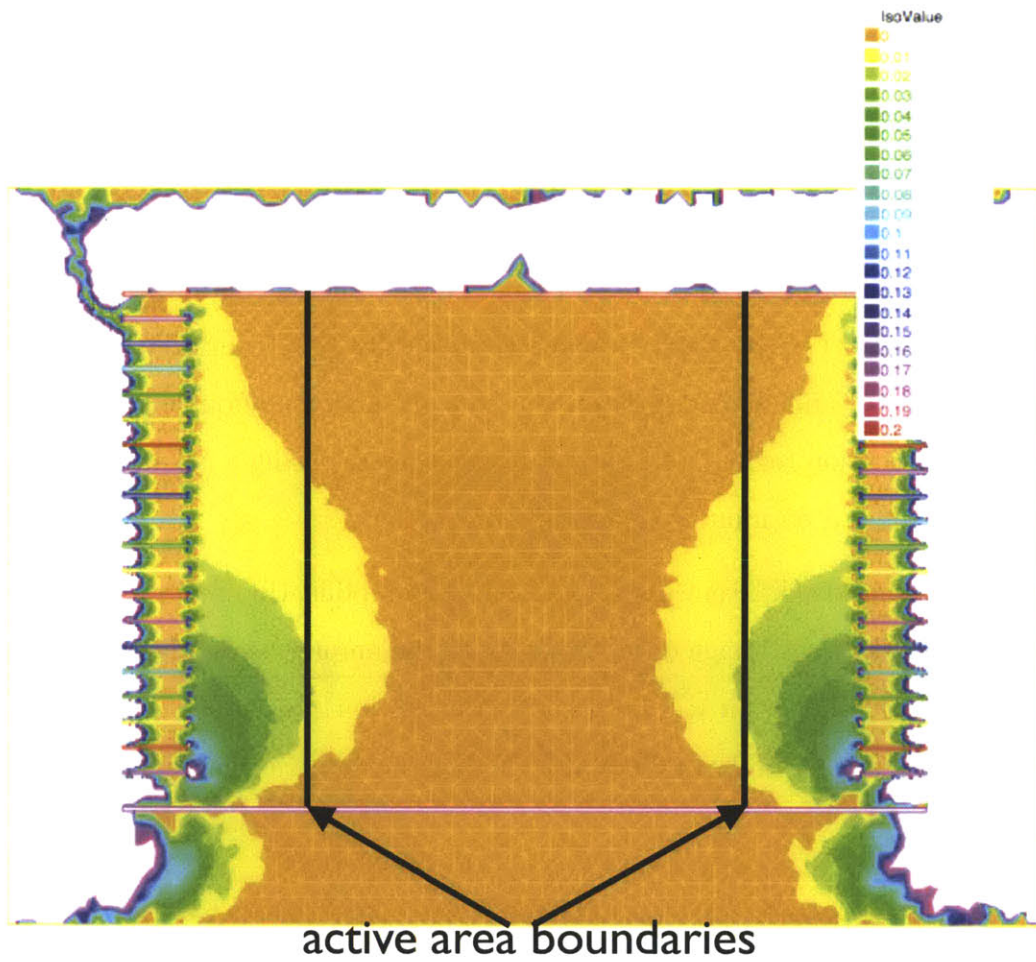


Figure 4-3: A finite element method analysis of the transverse field in the 10L drift cage. The colors indicate the value of E_T/E . The active area has no more than 1% transverse field.

At normal operating voltage of 700 V, the electric field in the amplification region is 1.32×10^6 V/m. At 60 torr and 300 K, the first Townsend coefficient for CF_4 is 21630 m^{-1} , so the amplification over the 0.53 mm of the amplification region is approximately 10^6 .

4.1.4 CCD Readout

The primary readout for the detector is through one CCD camera for each active region. Each camera is an Apogee Alta U6. These cameras contain a Kodak1001E chip with 1024×1024 pixels, each of which is physically $24 \times 24 \mu\text{m}$. The cameras are operated at -20°C and binned 4×4 on the chip to reduce readout noise. The light from the amplification region is focused onto the cameras using a Nikon photography lens with $f/1.2$ and a 55 mm focal length.

Because of slightly different distances from the amplification region, due to space constraints, the cameras image different areas on the amplification plane. The procedure for distance calibration will be described in section 4.3.3, but the result is that the top camera images $14.0 \times 14.0 \text{ cm}$ and the bottom camera images $17.2 \times 17.2 \text{ cm}$.

4.1.5 Charge Readout

Each amplification region has two charge readout channels. One is attached to the copper anode and is readout through a Cremat 113 amplifier, with a slow ($1 \mu\text{s}$) rise time. The other is attached to the grounded mesh and is readout through a custom fast amplifier with a fast rise time (40 ns). All four channels are read out through and Alazar ATS 860 digitizer. The calibration and characterization of this system is still ongoing, and so the data from this system are not used in the analysis in this work.

4.2 Gas Properties of CF₄

For spin-dependent dark matter searches, CF₄ is considered good option because it has a high spin enhancement $\lambda^2 J(J+1)$, as described in section 1.3.4. Additionally, because there are commercial uses for CF₄, it is easily available at high purities, and many of its gas properties are well-known [69]. Beyond its theoretical suitability, however, there are a few practical measurements that must be made to determine its suitability for use in a drift chamber.

4.2.1 Drift Electron Diffusion and Attachment

The diffusion of drift electrons is of intense concern to an experiment such as DMTPC. If the diffusion is too great, it will overwhelm the directionality of any signal. Therefore, the diffusion in CF₄ was measured using the detector and reported by the collaboration in Reference [70]. This was done by placing alphas sources at varying heights in the drift cage and measuring the width of the resulting tracks in the detector. The pressure and drift voltage of the detector was varied in order to measure the diffusion over a range of E/N, the field-to-density ratio. The results are parameterized by the quantity D/μ , where D is the diffusion constant and μ is the mobility of the electrons, an inherent property of the gas. The spread of a track varies linearly with the distance z that the track drifts in an electric field E :

$$\sigma^2 = \sigma_0^2 + 2 \left(\frac{D}{\mu} \right) \left(\frac{z}{E} \right) \quad (4.1)$$

The results are shown in Fig. 4-4. The errors are dominated by the uncertainty in the collimation of the alpha sources used for the measurement and the uncertainties in the relative gains at the locations of the different alphas. At normal operating conditions of 60 torr and 300K, the reduced field is 13.1×10^{-17} V·cm², and the maximum transverse diffusion over the maximum drift of 20 cm is about 1mm.

Additionally, if there is any attachment of electrons during drift, the signal could be attenuated over the drift, resulting in a z-dependent energy calibration. However, in this detector, no attachment was measured in the relevant parameter space.

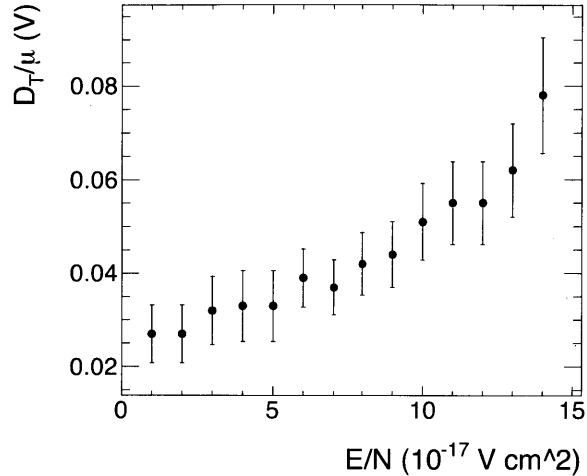


Figure 4-4: The transverse diffusion of CF_4 as a function of reduced field.

4.2.2 Scintillation Spectrum

The other requirement for an experiment with optical readout, such as DMTPC, is that the wavelengths of the output scintillation of the gas must be well-matched to the sensitive wavelengths of the detection device: the CCD camera. The output of CF_4 scintillation in electron avalanches was measured using a Jobin-Yvon 1250M spectrometer using an ultraviolet-sensitive Hamamatsu R928 multialkali PMT and a proportional tube, as described in Reference [71]. The spectrum is shown in Fig. 4-5.

In this spectrum, $58 \pm 6\%$ of the light is above 450nm. This is well-matched to the U6 cameras, whose quantum efficiency as a function of wavelength is shown in Fig. 4-6. The peak of the efficiency is at about 620 nm, which is remarkably similar to the peak in the CF_4 spectrum.

4.3 Calibration

Since the camera returns an image in spatial units of the pixels of the camera and arbitrary digitized units (ADU), and the charge readout returns a trace in voltage units, the camera and the charge readout must be calibrated to understand the output of the detector in useful units of keV and mm. Additionally, the overall spatial gain variation of amplification region of the two drift chambers must be understood. For

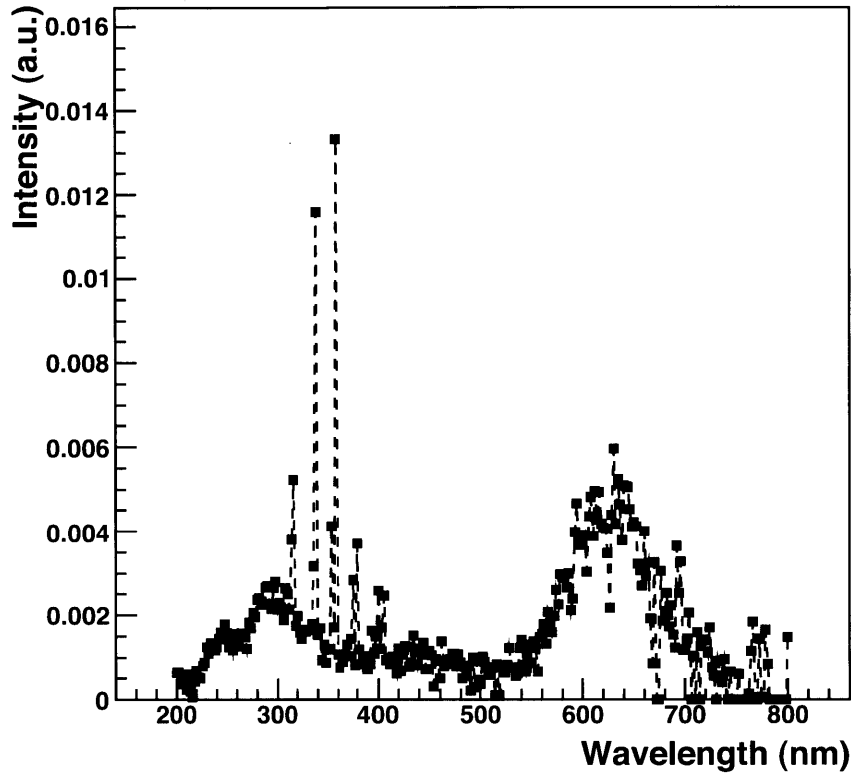


Figure 4-5: The measured scintillation spectrum of CF_4 as a function of wavelength. The integral of the spectrum is set to unity. Error bars are not shown for clarity. $58 \pm 6\%$ of the spectrum lies between 450 and 800 nm.

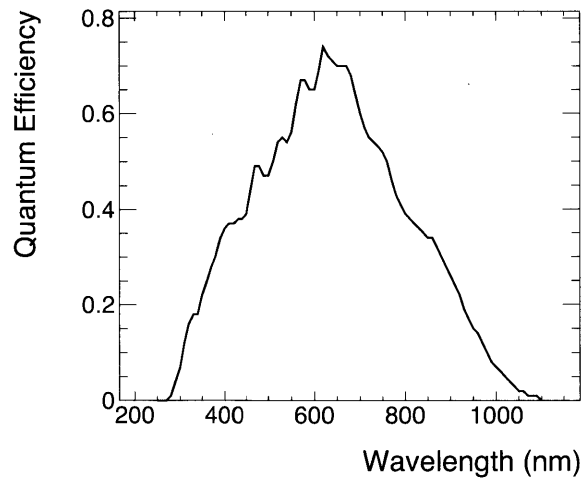


Figure 4-6: The wavelength-dependent quantum efficiency for the Kodak1001E chip of the Apogee Alta U6 cameras. The peak of this spectrum is well-matched to the 630 nm peak in the scintillation spectrum of CF_4 .

this purpose, a calibration regime was carried out periodically with the detector.

4.3.1 Energy Calibration

To calibrate the energy, an ^{241}Am alpha source with an energy of 4.5 MeV^1 was placed between the two rings closest to the amplification region on both sides of the detector. This alpha source was placed parallel to the spacers, and between them, so as not to lose any energy due to the spacers. Data were taken at the normal operating point of the detector, using 1 s exposures.

The candidate alphas tracks are carefully selected so that they match with the known location of the alpha source, are strictly straight, contain no kinks due to hard scatters, and contain only one alpha. The last condition is necessary, because, as the decay is a random process, there is non-zero probability that two decays will sit on top of one another during the 1 s exposure. This is accomplished by examining the distribution of energies in the track over the calibration period; discrete peaks occur in this distribution, and only candidates consistent with the lowest peak are passed.

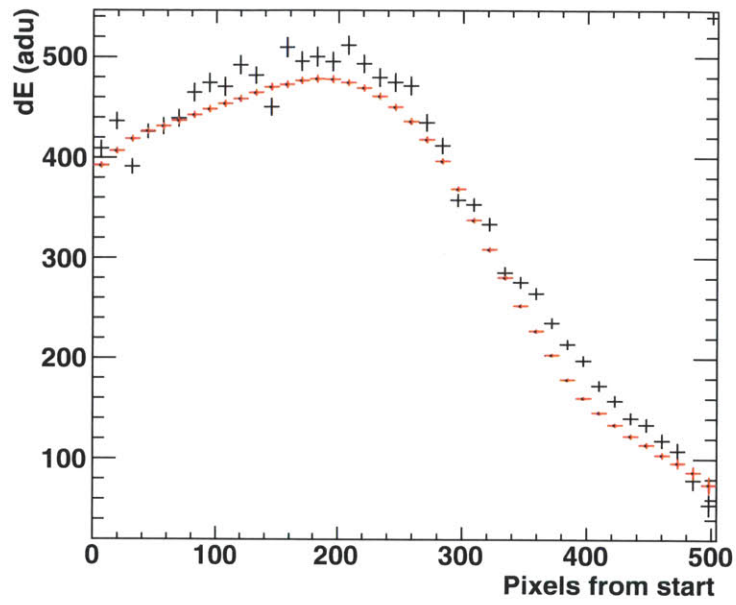
The alphas that meet these requirements are then projected onto an axis parallel to their direction, and their gain map corrected energy (see section 4.3.3) is plotted as a function of distance from the source. Using a theoretical $\frac{dE}{dx}$ distribution for the gas properties, as calculated with the SRIM program [72], and a Monte Carlo simulation of the energy deposition from alphas, the actual alpha tracks are compared with tracks of the known energy of the sources.

The results of this calibration are shown in Fig. 4-7. In the top drift chamber the calibration is 18.6 keV/adu , and in the bottom chamber, 17.5 keV/adu .

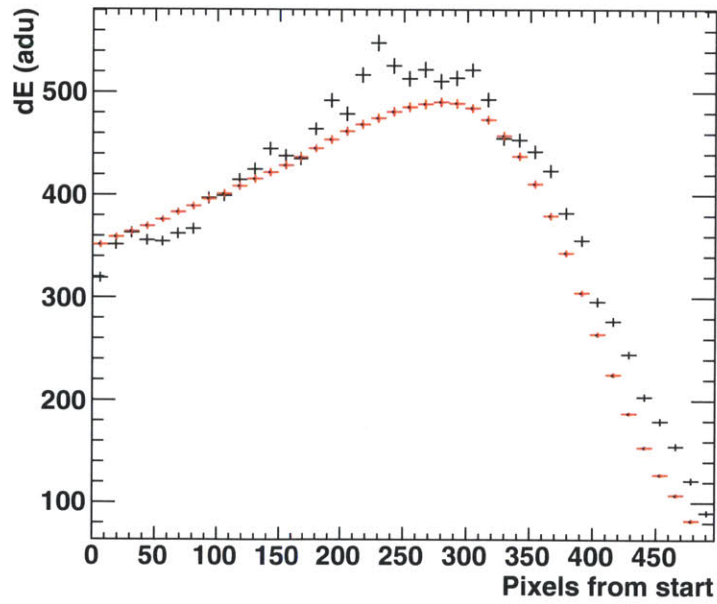
4.3.2 Energy Stability

It is also important to know the stability of the energy calibration. The detector has its gas refilled approximately once a day, and so the gain stability within a particular fill and between fills must be determined. To study the intrafill variation, the energy

¹Each alpha source was individually calibrated using a surface barrier detector to the 5% level



(a)



(b)

Figure 4-7: The energy calibration for (a) the top chamber and (b) the bottom chamber. Black points show data from alpha tracks in the chamber and red shows Monte Carlo generated tracks using the calibration constants 18.6 keV/adu (top) and 17.5 keV/adu (bottom) which provide the best match to the data.

calibration value is plotted per 1000 event run within the fill period. A plot of that for 3 fills is shown in Fig. 4-8. Only the variation for the top chamber is shown, for clarity, but the bottom calibration varies the same way. The typical variation is 3% over the course of the fill. The interfill variation over 850 hours (about one month) is shown in Fig. 4-9; this shows that the gain tends to decrease over time. This variation is about 7%.

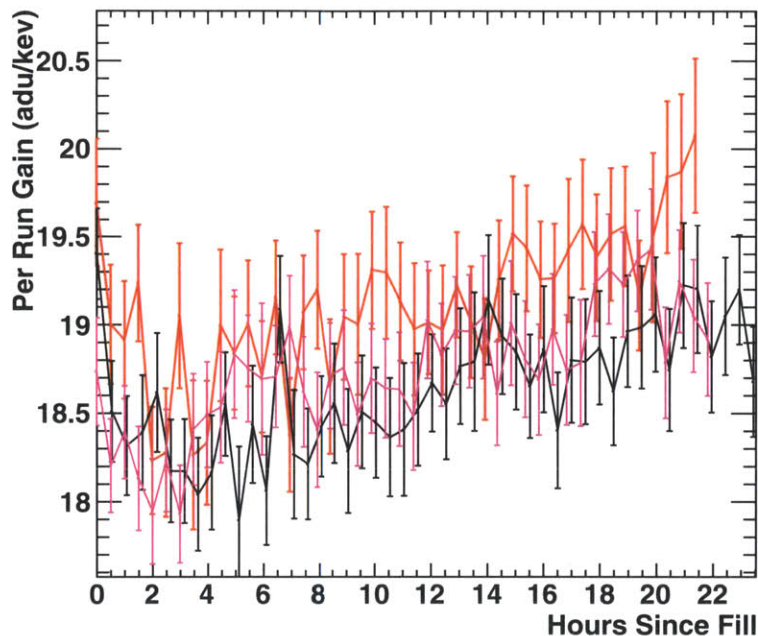


Figure 4-8: The variation of the energy calibration within a gas fill for three different fills. The gain rises about 3% over the course of a fill, and the interfill variation is 7%

These two variations dominate the uncertainty in the energy calibration.

4.3.3 Relative Gain Calibration

The gain variations of the amplification region must also be measured to calibrate the gain properly. The gain variations are measured by flooding the detector with gammas, which produce electron cascades uniformly over the active region. By integrating over many exposures, the gain variations become evident. These gain variations represent a convolution of many effects: the gain variation due to amplification region

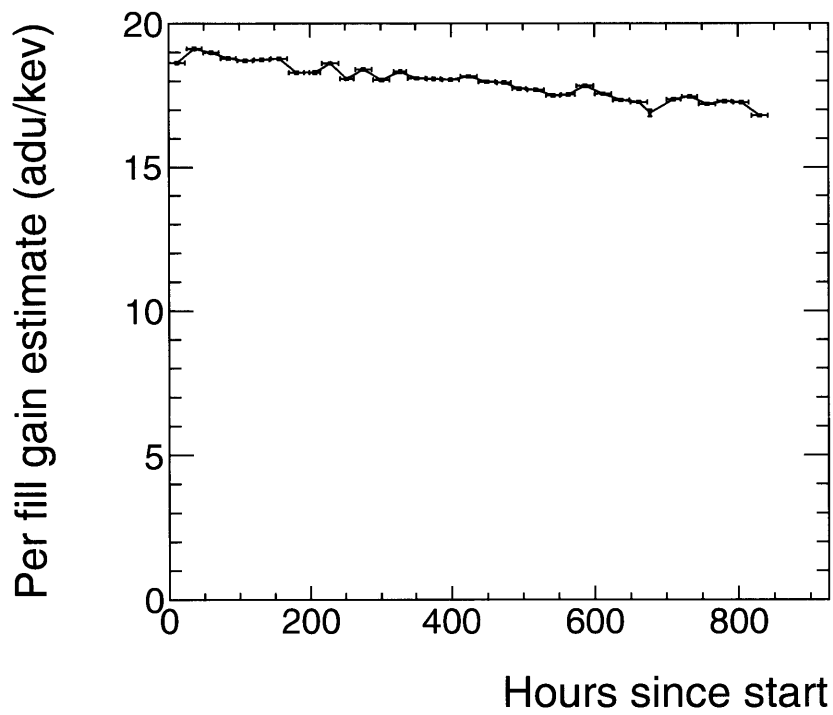


Figure 4-9: The variation of the energy calibration across many gas fills (one point per fill) for 850 hours. There is a downward trend with a variation of about 7%.

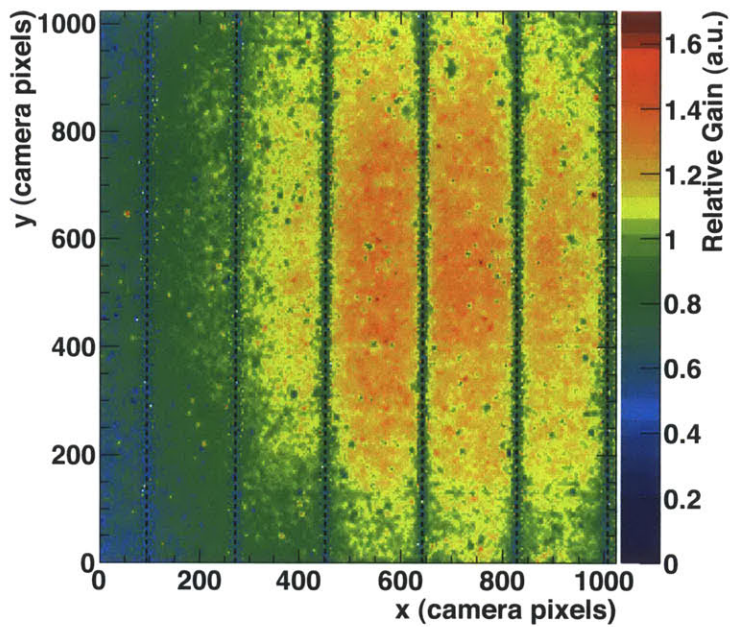
construction, radial loss of light due to the lens, and any camera positional effect.

The gammas are produced using two sources concurrently: a ^{137}Cs source, which produces a gamma of 662 keV in its decay to ^{137m}Ba ; and a ^{57}Co source, which produces 122 and 136 keV gammas in its decay to ^{57}Fe [73]. The sources are placed exterior to the detector in contact with the window of the opposite-side region—e.g., to calibrate the bottom drift chamber, the sources are placed on the window to the top drift chamber. The detector is run at a higher pressure than normal operating conditions, 75 torr, in order to increase the number of available targets. Additionally, the cameras are exposed for 5 s, to decrease the relative noise. Each side of the detector is exposed for approximately 60,000 s during a given calibration.

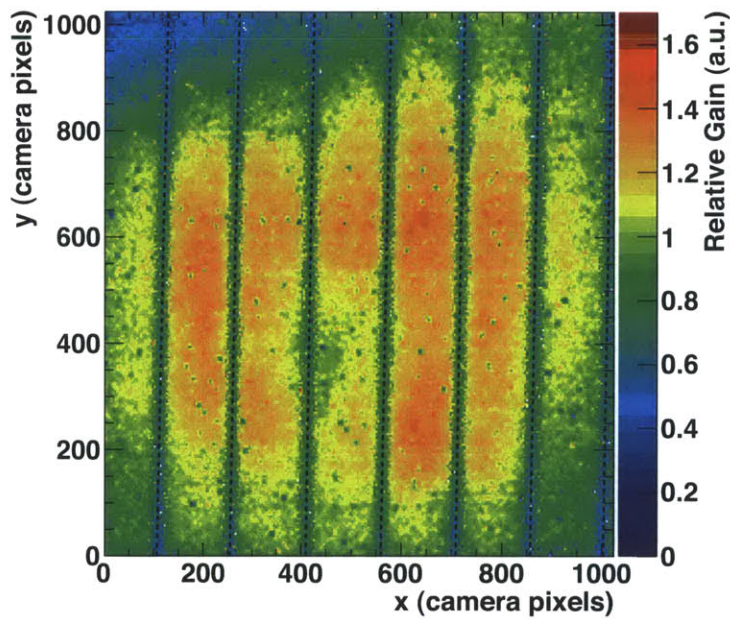
The frames are processed by creating a running sum over all of the images, excluding any images that show anode discharges (“sparks”), and within any image, any set of pixels sufficiently high enough above background to be considered a particle track in the reconstruction. Each pixel is then divided by the number times it has been entered into the sum. The image is blurred using a gaussian kernel to further reduce noise, and then normalized such that the average value of each pixel is 1.

The results of this process are shown in Fig. 4.3.3. Note that there are significant non-uniformities. The top drift chamber has a region of low gain along the left side of the image. The bottom drift chamber has a curious horseshoe shape in the middle of the image, along with a region of very low gain in the upper left hand corner. As a result, the relative gain varies by a factor of about 50% over the active areas, making this calibration very important indeed.

An additional feature of this procedure is the ability to calibrate the spatial dimension of the detector. In each gain map, regions of low gain are visible in vertical lines, corresponding to the locations of the spacers separating the sides of the amplification region. Since the true separation of the spacers is known, the conversion factor can be calculated. To do this, the image is divided into four horizontal slices. In each slice, a fit is performed to find the position and width of each spacer in the image. The four positions for each spacer are then fit with a line. This line represents the spacer position, and is saved along with the gain map for future use. The distance



(a) Top camera, serial number 081264.



(b) Bottom camera, serial number 100439.

Figure 4-10: Relative gain maps for the DMTPC 10L detector, produced using a Cs-137 and a Co-57 source. Spacers are marked with dotted lines. The maps are normalized such that the average value of a pixel in the image is 1.

between lines then allows for the calculation of the spatial calibration. In the top drift chamber, the calibration factor is 0.137 mm/pixel, and in the bottom drift chamber, 0.168 mm/pixel.

Chapter 5

Underground Operation of DMTPC

In 2010, the DMTPC 10L detector was moved underground to the Waste Isolation Pilot Plant (WIPP) near Carlsbad, NM, and in 2011, the detector was run in a source-free mode for a dark matter search.

5.1 The WIPP Facility

The WIPP facility is a United States Department of Energy facility designed for storage of defense nuclear waste. It is dug into the Permian salt bed, 2150 ft below surface level. The rock surrounding the underground laboratory is primarily NaCl, with small deposits of other salts and clays. The overburden is flat with an average density of 2.3 g/cm^3 and is 1585 meters water equivalent. It has a underground muon flux of $4.77 \times 10^{-7} \text{ cm}^{-1} \text{ s}^{-1}$, and a total modeled muon induced neutron flux of $3.41 \times 10^{-8} \text{ cm}^{-2} \text{ s}^{-1}$. [19] The radon background underground at WIPP has been measured to be 0.2-0.3 pCi/L [74], which is about a factor of 3-4 lower than the 0.8 pCi/L measured in the surface lab. The detector is at a distance of approximately 1 km from the stored waste. A photograph of the lab is shown in Fig. 5-1 and the installed detector in Fig. 5-2.



Figure 5-1: A photograph of the lab where the DMTPC 10L is located in the WIPP facility. The detector is in the far right corner of the lab as shown in this picture.



Figure 5-2: A photograph of the 10L detector installed in DMTPC lab at the WIPP facility.

5.2 Data Taking

For the course of this run, the detector was operated at 60 torr of CF_4 , with an amplification region voltage difference of 700 V, and a drift field voltage of -5 kV.

Data is taken ‘observer’ mode, where the camera are exposed for 1 second, read out, and exposed again. This mode introduces 0.3 seconds of dead time per exposure, for camera readout. The cameras are operated in 1000-exposure runs. Each run contains a dark frame, taken from 100 exposures taken while the camera shutters are closed. This is used to subtract the inherent variations in readout over the camera chips.

Once every 24 hours, the detector gas is refilled, in order to maintain gain stability. (See Section 4.3.2.) During this time, the voltage is off, and the cameras operate in the same way as voltage-on data taking. This allows for separation of backgrounds that come from camera effects, as will be discussed in section 5.4.

5.3 Data Processing

Data processing for CCD images involves several steps. First, the images must be pedestal subtracted and cleaned of hot pixels. Then, tracks in the image can be found, and their relevant parameters—e.g, energy, length, and position—calculated.

5.3.1 Image Cleaning

At the beginning of each run, a bias frame for each camera is saved. This frame is comprised of the average of 100 images taken at the same exposure as the data, but with the shutter closed. This allows intrinsic variations over the chip to be subtracted off. For example, the Alta U6 cameras used on this detector typically have a higher pedestal along the left side of the image, and a lower pedestal along the bottom of the image. This bias frame is processed before using it to remove pixels which are 5 sigma outliers from the mean of the image.

After checking each image for sparks—see subsection 5.4.1—each data image also

has hot pixels removed, though in this case, a test is made to see if nearby pixels are also above average, as above average pixels in a track should not be removed. Then the bias frame is subtracted from the image. Finally, as the average value of the images varies over the course of a run, a final correction is made to bring the mean of the data image to zero. This is done by comparing the average pixel value of the overscan part of the image with the average pixel value of the bias overscan image, and using that difference to correct the main image.

5.3.2 Track Finding

After cleaning the image, interesting features of the image must be recognized and cataloged. The first step is to create a blurred copy of the cleaned image, using a gaussian blurring algorithm. This reduces the effect of pixel-to-pixel noise and makes features more prominent. After the blurring, the bin with the maximum value in the blurred image is found. If this bin is 5.2 sigma above the image mean, then a track begins. Working out in rings from this pixel, pixels are added if they are above threshold in both the blurred and unblurred images with a decreasing threshold for each ring, until no more contiguous pixels are above threshold. If the total number of pixels in the track is greater than 5, the track is kept. Then, if there are any pixels not in the track that four or more of the track pixels touch, then it is added to the cluster. This promotes a concave track shape. All pixels in the track are marked as used and unavailable for any other tracks in the image. A 'reduced' cluster is also formed requiring a higher threshold, and thus consisting of the brightest pixels in the track.

This process repeats until there are no other features found. Then tracks must be merged across the spacers. Two tracks are considered for merging if they are closer than a certain distance or if both tracks have a close approach to the same spacer. If there is a reason to consider a merge, a line is fit to both candidate tracks. If both tracks have 'good' line fits ($|r| > 0.65$, where r is the linear fit correlation coefficient), then the lines are checked to make sure that they have similar slopes and that each line closely approaches the centroid of the other candidate track. If so, the tracks are

merged. If one track has a good line fit and the other track does not, the line from the track with a good fit is extended towards the other track. If the line is close to the centroid of the other track, the tracks are merged. Finally, if both tracks lack good line fits, a combined line fit is made with the two candidate tracks. If this fit is good ($(|r| > 0.8)$), the tracks are merged. This process is repeated until there are no mergers in the image.

5.3.3 Parameter Calculation

After the clusters of the pixel are determined, the parameters of the track are determined by algorithms on the pixels of the cluster. Some of the parameters are 'physical' parameters (e.g. energy or range) and some of them are 'selection' parameters that assist in background removal (e.g. maximum pixel). A list of relevant parameters calculated and the method used to calculate them is given below.

Energy The energy is calculated by dividing the number of ADU in each pixel by the normalized gain map, in order to correct for the variations in gain. Then, the total number of ADU in all the pixels of the track are summed. This, multiplied by the gain constant for a given camera, is the visible energy.

Recoil Energy The recoil energy is found from the visible energy by using an equation fit from the Monte Carlo, which calculates the visible energy using the Hitachi model [75].

Range An initial estimate of the range is found by finding the two pixels in the reduced cluster that are farthest apart and calculating the distance between them. This estimate must be altered at low energy because of the finite size of the pixels, which means that the relative placement of the track with respect to the pixel strongly affects the range reconstruction. This typically gives rise to overshoot for tracks under 8 pixel units in length. The correction is made by fitting a function to Monte Carlo data, as described in section 5.3.4. Measured range in all cases is the 2D range of the recoil projected onto the anode.

Position The position of each track is calculated as the ADU-weighted position of each pixel in the track.

Phi The angle of the track in the readout plane is calculated by finding the ADU-weighted variance in both of the camera axes (σ_{xx} and σ_{yy}), and the covariance between them (σ_{xy}). From these the eigenvectors of the matrix

$$\begin{pmatrix} \sigma_{yy} & \sigma_{xy} \\ \sigma_{xy} & \sigma_{xx} \end{pmatrix} \quad (5.1)$$

can be found, and two corresponding angles, representing the rotation of the coordinate system to that eigenvector. The angle of the track is the one of those two angles that maximizes $\sigma_{xx} \cos^2 \phi + \sigma_{yy} \sin^2 \phi + \sigma_{xy} \sin 2\phi$. This procedure is equivalent to finding the best fit ellipse that describes the track. The procedure gives the ‘axial’ angle of the track; that is, an angle which is between $-\frac{\pi}{2}$ and $\frac{\pi}{2}$. To find the vector angle, the direction of the track must be determined. To do this, the track is projected along the axis of the angle found in the previous part. The midpoint of this projected track is found, and the amount of deposited energy on either side of the midpoint is calculated. Since a particle deposits more energy at the beginning of the track than the end of the track, the side of the track with more deposited energy is determined to be the ‘head’ of the track.

Longitudinal Moments The second, third, and fourth longitudinal moments are calculated by projecting the track along the ϕ direction of the track, and using the ADU weighted bins along that axis to calculate the moments.

Transverse Moments The second, third, and fourth transverse moments are calculated by projecting the track along the direction perpendicular to the ϕ of the track, and using the ADU-weighted bins along that axis to calculate the moments.

Maximum Pixel The maximum pixel is simply the number of ADU in the pixel

with the greatest number of ADU. This quantity is useful in removing background—very high values indicate non-nuclear recoil tracks. See section 5.4.3.

Cluster Mean and RMS The cluster mean and rms are the mean and rms of the ADU levels of the pixels in the cluster.

Neighbors The number of neighbors above a threshold around the maximum pixel of a track. This quantity is useful in removing background—few neighbors indicate a non-nuclear recoil track. See section 5.4.3.

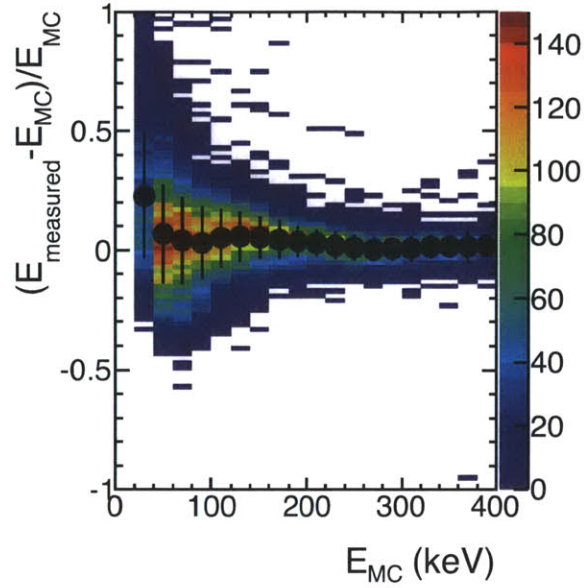
5.3.4 Monte Carlo Simulation and Parameter Reconstruction Quality

A simple Monte Carlo simulation is used to verify the track finding and reconstructed parameters. This simulation uses a foundation of SRIM and GARFIELD to model recoiling particles, a gaussian model of diffusion to model the track size, and blank CCD images to model the camera noise. It incorporates the true gain maps of the detector for spacer placement and gain variations across the field of view.

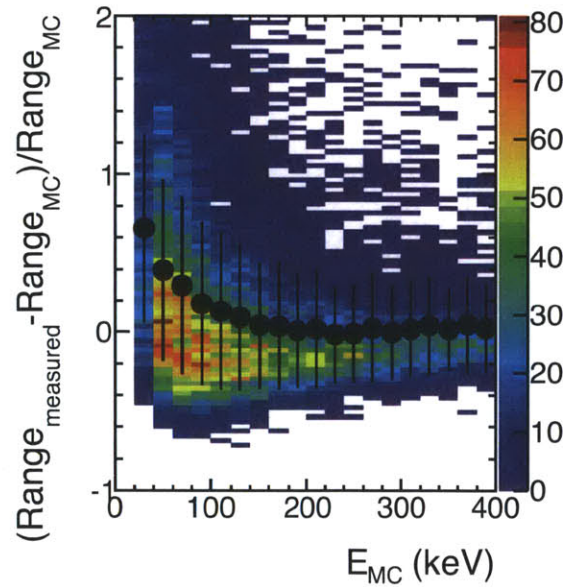
In order to evaluate the quality of the reconstruction parameters, a sample of randomly directed neutrons with an energy spectrum of a ^{252}Cf source is created in the Monte Carlo. This sample is passed through the reconstruction in exactly the same way as data.

Fig. 5-3 and Fig. 5-4 shown the energy and range resolutions for the two cameras as a function of the energy of the recoiling nucleus. The resolutions are slightly different between the two cameras due to different optical properties and due to different length scales between the two cameras. The energy resolution is relatively gaussian for energies above 50 keV, and decreases, as expected, with increasing recoil energy. The range resolution, however, is highly skewed, even at higher energies, due to the difficulty of reconstructing the range out of the diffuse track.

This reconstruction was verified with a brief (3000 s) run with a ^{252}Cf source. Candidate nuclear recoils from this run are shown in Figs. 5-5 and 5-6. Also shown in these plots is the predicted range-energy function for the running parameters. This

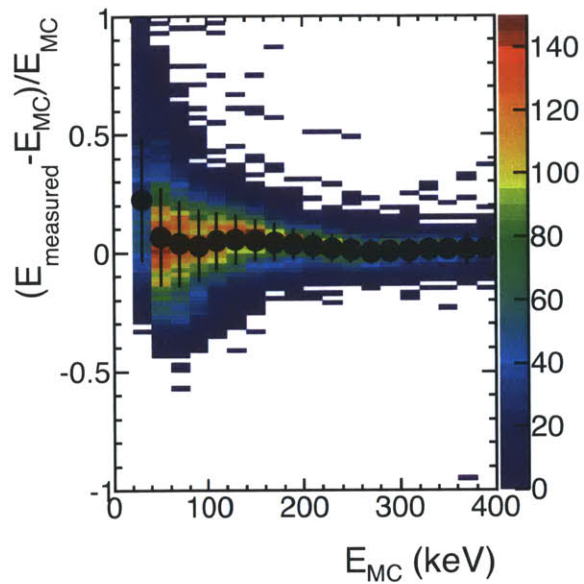


(a)

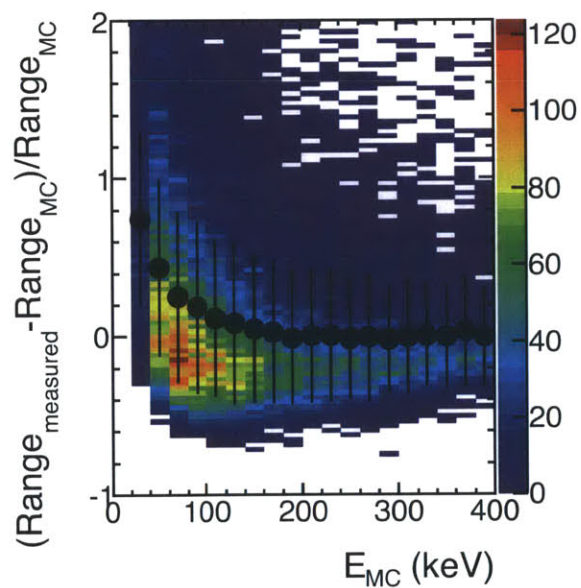


(b)

Figure 5-3: Energy and range reconstruction for top detector. Shown in (a) is the energy resolution as a function of recoil energy, which is 14.6% at 100 keV. Shown in (b) is the range reconstruction as a function of recoil energy. The colored histogram shows the distribution of Monte Carlo events, and black points are a profile histogram of the points, with the error bars representing the RMS of each energy bin.



(a)



(b)

Figure 5-4: Energy and range reconstruction for bottom detector. Shown in (a) is the energy resolution as a function of recoil energy, which is 17.0% at 100 keV. Shown in (b) is the range reconstruction as a function of recoil energy. The colored histogram shows the distribution of Monte Carlo events, and black points are a profile histogram of the points, with the error bars representing the RMS of each energy bin.

prediction is the 3D range of the particle which should be the maximum value of the measured 2D range; that is, all the measured points, if they were measured perfectly, should fall below this line. The candidate recoils largely do fall under this, but finite measurement resolution causes some to fall above the line. The grey boxes in the plot show where Monte Carlo generated recoils from a ^{252}Cf source fall, and the data and Monte Carlo are in agreement.

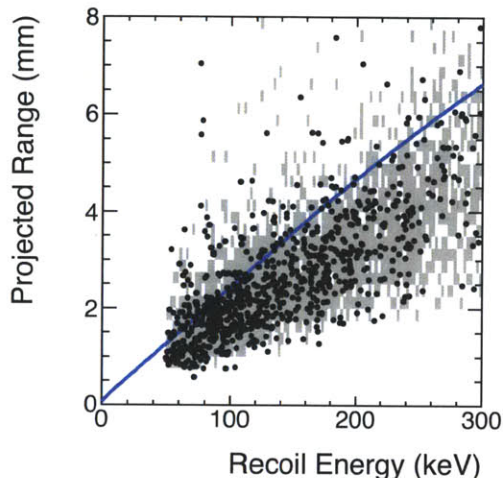


Figure 5-5: Projected range (2D) as a function of recoil energy for a ^{252}Cf run, top camera. Black points show nuclear recoil candidates; grey shading shows Monte Carlo generated nuclear recoil candidates; blue line shows predicted (3D) range-energy function for the running conditions.

The ϕ resolution can also be calculated from the Monte Carlo. Fig. 5-7 shows the difference between the reconstructed ϕ and the generated ϕ as a function of nuclear recoil energy. These plots show that there are two parameters that influence the angular resolution: the width of the peak around zero (how well the axial angle can be determined) and what percentage of the events are in the central peak as opposed to the sideband peaks (how well the vector direction of the track can be determined).

Fig. 5-8 shows the axial angular resolution as a function of nuclear recoil energy for both cameras; as expected the angular resolution gets better as a function of increasing recoil energy. The top camera has an angular resolution of 43° at 100 keV and the bottom camera has an angular resolution of 41° at 100 keV.

Fig. 5-9 shows the determination of vecto—also called the head-tail determination,

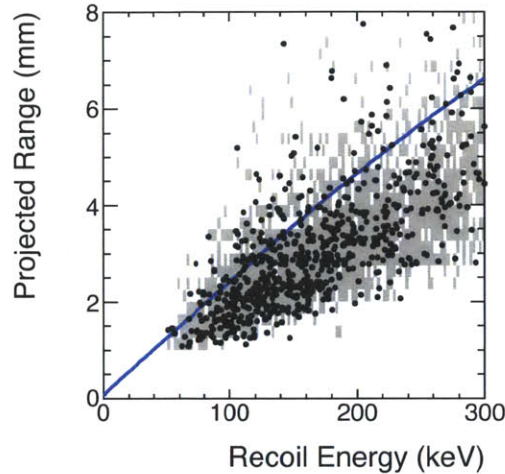
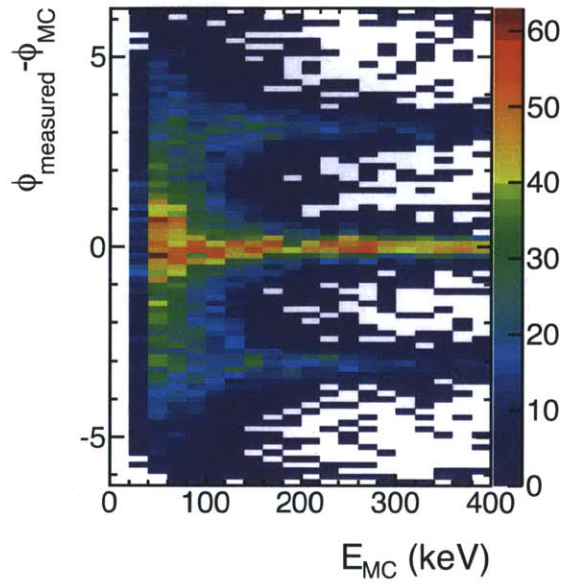


Figure 5-6: Projected range (2D) as a function of recoil energy for a ^{252}Cf run, bottom camera. Black points show nuclear recoil candidates; grey shading shows Monte Carlo generated nuclear recoil candidates; blue line shows predicted (3D) range-energy function for the running conditions.

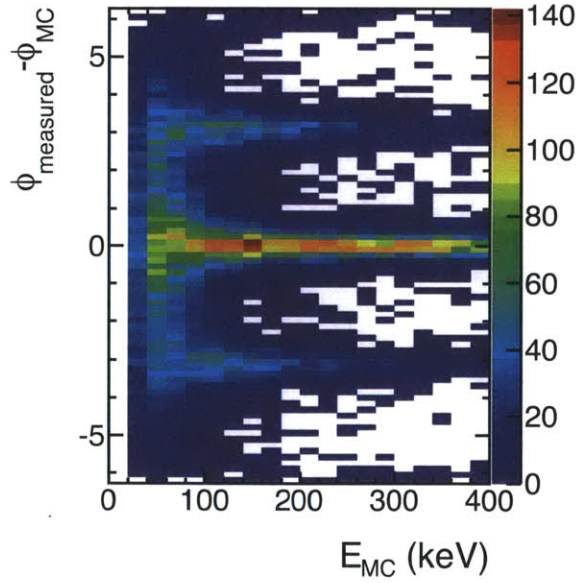
that is, which direction along a particular axis a recoil is traveling—as a function of nuclear recoil energy. For both cameras, the determination is consistent with chance at the lowest energies, and increases with energy, with a typical value of 55% in the energies of interest.

5.4 Backgrounds

The backgrounds for a CCD-based experiment are different from typical backgrounds for dark matter search experiments. Because of the long scattering length in gas, electronic recoils such as those from gammas are not seen with the CCD. A test illumination with an prototype chamber and a 660 keV ^{137}Cs source made a statistics limited measurement indicating that gamma recoils are excluded at the 10^6 level. Similarly, throughgoing muons also produce no visible response in the detector—though they do occasionally interact with the CCD itself. (See Section 5.4.3) The sections below describe the backgrounds of this dark matter search and, where applicable, methods for removing the background from the sample.

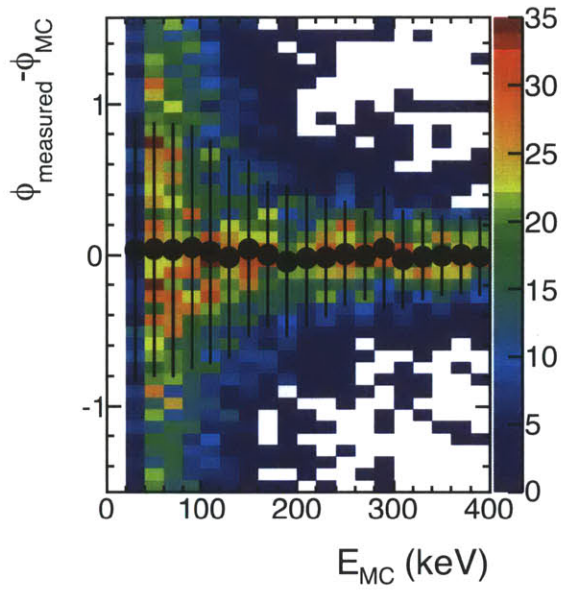


(a)

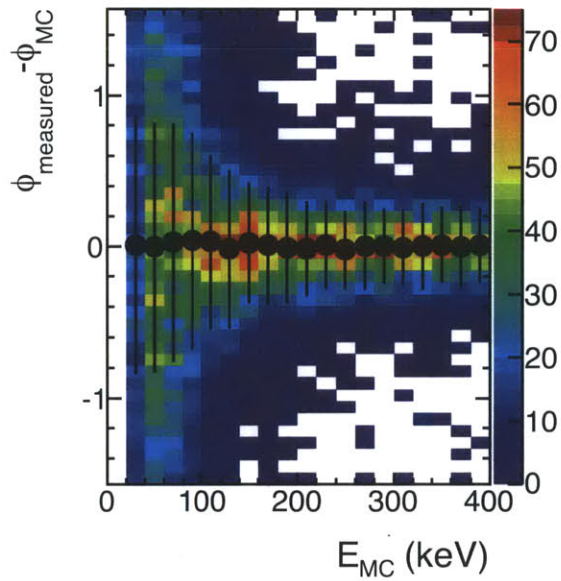


(b)

Figure 5-7: Angular reconstruction (ϕ) for (a) top camera and (b) bottom camera.

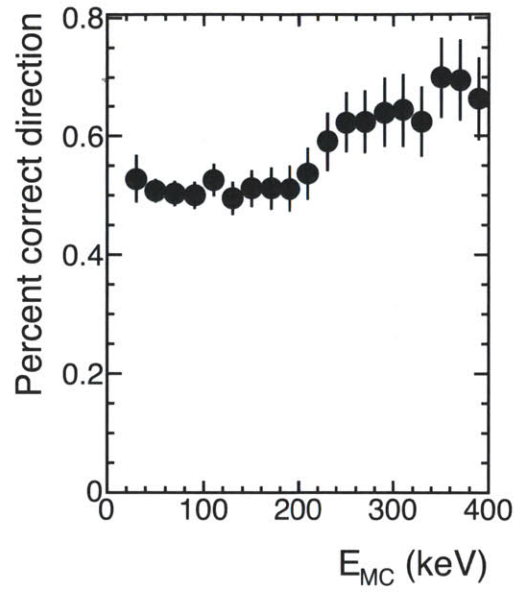


(a)

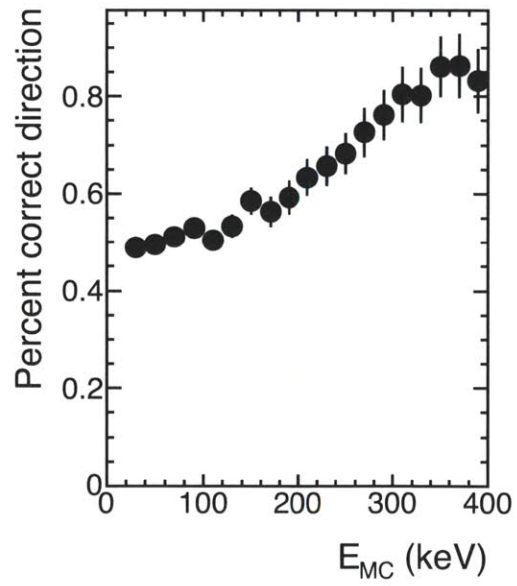


(b)

Figure 5-8: Axial angular reconstruction (ϕ) for (a) top camera and (b) bottom camera. The colored histogram shows the distribution of Monte Carlo events, and black points are a profile histogram of the points, with the error bars representing the RMS of each energy bin.



(a)



(b)

Figure 5-9: Correct percentage of vector direction determination for (a) top camera and (b) bottom camera .

5.4.1 Sparks

Sparks occur in the detector as a result of a breakdown in voltage between the anode plate and the ground mesh. The anode voltage is set in order to have a spark in less than 5% of images. However, sparks occur, and so must be removed from the data sample. There are three methods used to do this: two complementary methods on the whole image, and a separate method to deal with a class of events called partial sparks.

The first whole image method is to compare the mean of the image (before bias subtraction) to the mean of the previous non-spark image. The first image in a run is compared to the bias frame. If this ratio is greater than 1.01, the image is deemed a spark. The second whole image method is to compare the mean of the overscan pixels to the mean of the whole image. Overscan pixels are pixels on the chip of the CCD which are masked from incoming light, and therefore should not be affected by activity in the detector. If the difference between the means exceeds some camera variable threshold (for top, -1; for bottom, -7.5), the image is deemed a spark. These methods are complimentary because the overscan method can catch fainter and more diffuse sparks, but the overscan pixels are not perfectly masked from the whole chip, so a bright spark near the overscan pixels can cause a failure in that method. However, bright sparks are well-caught by the ratio method.

Partial sparks are sparks that occur during the readout of a camera. Because the CCD is read out by passing charge from row to row on the chip, a spark during readout appears displaced, and has a sharp edge. A sample partial spark is shown in Fig. 5-10. These sparks can cover any fraction of the image. For sparks that cover a large fraction of the image, the previous two spark finding methods work well. For sparks covering a small fraction of the image, there may not be enough light deposition to register. However, the hard edge feature can be exploited by running an edge finder on the image, and projecting the results of that edge finder onto the x-axis. If a large, single peak appears, the image is considered a spark.

The next five images after a spark are also vetoed, as the spark causes the gain

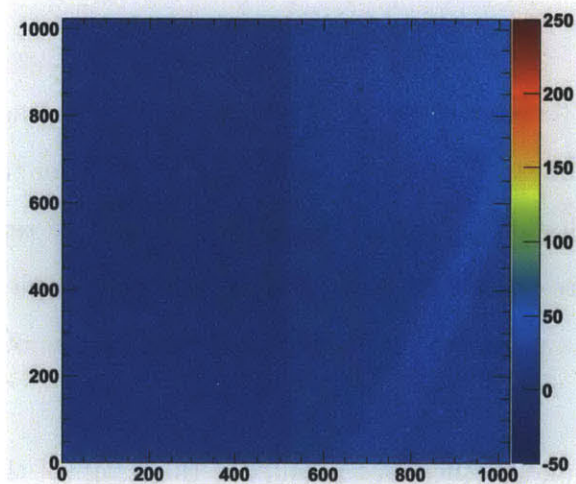


Figure 5-10: A sample partial spark. Note the hard edge of the excess light near the middle of the image. This is the defining quality of a partial spark.

to droop in those images.

5.4.2 Residual Bulk Images

Residual Bulk Images (RBIs) are a camera effect that occurs when charge gets trapped in the bulk silicon beneath a CCD pixel and bleeds out over the next 20 or so images. This effect is dominated by long wavelength light (700 nm and greater) and most prominent after events that put a lot of charge into a pixel, which in this detector is often correlated with sparks. A complete description of the physics of this effect can be found in Reference [76].

The charge bleed, if several nearby pixels are affected, can mimic nuclear recoil tracks. To remove these, two strategies are employed. First, since many RBIs are the result of sparks, spark images are checked to see if they contain pixels which hit the maximum value of the camera. If so, these pixels are marked and any tracks that fall after them which overlap the region significantly are vetoed. Secondly, after all tracks are found, the tracks in a run are all cross-referenced against each other to ensure that they do not overlap in position. This latter method also has the side benefit of removing many tracks which are caused by hot pixels.

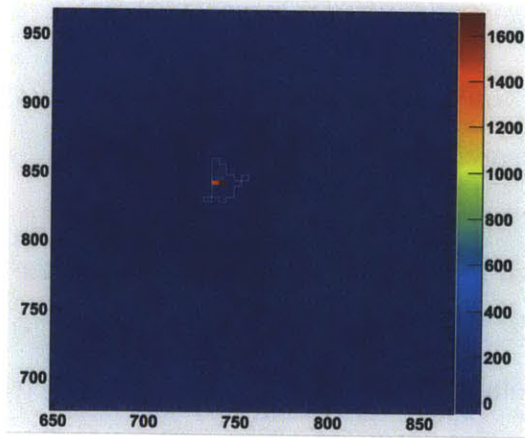
5.4.3 Worms

“Worms” is a collective term coined to cover all types of tracks that appear in detector-off images—things that are found as tracks, but can have no physics basis in the detector. There are three types of worms. The first type is comprised of tracks that have extremely high energy deposition (usually greater than 500 ADU) in one or two pixels. These are hypothesized to come from charged particles (e.g. cosmic ray muons) passing through the CCD chip. The second type is comprised of tracks that have medium deposition (100 ADU) in one pixel. These are hypothesized to come from unfound hot pixels. The third type is comprised of ‘blank’ tracks—tracks that appear to have no internal structure. These are hypothesized to come from fluctuations in the noise background that trigger the track finder. Samples of the three types of worm are shown in Fig. 5-11.

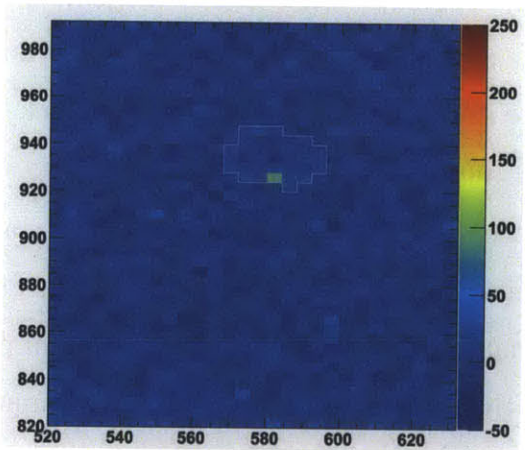
In order to remove these tracks, both hard cuts on certain track reconstruction variables, as well as a linear discriminant analysis using the data taken from detector off runs are used. The hard cuts require that the maximum pixel in a track is below 400 ADU¹, the ratio of the maximum pixel to the total summed energy of the track to be less than 22.5%, and the rms of the cluster to be greater than 10.5 ADU. This last cut addresses the third type of worm, and requires there to be internal structure to the track.

To improve on this discrimination, a Fisher discriminant is also used. The Fisher discriminant [77] is a linear multivariate technique which finds the line in a space of N-variables that maximizes the separation between the means of two populations while minimizing the variance within each population. I.e. the quantity $J(\vec{w}) = \frac{(\mu_1 - \mu_2)^2}{\sigma_1^2 + \sigma_2^2}$ is maximized, where μ_i and σ_i represent the mean and standard deviation of population i when the population has been projected on the line \vec{w} . The Fisher discriminant for this work uses the variables {energy, range, cluster RMS, neighbors, number of pixels, number of pixels in reduced cluster, maximum pixel}, and uses as its two populations a dataset of real worms collected from the cameras and a dataset of Monte Carlo

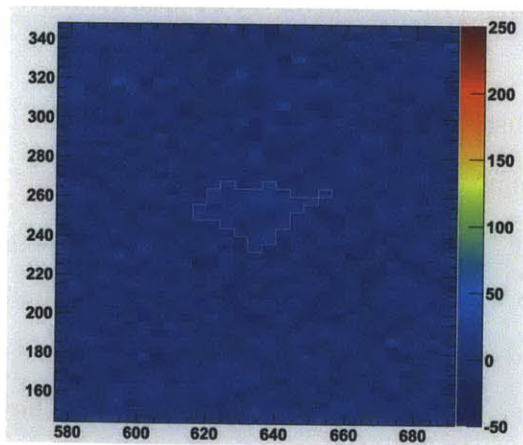
¹In practice, this cuts many alphas as well. However, when doing analyses with alphas, worm cuts can typically be ignored, as requiring a minimum length gets rid of worms.



(a)



(b)



(c)

Figure 5-11: Worm subtypes in the DMTPC detector. Type (a) shows a high deposition worm—note the difference in vertical scales between (a) and (b)/(c). Type (b) shows a medium deposition worm. Type (c) shows a ‘blank’ worm. All images have been zoomed in to show the structure of the worm. The pixels found to be in the track are shown outlined with a thin white line.

generated nuclear recoils. A cut is placed at 0.4 in the discriminant space. The separation in the discriminant is shown in 5-12. Note, interestingly, that the bottom camera (100439) has a significantly lower rate of worms overall; this is characteristic of the differences between cameras and is an important consideration when analyzing data.

5.4.4 Edge Crossing Tracks

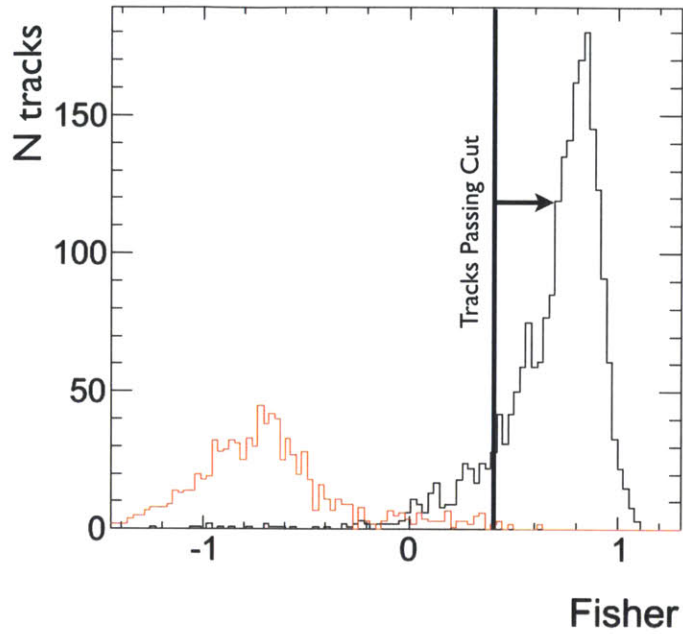
Since the track parameters for tracks which are partially inside the sensitive volume and partially outside of it cannot be determined, these tracks are removed from the sample. If any track has a pixel which touches the edge of the image, this track is vetoed. Additionally, any track whose weighted x or y position falls within 40 pixel units (10 pixels) of the edge is rejected, to account for occasionally missing pixels near the edge. These tracks are typically alphas coming from U/Th chain decays on the drift cage rings.

There are, of course, tracks which cross the vertical boundaries of the detector (e.g. alphas that start above the drift cage and work their way in), but this detector has no way to veto those events currently.

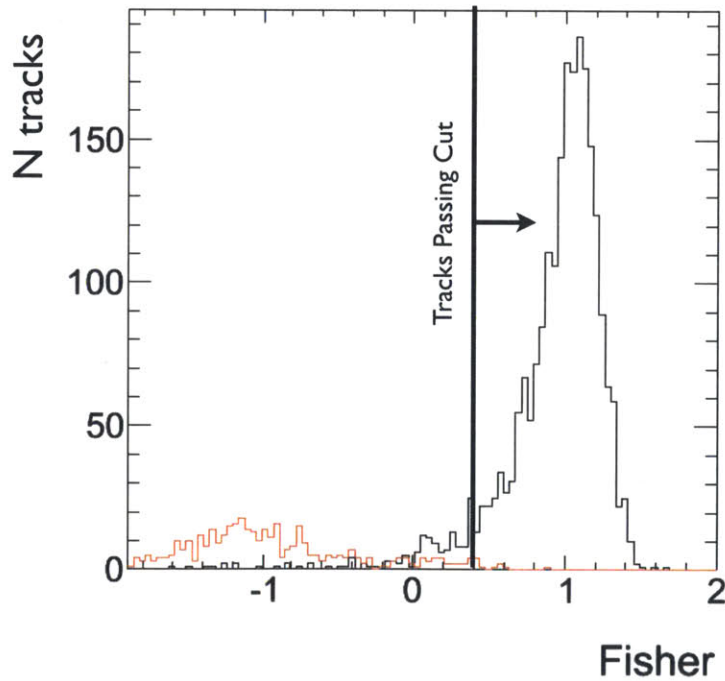
5.4.5 Cutoff Tracks

Cutoff tracks are tracks which are subject to the same issue as the partial sparks described above. However, unlike the sparks, which have a long and easily-findable edge, cutoff tracks have a short edge with a hard cutoff. A sample cutoff track is shown in Fig. 5-13.

To remove these tracks from the sample, the track pixels are projected on the x-axis, normalized so that the largest bin has value 1, and the bin-to-bin derivative is computed. This derivative is called the cluster derivative. The process is repeated with a box drawn around the track, three pixels away from the cluster in all directions. This derivative is called the box derivative. The maximum of the absolute value of both derivatives is taken, and a cut is placed such that if the sum of the cluster



(a)



(b)

Figure 5-12: Fisher discriminant cuts for (a) top camera and (b) bottom camera. The black line shows Monte Carlo simulated recoils and the red line shows tracks from detector off datasets. The small bleed of worms above the cut shown comes from the third type of worm (blank worms) and is addressed by the lower bound cut on cluster RMS.

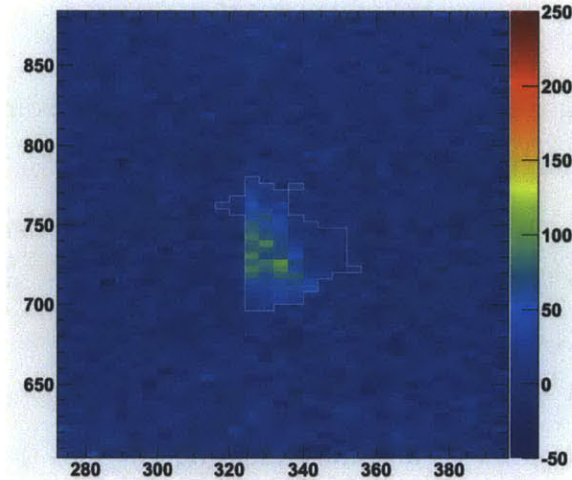


Figure 5-13: A sample cutoff track. Note the hard edge on the left side of the track; this is the hallmark of a cutoff track.

derivative and the box derivative is greater than 0.3, the cluster is determined to be a cutoff track. Fig. 5-14 shows these two derivatives for Monte Carlo samples of cutoff alphas and nuclear recoils and the effect of the cut between them.

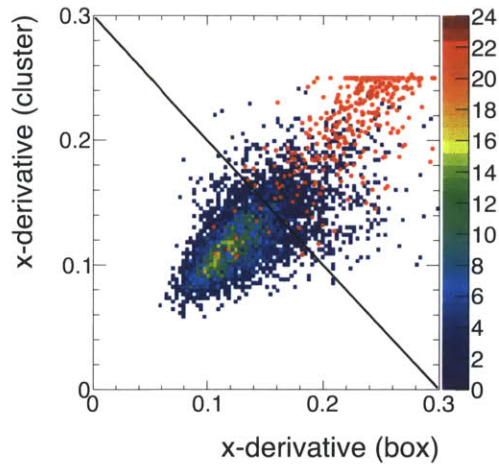


Figure 5-14: The distributions for the two x-derivatives of clusters. Red points show Monte Carlo generated cutoff alpha tracks which pass all other reconstruction cuts. Color-scaled boxes show Monte Carlo nuclear recoil tracks which pass all other reconstruction tracks. The black line shows the cut described in the text.

5.4.6 Misjoined Tracks

The cluster finding algorithm is tuned in such a way to maximize its quality over a large range of track energies and lengths. This means that for long tracks, there are occasional times when part of an alpha track is not correctly joined to the rest of the track, especially when the alpha has a hard scatter across a spacer near the end of the track. When searching for nuclear recoil candidates, these tracks are eliminated by rerunning the track joining algorithm with looser parameters for the distance of closest approach between two tracks and merging any two tracks that are close in distance and across a spacer.

5.4.7 Extreme Partial Sparks

If a partial spark occurs in the outside three bins of an image, the standard edge detector cannot register it, as the edge detector always finds an edge at the actual edge of the image. These sparks can also fake a nuclear recoil event through a position-shifted RBI type event. An example of this type of event is shown in Fig. 5-15. This occurrence of extreme partial sparks is rare, but easy to remove, as the light from the partial sparks gets found as tracks. By checking if additional tracks in the image cover more than 40 pixels along one of the vertical edges of the image, these tracks can be eliminated.

5.4.8 Spacers

Finally, tracks which have a nearest approach to a spacer of 1 pixel—that is, they touch the spacer—are eliminated from the sample. This prevents missing energy from the dead regions of the spacers.

5.4.9 Cut Efficiencies

A large Monte Carlo sample is also used to calculate the efficiency of the detector. Fig. 5-16 shows the energy dependent efficiencies for both cameras. The cuts that

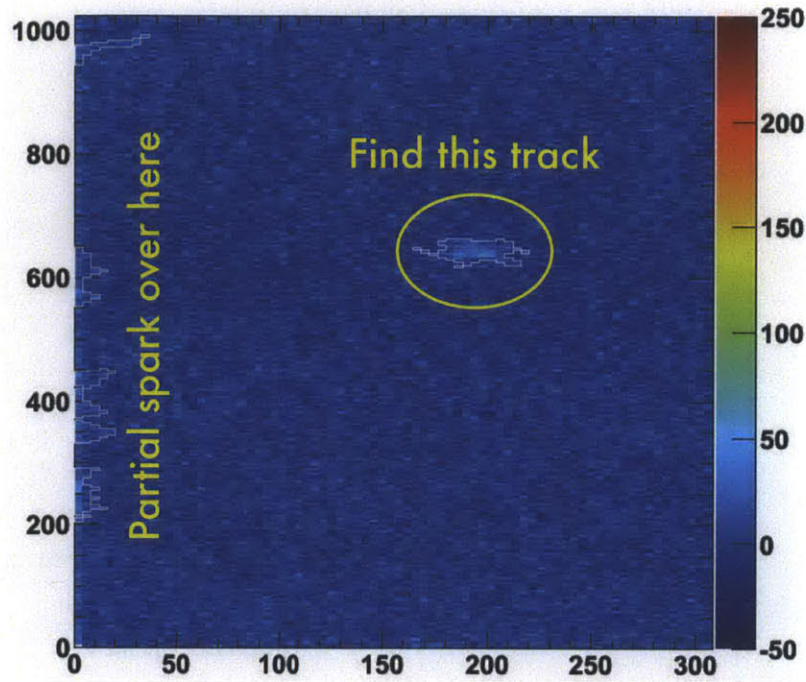


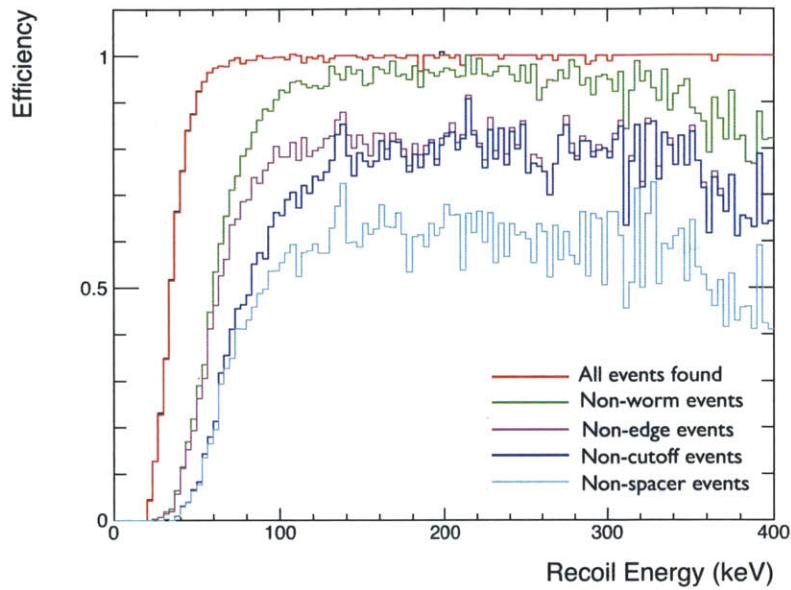
Figure 5-15: A sample extreme partial spark. The image has been zoomed to show both the small amount of light near the left-hand edge and the nuclear recoil candidate resulting from RBI next to it.

most drastically impact the edge of the efficiency turn on are the worm cut and the cutoff track cut. This makes sense, as low energy tracks are difficult to distinguish between the cases. The cuts that most impact the efficiency in the region past the turn-on are the edge and spacer cuts; these are simply geometrical effects that cannot be reduced. There are a few cuts not shown on this efficiency plot, namely RBI, track rejoining, and edge sparks, as they cannot adequately be modeled in simulation.

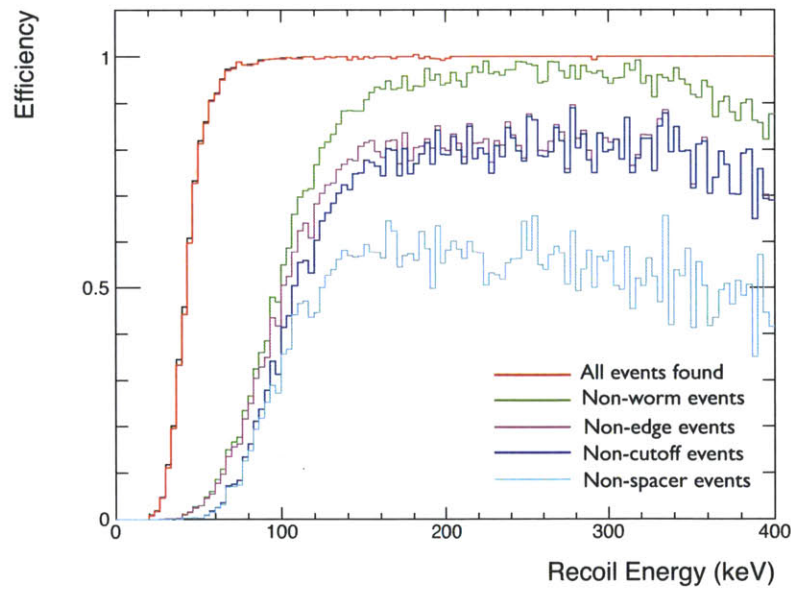
5.4.10 Final Data Sample

The final data sample is constructed by applying all of the cuts described above and then selecting tracks between 80 and 200 keV recoil energy with a length less than 5 mm. The data rates after each cut are shown in Table 5.1. A total of 1907000 images were recorded for this data sample.

A range vs. energy plot for the data is shown in Fig. 5-17, showing that most of the tracks sit below the expected fluorine recoil band, shown in blue. The a histogram



(a)



(b)

Figure 5-16: Cut efficiencies as a function of energy for (a) top camera and (b) bottom camera. Not shown are the RBI, track rejoining, or edge cut sparks, as they do not contribute in simulation.

Cut	Camera					
	081264		100439		Total	
	Number	Rate (Hz)	Number	Rate (Hz)	Number	Rate (Hz)
Non-Spark Images	1666084		1607601			
All Tracks	221586	0.133	189195	0.118	410781	0.251
Non-RBI	148966	0.0894	181921	0.113	330887	0.203
Non-Worm	17456	0.0100	25654	0.0160	43110	0.0260
Fiducial	1326	0.000796	1343	0.000835	2669	0.00163
50 < E < 300 (keV)	806	0.000484	702	0.000437	1508	0.000921
Non-Cutoff	446	0.000268	390	0.000243	836	0.000510
Remerge	434	0.000260	383	0.000238	817	0.000499
Non-Edge Spark	433	0.000260	380	0.000236	813	0.000496
Non-Spacer	368	0.000221	268	0.000167	636	0.000386
80 < E < 200 (keV)	205	0.000123	162	0.000101	367	0.000224

Table 5.1: Rates of events passing each cut for source-free data with the 10L detector, for 1907000 1 s exposures on each side of the chamber.

of the energy is shown in 5-18, and shows that it has a rapidly falling shape as a function of energy.

Figure 5-19 shows the reduced angle distribution of the tracks in the sample, and Fig. 5-20 show the reduced angle as a function of recoil energy. Evidence for dark matter would show up as a peak in these distributions around 0. In order to evaluate if there is some asymmetry in the ϕ distribution, we perform a Rayleigh test for asymmetry in circular data. The use of this test for looking at dark matter distributions is described in Reference [55]. These data have a Rayleigh $R^* = 2.94$ with $N = 367$, which has a probability value $p = 0.230$, which indicates that 23% of Rayleigh values calculated from a uniform distributions would have a Rayleigh R^* greater than this distribution. More simply, there is no evidence for an angular asymmetry (and thus dark matter) from these data.

5.5 Dark Matter Limits

With the data, a limit is set on the dark matter cross section as a function of mass. The model used for limit setting is the standard isotropic halo described in Sec-

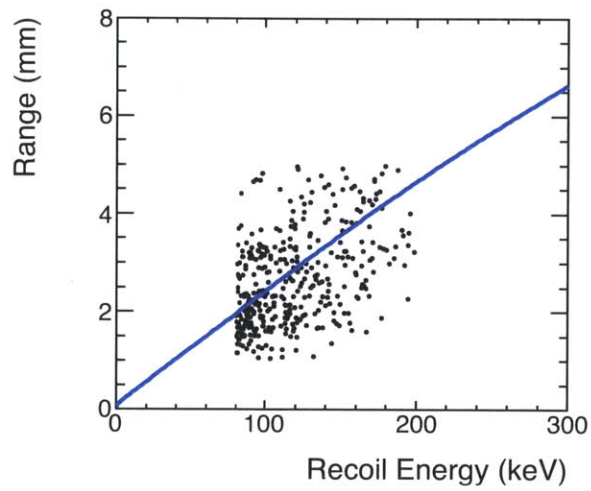


Figure 5-17: Range vs. energy for tracks that pass all cuts. Data points are shown with black circles; the predicted range vs. energy curve for fluorine recoils is shown with the blue line.

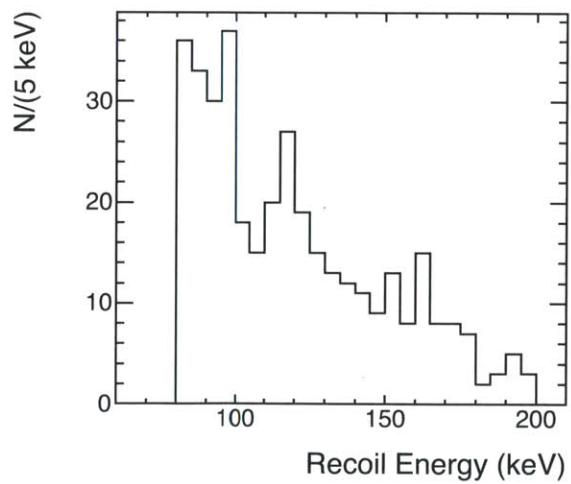


Figure 5-18: The energy spectrum for tracks that pass all cuts.

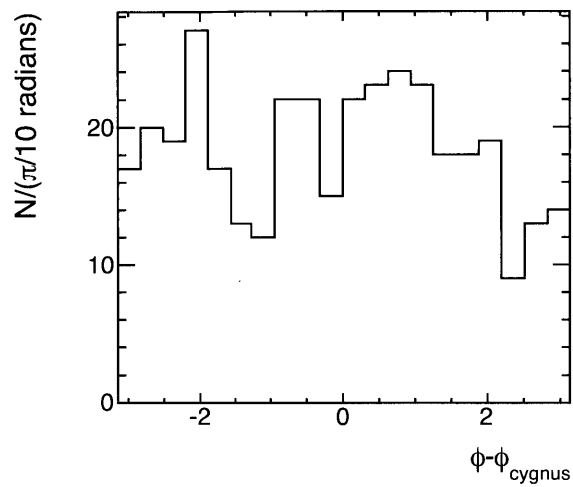


Figure 5-19: The reduced phi distribution for tracks that pass all cuts. Evidence for dark matter would appear as a peak around zero.

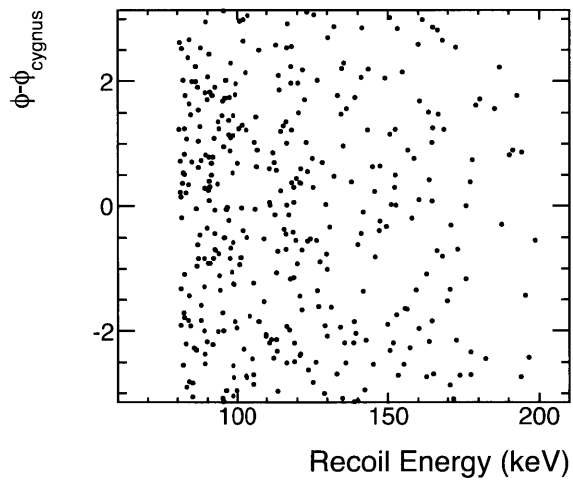


Figure 5-20: The reduced phi distribution as a function of energy for tracks that pass all cuts.

tion 1.3.2, and a simple poisson limit is set, using the energy window between 80 and 200 keV. Within this window, the number of events is corrected in each camera according to the MC-generated efficiencies for that particular camera, and then the number of events between the two cameras is summed. A poisson limit was chosen due to the high background rate and lack of evidence of directionality from the angular distribution. The results of the limit setting are shown in Fig. 5-21. The limit for this work has a minimum at $m_\chi = 100$ GeV of 3.7×10^{-33} cm². This is a conservative limit, which assumes that the only exposure is during the 1 s exposure time of the camera; a limit is additionally shown which takes into account the 0.3 s parasitic exposure which happens during camera readout. This limit has a minimum at $m_\chi = 100$ GeV of 2.9×10^{-33} cm².

5.6 Discussion

The most obvious thing to note about the limit set using the data taken underground with the 10L detector is that the limit set is considerably worse than the limit set at the surface. Since this is precisely opposite of what is expected, a minor investigation was undertaken to investigate this effect.

The first thing to consider is if there is some sort of physical background that could cause this increase. There are two potential physics processes that can introduce potential nuclear recoils: neutrons, which exactly fake the expected signal, and alphas, which can fake the signal through poor reconstruction. It is hard to see how neutrons would cause an increased rate underground. The expected rate of neutrons producing recoils between 80 and 200 keV on the surface is 5 per day. Since the background neutron flux underground is approximately 10^5 lower than the surface neutron flux, it is unlikely that this is the culprit.

Alphas pose a more complicated scenario, as the entire detector was disassembled, packed, shipped, and reassembled between the surface run and the underground run, and, as this was not a process with excessive attention paid to cleanliness, it is possible that additional contaminants were introduced into the detector during this process,

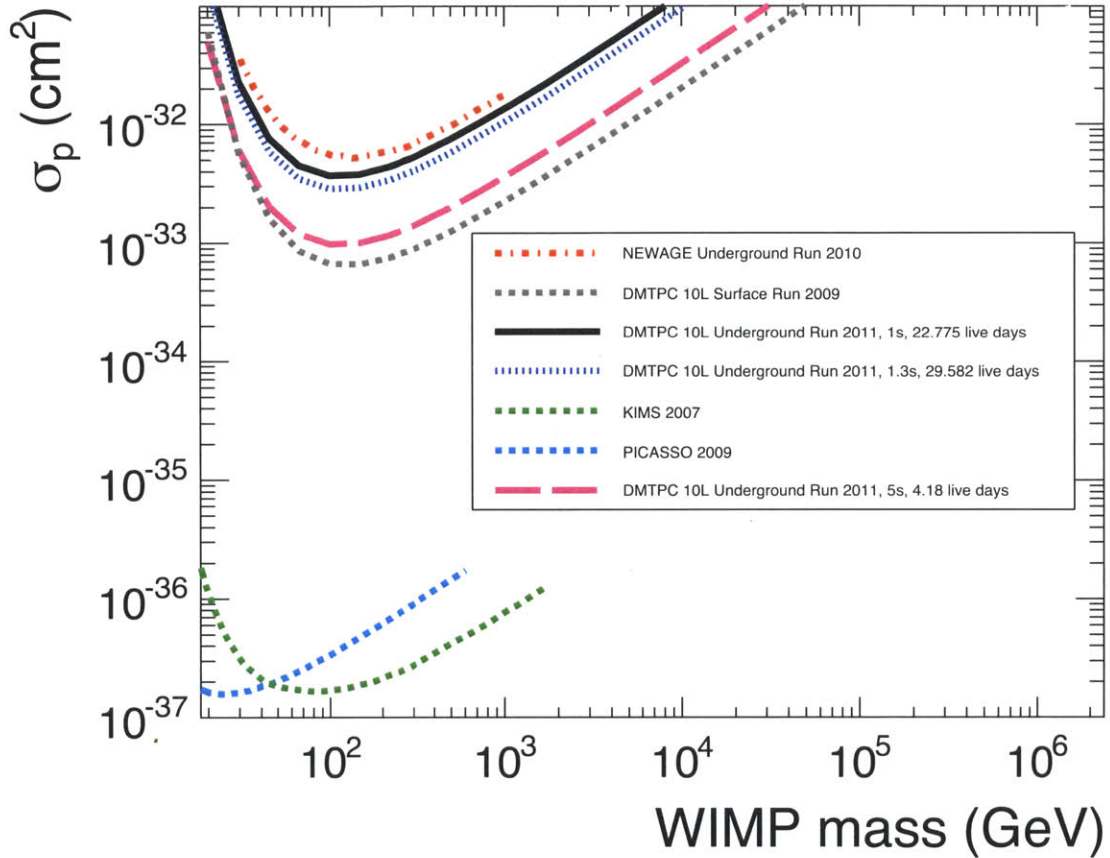


Figure 5-21: WIMP cross section normalized to single proton limits as a function of mass for this work using an assumption of 1 s exposures (solid black line), an assumption of 1.3 s exposures (small dotted blue line), and a brief run with 5 s exposures (long dashed magenta line). Also shown are limits from the 10L above ground (dotted grey line) [12], NEWAGE (dot-dash red line) [13], KIMS (dotted green line) [14], PICASSO (dotted cyan line) [15], and projected for the next generation DMTPC detector (small dotted blue line).

causing a much higher internal background rate. To study this, the rate of alphas between the surface run and the underground run can be compared. For this purpose, an alpha is defined as a track with a range greater than 10 mm and an energy greater than 500 keV. No other requirements are placed other than avoidance of sparks. With these requirements, in the top camera, the rate on the surface is 0.0253 ± 0.0006 Hz, and underground the rate is 0.0278 ± 0.0008 Hz. While the rate underground is slightly higher than the surface rate, it is clearly not sufficient to explain the discrepancy.

The rates of physics backgrounds are summarized in Table 5.2

Background	Surface (Hz)	Underground (Hz)
Neutron Flux (calculated)	6.42×10^{-5}	1.6×10^{-10}
Alpha Contamination (measured)	0.0253 ± 0.0006	0.0278 ± 0.0008

Table 5.2: Rates of potential physics background events on the surface and underground. Neutron rates from the surface are calculated in [18] and [12] and then scaled by exposure, efficiency, and total neutron flux from [19] for underground. Alpha contamination rates are for the top camera of the 10L detector, measured in data.

The main difference between above-ground and underground data is that above-ground data was taken with 5 s exposures and underground data was taken with 1 s exposures. To see if this had a major effect, 87,000 5 s exposures were taken and processed with the same cuts as the 1 s exposures. One cut had to be added, to ensure that the centroid (x-y position) of the track was located within the track. This cut had no effect on the 1 s data when added to that analysis. The rates for tracks passing each cut in this data set are shown in Table 5.3.

These rates show that there is a major difference between the two exposure times, and the rates for 5 s exposures are slightly lower than the above-ground rates, as might be expected. The reason for this difference is not yet clear, and there is a program of measurements ongoing to understand the difference in noise rates. A limit from this abbreviated data set is also shown in Fig. 5-21, and is considerably better than the limit for the 1 s exposures, with a minimum at $m_\chi = 100$ GeV of 9.8×10^{-34} cm² and approaches the surface run data.

Cut	Camera					
	081264		100439		Total	
	Number	Rate (Hz)	Number	Rate (Hz)	Number	Rate (Hz)
Non-Spark Images	71223		73016			
All Tracks	196474	0.552	138874	0.380	335348	0.932
Non-RBI	28182	0.0791	29834	0.0817	58016	0.161
Non-Worm	3958	0.0111	5061	0.0138	9019	0.0250
Fiducial	272	0.000764	227	0.000623	499	0.00139
50 < E < 300 (keV)	144	0.000404	111	0.000304	255	0.000708
Non-Cutoff	60	0.000168	36	0.0000986	96	0.000267
Remerge	31	0.0000871	26	0.0000712	57	0.000158
Non-Edge Spark	31	0.0000871	26	0.0000712	57	0.000158
Non-Spacer	22	0.0000618	18	0.0000493	40	0.000111
80 < E < 200 (keV)	9	0.0000253	7	0.0000191	16	0.0000444

Table 5.3: Rates of events passing each cut for 87000 5 s exposures on each side of the camera, using the same cuts as for the 1 s data in Table 5.1. Two alpha sources were deployed in the top chamber.

Chapter 6

Conclusions

This work has looked at searches for two different types of rarely interacting matter—cosmic relic neutrinos and dark matter—in the universe. In both cases, no evidence was found for the particle, however, the work in both cases points to important considerations for future research.

In the case of the cosmic relic neutrinos, it is obvious that the limiting factor for discovery is the small amount ($40\mu\text{g}$) of tritium in KATRIN. Furthermore, because KATRIN operates at the maximum tritium source column density, the only way to scale the technology is to scale the cross sectional area of the apparatus. To even approach a feasible amount of tritium, a super-KATRIN would have to be unimaginably large—many kilometers in diameter for the spectrometer. Therefore, a new technology is necessary. One such proposed technology is microwave antenna detection of synchrotron radiation from decay electrons in a magnetic field, as described by the Project 8 collaboration [78]. This technology may be scalable enough to reach the large tritium masses needed for a successful search, but is still in very early stages of development.

By contrast with KATRIN, this work shows that the DMTPC technology is still very much in development, especially with regards to backgrounds to directional searches. This work has enumerated many of the backgrounds to a directional search using this technology, and also has shown that there are still unknown backgrounds. As described in Section 5.6, there is an ongoing set of measurements with differ-

ent exposure times in order to try and resolve the difference between the 1 s and 5 s exposures. Additionally, fully commissioning and incorporating the charge read-out information may be able to distinguish camera backgrounds from physics backgrounds [79], and especially provide a way to remove worm and cutoff events without the efficiency drag of the current methods. These two activities will point the way to understanding the result of this work, vital for understanding if the background for this technology can be reduced sufficiently for a competitive dark matter search.

The DMTPC collaboration is also currently building its next generation prototype, the four-shooter, which has approximately twice the active mass and four cameras. This detector also has been constructed with more care as to the cleanliness of the interior components, including the use of copper rings for the field cage instead of steel, reducing the internal uranium and thorium decay chain (and therefore alpha) contamination. Additionally, the cameras of this detector are arranged such that the whole area of the drift cage-amplification region is imaged, which allows a much more thorough study of where internal backgrounds originate than was possible in the 10L.

It is clear that the current backgrounds are too high to make DMTPC currently competitive in the field. However, the ongoing program has a lot of power to address these backgrounds and hopefully reduce them to the point where the power of directionality can be brought to bear to search for dark matter. As the non-directional dark matter experiments grow in size and sensitivity, it is likely that there will be more claims of dark matter detection. Already there is tension between experiments, especially those with annual oscillation signals and those which do not do a time-dependent analysis. Directionality is a powerful way to determine the validity of these claims, as shown by Green and Morgan, and the development of directional technology should be a priority for the field in order to be ready for the time when it will be vital.

Bibliography

- [1] K. G. Begeman, A. H. Broeils, and R. H. Sanders. Extended rotation curves of spiral galaxies: Dark haloes and modified dynamics. *Monthly Notices of the Royal Astronomical Society*, 249:523–537, 1991.
- [2] R.P. Olling and M.R. Merrifield. Two measures of the shape of the dark halo of the Milky Way. *Monthly Notices of the Royal Astronomical Society*, 311(2):361–369, 2000.
- [3] E. Aprile et al. Dark matter results from 100 live days of XENON100 data. *Arxiv preprint arXiv:1104.2549*, 2011.
- [4] Z. Ahmed et al. Dark matter search results from the CDMS II experiment. *Science*, 327:1619, 2010.
- [5] Z. Ahmed et al. Results from a low-energy analysis of the CDMS II germanium data. *Physical Review Letters*, 106(13):131302, 2011.
- [6] R. Bernabei et al. First results from DAMA/LIBRA and the combined results with DAMA/NaI. *The European Physical Journal C-Particles and Fields*, 56(3):333–355, 2008.
- [7] C.E. Aalseth et al. Results from a search for light-mass dark matter with a p-type point contact germanium detector. *Physical Review Letters*, 106(13):131301, 2011.
- [8] R. Gaitskell, V. Mandic, and J. Fillipini. Dark matter tools plotter. <http://dmttools.brown.edu>.
- [9] E. Behnke et al. Spin-dependent WIMP limits from a bubble chamber. *Science*, 319(5865):933, 2008.
- [10] H. S. Lee et al. Limits on interactions between weakly interacting massive particles and nucleons obtained with CsI (Tl) crystal detectors. *Physical review letters*, 99(9):91301, 2007.
- [11] G. L. Fogli et al. Hints of $\theta_{13} > 0$ from global neutrino data analysis. *Phys. Rev. Lett.*, 101:141801, 2008.

- [12] S. Ahlen et al. First dark matter search results from a surface run of the 10-L DMTPC directional dark matter detector. *Physics Letters B*, 2010.
- [13] K. Miuchi et al. First underground results with NEWAGE-0.3a direction-sensitive dark matter detector. *Physics Letters B*, 686:11–17, 2010.
- [14] H. S. Lee et al. Limits on WIMP-nucleon interactions with CsI(Tl) crystal detectors. *Phys. Rev. Lett.*, 99:091301, 2007.
- [15] S. Archambault et al. Dark matter spin-dependent limits for WIMP interactions on 19-F by PICASSO. *Phys. Lett.*, B682:185–192, 2009.
- [16] J. Ellis et al. Implications of LEP on laboratory searches for dark matter neutralinos. *Nuclear Physics B*, 400(1-3):25–36, 1993.
- [17] A.G. Cocco, G. Mangano, and M. Messina. Probing low energy neutrino backgrounds with neutrino capture on beta decaying nuclei. *Journal of Cosmology and Astroparticle Physics*, 06:015, 2007.
- [18] T. Nakamura et al. Sequential measurements of cosmic-ray neutron spectrum and dose rate at sea level in Sendai, Japan. *Journal of Nuclear Science and Technology*, 42 No. 10:843–853, 2005.
- [19] D.M. Mei and A. Hime. Muon-induced background study for underground laboratories. *Physical Review D*, 73(5):053004, 2006.
- [20] A.A. Penzias and R.W. Wilson. A measurement of excess antenna temperature at 4080 mc/s. *The Astrophysical Journal*, 142:419–421, 1965.
- [21] G.F. Smoot et al. Structure in the COBE differential microwave radiometer first-year maps. *The Astrophysical Journal*, 396:L1–L5, 1992.
- [22] D.N. Spergel et al. First-year Wilkinson Microwave Anisotropy Probe (WMAP) observations: determination of cosmological parameters. *The Astrophysical Journal Supplement Series*, 148:175, 2003.
- [23] E. Komatsu et al. Seven-year Wilkinson Microwave Anisotropy Probe (WMAP) observations: Cosmological interpretation. *The Astrophysical Journal Supplement Series*, 192:18, 2011.
- [24] C. L. Cowan et al. Detection of the free neutrino: a confirmation. *Science*, 124(3212):103, 1956.
- [25] K. Nakamura. Review of particle physics. *Journal of Physics G: Nuclear and Particle Physics*, 37:075021, 2010.
- [26] D. H. Perkins. *Particle Astrophysics*. Oxford Master Series in Particle Physics, Astrophysics, and Cosmology. Oxford University Press, Oxford, second edition, 2009.

- [27] R. N. Mohapatra and P. B. Pal. *Massive Neutrinos in Physics and Astrophysics*. World Scientific Lecture Notes in Physics, Vol. 72. World Scientific, third edition, 2004.
- [28] S. Weinberg. Universal neutrino degeneracy. *Phys. Rev.*, 128(3):1457–1473, Nov 1962.
- [29] A. Ringwald and Y.Y.Y. Wong. Gravitational clustering of relic neutrinos and implications for their detection. *Journal of Cosmology and Astroparticle Physics*, 12:005, 2004.
- [30] W.H. Press and P. Schechter. Formation of galaxies and clusters of galaxies by self-similar gravitational condensation. *The Astrophysical Journal*, 187:425–438, 1974.
- [31] A. S. Szalay and G. Marx. Neutrino rest mass from cosmology. *Astronomy and Astrophysics*, 49:437–441, 1976.
- [32] M. Boylan-Kolchin, J.S. Bullock, and M. Kaplinghat. The milky way’s bright satellites as an apparent failure of Λ CDM. *Arxiv preprint arXiv:1111.2048*, 2011.
- [33] W. J. G. De Blok. The core-cusp problem. *Advances in Astronomy*, 2010:5, 2010.
- [34] F. Zwicky. On the masses of nebulae and of clusters of nebulae. *The Astrophysical Journal*, 86:217, 1937.
- [35] V.C. Rubin et al. Rotation velocities of 16 SA galaxies and a comparison of Sa, Sb, and SC rotation properties. *The Astrophysical Journal*, 289:81–98, 1985.
- [36] V.C. Rubin, W.K. Ford Jr, and N. Thonnard. Rotational properties of 21 SC galaxies with a large range of luminosities and radii, from NGC 4605/R= 4kpc/to UGC 2885/R= 122 kpc. *The Astrophysical Journal*, 238:471–487, 1980.
- [37] M. Kamionkowski and A. Kinkhabwala. Galactic halo models and particle dark-matter detection. *Phys. Rev. D*, 57(6):3256–3263, Mar 1998.
- [38] W. Boer and M. Weber. The dark matter density in the solar neighborhood reconsidered. *Journal of Cosmology and Astroparticle Physics*, 2011:002, 2011.
- [39] T. Bruch et al. Dark matter disc enhanced neutrino fluxes from the sun and earth. *Physics Letters B*, 674(4-5):250–256, 2009.
- [40] R. Catena and P. Ullio. A novel determination of the local dark matter density. *Journal of Cosmology and Astroparticle Physics*, 2010:004, 2010.
- [41] M. Pato et al. Systematic uncertainties in the determination of the local dark matter density. *Physical Review D*, 82(2):023531, 2010.
- [42] F.J. Kerr and D. Lynden-Bell. Review of galactic constants. *Monthly Notices of the Royal Astronomical Society*, 221:1023–1038, 1986.

- [43] G. Bertone, editor. *Particle Dark Matter*. Cambridge University Press, 2010.
- [44] R. D. Peccei and H. R. Quinn. Constraints imposed by CP conservation in the presence of instantons. *Physical Review D*, 16:1791.
- [45] S. J. Asztalos et al. Improved RF cavity search for halo axions. *Physical Review D*, 69(1):011101, 2004.
- [46] S. J. Asztalos et al. SQUID-based microwave cavity search for dark-matter axions. *Physical review letters*, 104(4):41301, 2010.
- [47] A. Boyarsky et al. Realistic sterile neutrino dark matter with keV mass does not contradict cosmological bounds. *Physical review letters*, 102(20):201304, 2009.
- [48] T. K. Hemmick et al. Search for low- z nuclei containing massive stable particles. *Physical Review D*, 41(7):2074, 1990.
- [49] J. D. Lewin and P. F. Smith. Review of mathematics, numerical factors, and corrections for dark matter experiments based on elastic nuclear recoil. *Astropart. Phys.*, 6:87–112, 1996.
- [50] G. Jungman, M. Kamionkowski, and K. Griest. Supersymmetric dark matter. *Physics Reports*, 267(5-6):195–373, 1996.
- [51] P. Gondolo. Recoil momentum spectrum in directional dark matter detectors. *Physical Review D*, 66(10):103513, 2002.
- [52] S. R. Deans. *The Radon transform and some of its applications*. John Wiley and Sons, 1983.
- [53] B. Morgan, A. M. Green, and N. J. C. Spooner. Directional statistics for realistic weakly interacting massive particle direct detection experiments. *Physical Review D*, 71(10):103507, 2005.
- [54] A. M. Green and B. Morgan. Optimizing WIMP directional detectors. *Astroparticle Physics*, 27(2-3):142–149, 2007.
- [55] B. Morgan and A. M. Green. Directional statistics for realistic weakly interacting massive particle direct detection experiments. ii. 2d readout. *Physical Review D*, 72(12):123501, 2005.
- [56] A. M. Green and B. Morgan. Consequences of statistical sense determination for WIMP directional detection. *Physical Review D*, 77(2):027303, 2008.
- [57] J. Ellis, A. Ferstl, and K. A. Olive. Re-evaluation of the elastic scattering of supersymmetric dark matter. *Physics Letters B*, 481(2-4):304–314, 2000.
- [58] G. J. Alner et al. The DRIFT-II dark matter detector: Design and commissioning. *Nucl. Instrum. Meth.*, A555:173–183, 2005.

- [59] E. Daw et al. Spin-dependent limits from the DRIFT-IIId directional dark matter detector. *Arxiv preprint arXiv:1010.3027*, 2010.
- [60] D. Santos and others. MIMAC : A Micro-TPC Matrix of Chambers for direct detection of WIMPs. *J. Phys. Conf. Ser.*, 65:012012, 2007.
- [61] J. Angrik et al. KATRIN Design Report 2004. *Wissenschaftliche Berichte FZKA*, 7090, 2005.
- [62] T. Thümmler, R. Marx, and C. Weinheimer. Precision high voltage divider for the KATRIN experiment. *New Journal of Physics*, 11:103007, 2009.
- [63] S. Grohmann et al. Precise temperature measurement at 30 K in the KATRIN source cryostat. *Cryogenics*, 2011.
- [64] V. M. Lobashev and P. E. Spivak. A method for measuring the electron antineutrino rest mass. *Nucl. Instr. and Meth. A*, 240(2):305, 1985.
- [65] A. Saenz, S. Jonsell, and P. Froelich. Improved Molecular Final-State Distribution of HeT for the β -Decay Process of T₂. *Phys Rev Lett*, 84:242, 2000.
- [66] W. Y. Hwang and B. Q. Ma. Detection of cosmic neutrino clustering by cosmic ray spectra. *New Journal of Physics*, 7:41, 2005.
- [67] G. J. Stephenson, Jr., J. Terrance Goldman, and B. H. J. McKellar. Neutrino clouds. *Int. J. Mod. Phys.*, A13:2765–2790, 1998.
- [68] S. Ahlen et al. The case for a directional dark matter detector and the status of current experimental efforts. *Int. J. Mod. Phys.*, 25:1–51, 2010.
- [69] L. G. Christophorou, J. K. Olthoff, and M. Rao. Electron interactions with CF₄. *Journal of Physical and Chemical Reference Data*, 25(5):1341–1388, 1996.
- [70] T. Caldwell et al. Transport properties of electrons in CF₄. *Arxiv preprint arXiv:0905.2549*, 2009.
- [71] A. Kaboth et al. A measurement of photon production in electron avalanches in CF₄. *Nucl. Instr. and Meth. A*, 592(1-2):63–72, 2008.
- [72] J. F. Ziegler, J. P. Biersack, and U. Littmark. The stopping and range of ions in solids. *Pergamon Press*, New York, 1985.
- [73] National Nuclear Data Center. Information extracted from the chart of nuclides database. <http://www.nndc.bnl.gov/chart/>.
- [74] R. Hayes and H.C. Chiou. Preliminary evaluation of real time false CAM alarm prediction through continuous radon monitoring. *Health Physics*, 84(5):S89, 2003.

- [75] A. Hitachi. Bragg-like curve for dark matter searches: Binary gases. *Radiation Physics and Chemistry*, 77(10-12):1311–1317, 2008.
- [76] J.R. Janesick. *Scientific Charge-Coupled Devices*, volume 83. Society of Photo Optical, 2001.
- [77] S. Mika et al. Fisher discriminant analysis with kernels. In *Neural Networks for Signal Processing IX, 1999. Proceedings of the 1999 IEEE Signal Processing Society Workshop*, pages 41–48. IEEE, 1999.
- [78] B. Monreal and J.A. Formaggio. Relativistic cyclotron radiation detection of tritium decay electrons as a new technique for measuring the neutrino mass. *Physical Review D*, 80(5):051301, 2009.
- [79] J. P. Lopez et al. Background rejection in the DMTPC dark matter search using charge signals. *Arxiv preprint arXiv:1109.3501*, 2011.